INVESTIGATION OF ALTERNATIVE BATTERIES SYSTEMS BEYOND LITHIUM-ION BATTERIES

BY

RUIXIAN ZHANG

DISSERTATION

Submitted in partial fulfillment of the requirements
for the degree of Doctor of Philosophy in Chemistry
in the Graduate College of the
University of Illinois Urbana-Champaign, 2021

Urbana, Illinois

Doctoral Committee:

Professor Andrew A. Gewirth, Chair
Professor Catherine J. Murphy
Professor Ralph G. Nuzzo
Associate Professor Joaquín Rodríguez-López

ABSTRACT

The growing market for portable electronic devices and electric vehicles has created an increasing demand for state-of-the-art Li-ion batteries. Meanwhile, alternatives to current Li-ion batteries are proposed to improve battery safety, energy density, C-rate, etc. Approaches towards such alternatives include utilization of novel electrolytes, anode and cathode materials, and metal ion charge carriers in the battery system. The work presented here covers the investigation of several alternative battery systems.

Double Layer Structure in Water-in-Salt Electrolytes. Water-in-Salt Electrolytes (WiSE) are highly concentrated aqueous electrolytes that are of great interest due to their application potential in batteries. The double layer structure of this LiTFSI-based aqueous system is investigated on a charged electrode surface. Potential dependent atomic force microscopy (AFM) reveals the presence of layers, the structure of which changes with applied potential. Larger layers (6.4 Å and 6.7 Å) are observed at positive potentials, associated with $[Li(H_2O)_x]^+([TFSI]^-)_y$ ion pairs, while smaller layers (2.8 Å and 3.3 Å) are found at negative potentials and associated with $[Li(H_2O)_x]^+$ alone. Vibrational spectroscopy shows the potential-dependent compositional change in the double layer, where $[TFSI]^-$ is enriched at positive and $[Li(H_2O)_x]^+$ enriched at negative potentials, respectively. Electrochemical measurements using macroelectrodes and ultramicroelectrodes (UME) reveal a surface-confinement effect for a ferricyanide redox species at the electrode/WiSE interface.

Catalytic Effect of Co Nanoparticles in a Sodium-Sulfur Battery. Room-temperature sodium-sulfur (Na-S) batteries have aroused great interest due to their high energy density and high natural abundance. A new room-temperature Na-S battery system is developed in this work. A MOF-derived Co-containing nitrogen-doped porous carbon (CoNC) is utilized as a catalytic sulfur cathode host. A concentrated sodium electrolyte based on sodium bis(fluorosulfonyl)imide (NaFSI), dimethyoxyethane (DME) and bis(2,2,2-trifluoroethyl) ether (BTFE) is used to facilitate reversible Na electrodepostion and mitigate polysulfide dissolution. The amount of Co present in the CoNC carbon host is tuned by acid-washing. Significant improvement in reversible

sulfur conversion and capacity retention is observed with higher Co-content in CoNC, with 600 mAh/g and 77% capacity retention for CoNC, and 261 mAh/g and 56% capacity retention for acid-washed CoNC at cycle 50 at 80 mAh/g. The catalytic mechanism of Co is investigated. Postmortem XPS, TEM and selected area electron diffraction (SAED) reveals that CoS is formed during cycling in place of Co nanoparticles. Raman spectroscopy suggests that CoS exhibits a catalytic effect on the oxidation of Na_2S.

CoS_2 as a Cathode Material for a Non-Aqueous Zn Battery. CoS_2 is investigated as a cathode material for a non-aqueous Zn battery. A maximum capacity of 283 mAh/g is obtained from a Zn/CoS_2 coin cell. Compositional study reveals a reversible Zn^{2+} intercalation process. X-Ray photoelectron spectroscopy (XPS) reveals an anionic redox activity mediated by reversible interconversions between $2S^{2-}$ (sulfide) and S_2^{2-} (disulfide), which is the first such known case operating in a multivalent system. X-Ray diffraction (XRD) reveals an irreversible phase change upon Zn^{2+} insertion.

ACKNOWLEDGMENTS

I sincerely thank my advisor Prof. Andrew Gewirth, for his guidance throughout my graduate research. His feedbacks and support have truly helped me develop as a researcher. He has also been so kind and understanding, and I am very grateful to have him as my PI.

I thank my committee (Catherine Murphy, Ralph Nuzzo, Joaquín Rodríguez-López), for their guidance and suggestions in my research. I would like to specially thank Prof. Nuzzo for access to facilities in his lab as well as discussions with me on my Zn cathode project.

I thank my collaborators, Mengwei Han and Prof. Rosa Espinosa-Marzal, for their great contribution on the water-in-salt electrolyte project. It has been such a wonderful experience working with them.

I thank Hodge and Erny, from the SCS and physics/MRL machine shop, for their help with designing and building the spectroelectrochemical cell for surface-enhanced infrared absorption spectroscopy, which is of great importance to my water-in-salt electrolyte project.

I thank Dr. Rich Haasch and Dr. Tao Shang, staff scientists at MRL for their help with X-ray photoelectron spectroscopy and gold vapor deposition. Their support has been crucial to my research.

I thank all of the past and current Gewirth group members. I thank Dr. Chengsi Pan for his guidance and suggestions on my Zn cathode project. I have learned a lot about conducting research working with him. I thank Dr. Kim Ta for her contribution to my water-in-salt electrolyte project. She has also contributed a lot to maintaining the glovebox that we share, and it has been great working with her. I thank Annie Esposito for sharing her carbon materials with me and for her contribution to my sodium-sulfur project. I thank Eric Thornburg for assisting me with his expertise in transmission electron microscopy and for his contribution to my sodium-sulfur project. I thank Ken Madsen for his help with a variety of errands in lab. He has been so helpful and friendly, and I really enjoyed discussions with him about research. I thank Xinyi Chen for her support. We joined the lab in the same year and I am really thankful to have gone through graduate school together with her.

Lastly, I thank my parents for their love and support.

TABLE OF CONTENTS

Chapter 1: Introduction

1.1 Introduction to Li-Ion Batteries

Reducing CO_2 emissions from fossil fuel combustion is a major challenge for modern civilization. According to the 2021 Inventory of U.S. Greenhouse Gas Emissions and Sinks by the U.S. Environmental Protection Agency (EPA), in 2019, 4888.5 million metric tons (MMT) of CO_2 emissions are produced from fossil fuel combustion in the U.S., which is 96% of the total CO_2 emissions. Within the CO_2 emissions from fossil fuel combustion, 38% and 33% are ascribed to transportation and electric power.[1]

To solve the heavy fossil fuel consumption and CO_2 emissions of these two energy related activities, new energy storage/consumption systems are under development. Electric vehicles (EVs) and hybrid electric vehicles (HEVs) have greatly impacted the gasoline-based transportation systems, for which batteries are utilized to power electric motors, in place of the fossil fuel-consuming internal combustion engines. In renewable energy harvesting systems, including wind, solar, geo-thermal, etc., batteries can be utilized for grid application. The spread of such combination would reduce the fossil fuel combustion for electricity production.[2]

Since the introduction of the $LiCoO_2$/graphite battery by Sony in 1991, the Li-ion battery has been widely utilized in portable electronics, EVs and various other energy storage applications.[3,4] The Nobel Prize in chemistry in 2019 was awarded to the development of Li-ion batteries, in recognition of the contribution of this crucial technology.[5] A Li-ion battery offers a high gravimetric and volumetric energy density, in comparison with other common battery systems, including lead-acid, nickel-cadmium, and nickel-metal hydride batteries (Figure 1.1). It also does not suffer from memory effect and has low self-discharge rate.[6,7]

Figure 1.2 shows the schematic of a Li-ion battery. The main components include a graphite anode, a $LiCoO_2$ cathode and a liquid electrolyte. During the discharge process, Li^+ leaves/deintercalates from the anode, travels from the anode to the cathode, and inserts/intercalates into the cathode. Oxidation reaction takes place at the anode, and reduction reaction takes place at the cathode. Electrons flow from the anode to the cathode through the external circuit and provide power to a device. During the charge process, external electrons are introduced to the battery, and the reverse process takes place.[8]

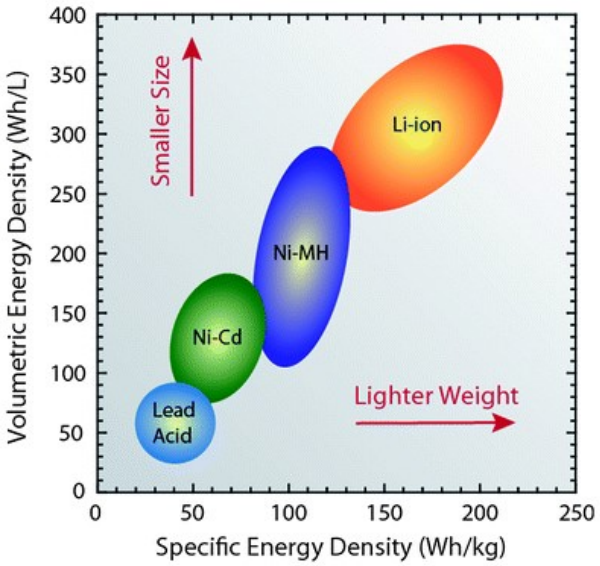

Figure 1.1. Gravimetric and volumetric energy densities in different battery systems.[9]

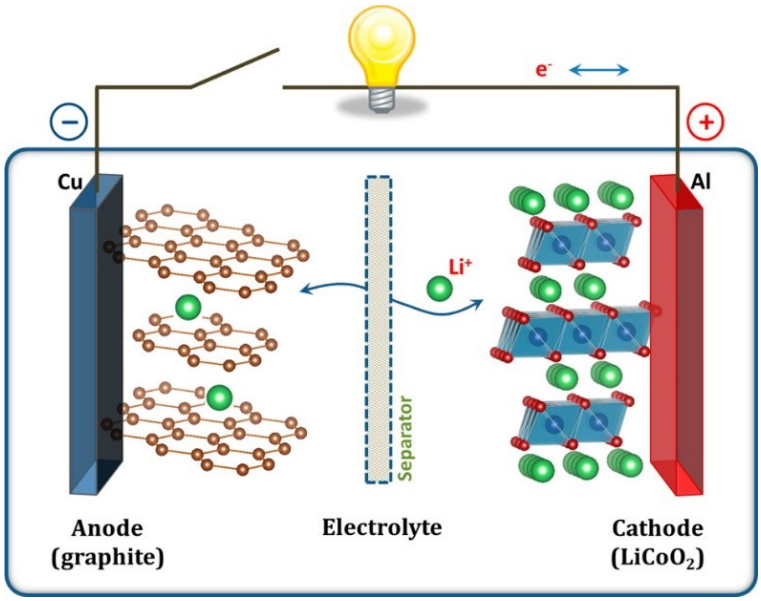

Figure 1.2. The schematic illustration of a $LiCoO_2$/graphite Li-ion battery.[8]

The energy of a Li-ion battery is determined by its voltage V and its capacity/total charge Q ($E = \int_0^Q Vdq$). Greater battery energy would require increasing the voltage and/or capacity of the battery, which are determined by the anode and cathode materials. The voltage of a battery is the reduction potential difference between the cathode and the anode. In a typical Li-ion battery, the anode material is usually graphite, with a reduction potential of -2.84 V vs standard hydrogen electrode (SHE), or 0.2 V vs Li/Li^+. The cathode material is usually a lithium transition metal oxide ($LiCoO_2$, $LiNi_xMn_yCo_{1-x-y}O_2$, $LiMn_2O_4$) or metal phosphate ($LiFePO_4$) with a metal redox center, and its reduction potential ranges from 3.6 to 4.2 V vs Li/Li^+ (Figure 1.3).[10] The corresponding voltage of a battery is 3.4 - 4.0 V. Li^+ intercalation into metal oxides and metal phosphates involves Li^+ entering the material, traveling and residing in the vacancies of channels/layers within the crystal structure. The capacity of a battery is the total charge that can be stored/delivered in the electrode material. and is determined by the number of Li^+ intercalation/reversible redox reactions that can be delivered from the electrode material.[8,2]

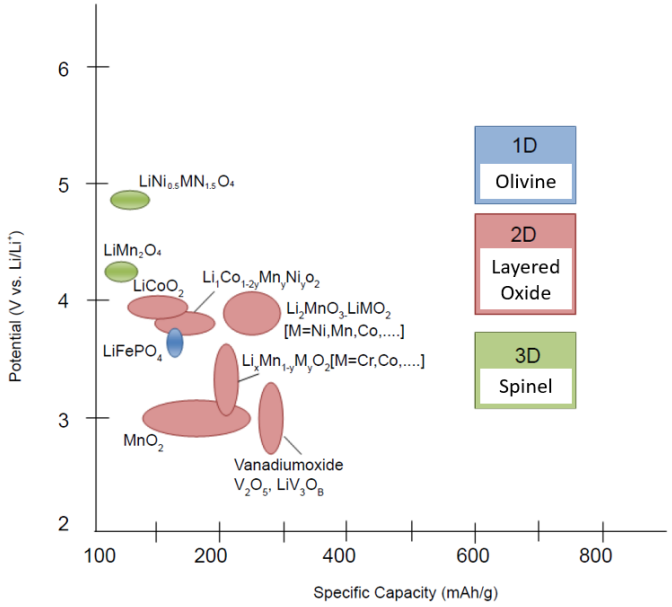

Figure 1.3. Voltage and specific capacity of different cathode materials.[10]

The liquid electrolyte is typically a 1 M lithium salt solution in one or several organic solvents. The selection of the lithium salt and organic solvents is based on the Li^+ transportation performance as well as the stability of the electrolyte within the battery operation voltage. The most common electrolyte utilized is 1 M $LiPF_6$ in cyclic ethylene carbonate (EC) and linear carbonate (dimethyl carbonate DMC or diethyl carbonate DEC) 1:1 solvent mixture, which has a high ionic conductivity of ~ 10^{-2} S/cm. EC, upon cycling, would reductively decompose and form a Li^+-conducting/electron-insulating passivation layer on the anode surface, which is called the solid electrolyte interface (SEI). Such SEI prevents further decomposition or side reactions to occur and allows stable cycling of a battery.[8,11,12]

1.2 Limitations of Li-Ion Batteries

The operation of a Li-ion battery is realized by the above-mentioned anode, cathode and electrolyte. At the same time, its energy density and physicochemical properties are limited by

these three components. On the anode side, graphite is most commonly utilized. Graphite bears a gravimetric capacity of 760 mAh/g, and a volumetric capacity of 372 mAh/mL, which are much lower compared with a Li metal anode (3861 mAh/g and 2062 mAh/mL).[13,14] Cathode materials are typically lithium transition metal oxides and phosphates, including $LiCoO_2$, $LiNi_xMn_yCo_{1-x-y}O_2$, $LiMn_2O_4$, $LiFePO_4$, etc. The gravimetric capacity of these intercalation cathodes ranges from 120 - 180 mAh/g (Figure 1.3), which is limited by the number of available sites for interaction in the transition metal oxides.[2,15] Due to the capacity limitation of the anode and cathode, the theoretical energy density of a Li-ion battery can at most go up to ~ 420 Wh/kg or ~ 1400 Wh/L, and the practical energy density is currently ~ 200 Wh/kg and ~350 Wh/L.[16,17] Meanwhile, the utilization of a liquid electrolyte containing an organic solvent raises safety issue, with the highly flammable carbonates being a major contributor to Li-ion battery thermal runaway and consequent fire incidents.[18] The Li and transition metal elements (Co, Ni, Mn) content in the Li-ion battery results in a high energy cost.[19] The high demand for these elements also leads to over-exploitation and child labor issues.[20] Due to such limitations, various alternative battery systems have been proposed and developed, in order to out-perform a Li-ion battery in certain aspects.

1.3 Alternative Battery Systems

1.3.1 Concentrated Electrolytes

Concentrated electrolytes have been receiving increasing attention. Such electrolytes contain a high salt-to-solvent ratio, and their concentrations usually range from 3 to 5 M. Due to the high lithium salt composition, the solvent molecules would participate in the coordination of Li^+, and the number of free solvent molecules dramatically decreases. As a result, the solvation,

or ion/ion and ion/solvent interaction differs greatly from a dilute electrolyte, and the concentrated electrolytes bear unique properties and could be utilized to improve the performance of a Li-ion battery (Figure 1.4).[21]

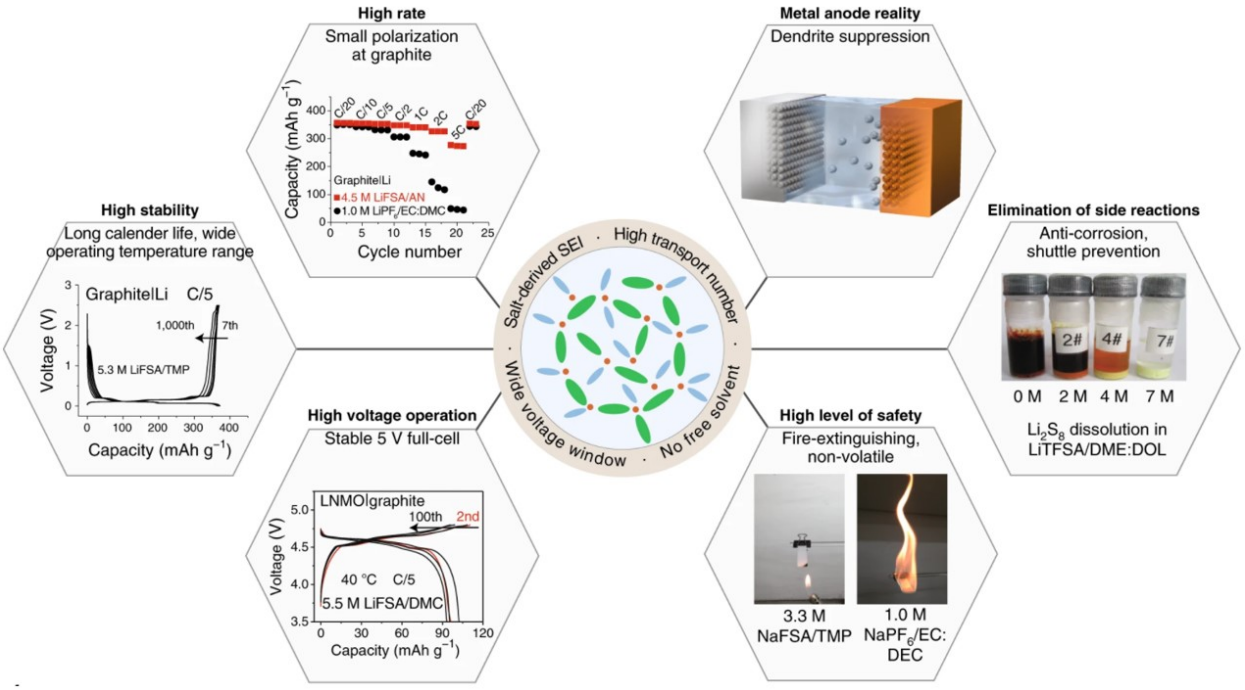

Figure 1.4. Structure of a concentrated electrolyte (central circle), its physicochemical and electrochemical properties (outer circle), and various functions in advanced batteries (outer hexagons).[21]

Due to a different solvation/ion-ion interaction, the anion in the concentrated electrolytes can have a upshift in its lowest unoccupied molecular orbital (LUMO). This change in LUMO can lead to a preferred reductive decomposition of the anion instead of solvent in the electrolyte at a reducing potential, and thus an SEI with different composition from the dilute electrolyte can be formed. Such as SEI can more effectively prevent the decomposition of the electrolyte, and promote battery cycle stability. The unique SEI can also promote stable and dendrite-free cycling of a metal anode, which is incompatible with a dilute electrolyte due to continuous

decomposition and dendrite formation. The ion-solvent interaction leads to a downshift in the highest occupied molecular orbital (HOMO) of the solvent molecule. This interaction, along with the lack of free solvent, can inhibit the oxidative decomposition of the solvent molecule at a positive potential, and allow battery cycling at higher voltage. The lack of free solvent also lowers the solubilization ability of the electrolyte compared with the dilute electrolyte, and that prevents the dissolution and corrosion of electrode materials and battery components. And with the organic solvent decreasing in composition, the flammability of the electrolyte is reduced and the safety of a battery can be improved.[21]

Among the concentrated electrolytes, water-in-salt electrolytes (WiSE) have attracted wide attention.[22,23] These electrolytes utilize H_2O as the solvent instead of flammable organic solvents, further reducing the flammability of the electrolyte. The addition of high concentration lithium salts (including: LiTFSI, LiOTF, LiFSI, etc.) allows coordination of H_2O molecules to Li^+ cations and produces a passivating SEI, which inhibits H_2O decomposition reactions and greatly expands the electrolyte stability window.[24,25] WiSE is considered a promising electrolyte for use in next-generation aqueous Li-ion batteries.

1.3.2 Beyond Li-Ion

The growing market for Li-ion batteries raises the demand for Li. Given a 5 % increase in Li consumption per year, current mineable Li resources could only sustain about 65 years without recycling.[26] Alternative metal ions, which are cheaper and more natural abundant, are proposed to be replace Li^+ as the charge carrier in a battery. Sodium appears to be a promising candidate. Sodium is the fourth most abundant element on earth. It is also much cheaper

compared with Li ($0.2/kg for Na_2CO_3 vs $6.75/kg for Li_2CO_3, Table 1.1).[27] A Na-ion battery would be a cost-effective candidate for mass battery application.

Table 1.1. Price of Na_2CO_3, Li_2CO_3, S, Ni, Co, and Mn.[27,32]

Data from 2019	Na_2CO_3	Li_2CO_3	S	Ni	Co	Mn
Price ($/kg)	0.2	6.75	0.05	18	37	3

The limited space available for battery mounting in certain applications also calls for greater volumetric energy density in a battery (Figure 1.5). Multivalent batteries have been proposed, whose anode utilizes Zn, Mg, and Al, etc. These multivalent metal anodes contain much higher volumetric capacity (5851 mAh/mL for Zn, 3832 mAh/mL for Mg, and 8046 mAh/mL for Al) compared with graphite (372 mAh/mL) and Li metal (2062 mAh/mL). These metals are also less reactive towards air than Li metal, which could promote safety and alleviates processing complexity for batteries with a metal anode.[13,14]

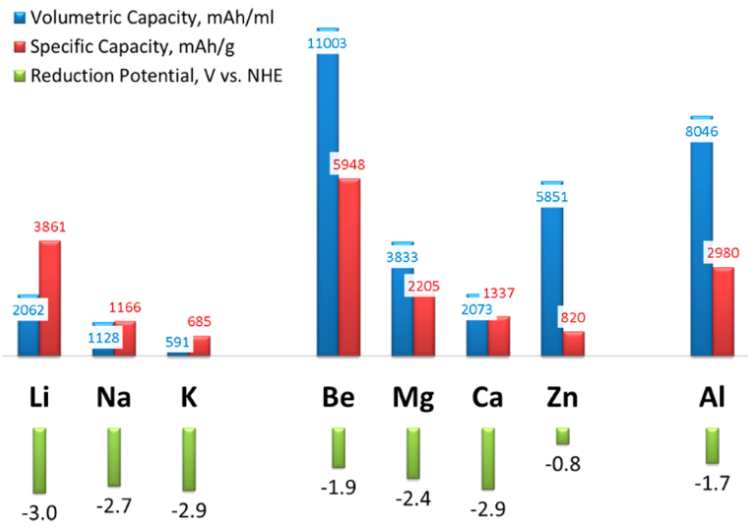

Figure 1.5. Capacities and reductive potentials for various metal anodes.[14]

1.3.3 Alternative Cathode Materials

For intercalation transition metal oxides and phosphates cathodes, the gravimetric/volumetric capacity is limited by their sites available for topotactic insertion in their crystal structure per unit mass/volume. To increase the capacity, alternative cathode materials with charge storage mechanisms different from intercalation are investigated.[28] Conversion electrodes have attracted wide interests. Sulfur is one of the most popular candidates for conversion cathode materials. By utilizing the conversion reactions of S ($2Li^+ + S + 2e^- \rightarrow Li_2S$), the restrictions on number of intercalation sites in the crystal structure is lifted. The S redox couple center is also much lighter than Co/Ni/Mn, and thus a much greater capacity can be obtained in the conversion electrode.[29] The theoretical gravimetric capacity for S is 1675 mAh/g, which is over 8 times of that of a typical metal oxide cathode. By replacing the intercalation cathode with S cathode, the theoretical energy density of a Li-S battery (Figure 1.6) can reach ~ 2500 Wh/kg and ~ 2800 Wh/L, which is much greater than the limit of a Li-ion battery.[30,31] S is also much cheaper and more earth abundant compared with the transition metal elements in the intercalation cathodes (Table 1.1).[32] Therefore, S is particularly attractive as an alternative cathode material to realize low-cost and large-scale battery application. Among the sulfur batteries, room-temperature Na-S batteries are desirable due to the higher natural abundance of Na relative to Li and expected low operation cost.[33] With a high theoretical specific energy of 1274 Wh/kg on a Na and S basis, room-temperature Na-S batteries would be a promising alternative to Li-based energy storage devices.[34]

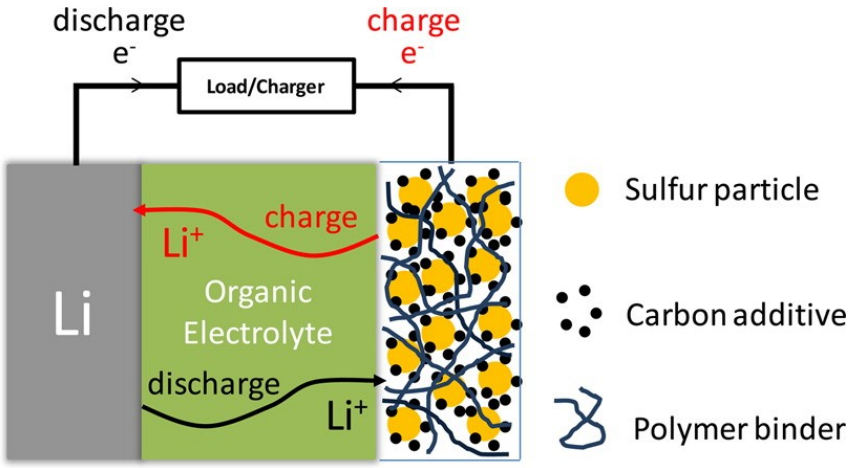

Figure 1.6. Schematic diagram of a Li-S battery.[29]

Anionic-redox cathode materials have also drawn considerable attention. These materials are usually transition metal oxides and sulfides (Li_3RuO_4, CoS_2, etc.). In contrast to traditional transition metal oxide cathodes, where only metal redox centers are present, these cathodes exhibit redox activity on the anions (oxide or sulfide). Such an anionic-redox activity contributes to higher capacity and energy density.[35,36] The study of anionic-redox cathode materials in multivalent battery systems is limited.

My graduate research focuses on these alternative battery systems. Chapter 2 investigated the double layer structure of the concentrated aqueous Li electrolytes/WiSE and the consequent electrochemical properties of the system. A layered double layer structure was observed for the first time in concentrated electrolyte systems, along with its confinement effect on redox species on the electrode surface. Chapter 3 developed a Na-S battery utilizing of a concentrated Na electrolyte and a Co nanoparticle-containing catalytic porous carbon host. Mechanistic studies revealed a conversion of Co nanoparticle to CoS during cycling, and the catalytic effect of CoS on S cathode. Chapter 4 studied CoS_2 as a novel cathode material for non-aqueous Zn batteries.

Reversible anionic sulfur redox activity was observed for the first time in a multivalent battery system.

1.4 References

1. *Inventory of U.S. Greenhouse Gas Emissions and Sinks: 1990-2019*; United States Environmental Protection Agency: Washington D.C., 2021.

2. Nitta, N.; Wu, F.; Lee, J. T.; Yushin, G., Li-Ion Battery Materials: Present and Future. *Mater. Today* **2015,** *18*, 252-264.

3. Manthiram, A., An Outlook on Lithium Ion Battery Technology. *ACS Cent. Sci.* **2017,** *3*, 1063-1069.

4. Li, J.; Du, Z.; Ruther, R. E.; An, S. J.; David, L. A.; Hays, K.; Wood, M.; Phillip, N. D.; Sheng, Y.; Mao, C.; Kalnaus, S.; Daniel, C.; Wood, D. L., Toward Low-Cost, High-Energy Density, and High-Power Density Lithium-Ion Batteries. *JOM* **2017,** *69*, 1484-1496.

5. Hu, Y.-S.; Lu, Y., 2019 Nobel Prize for the Li-Ion Batteries and New Opportunities and Challenges in Na-Ion Batteries. *ACS Energy Lett.* **2019,** *4*, 2689-2690.

6. Sasaki, T.; Ukyo, Y.; Novák, P., Memory Effect in a Lithium-Ion Battery. *Nature Mater.* **2013,** *12*, 569-575.

7. Sloop, S. E.; Kerr, J. B.; Kinoshita, K., The Role of Li-Ion Battery Electrolyte Reactivity in Performance Decline and Self-Discharge. *J. Power Sources* **2003,** *119-121*, 330-337.

8. Goodenough, J. B.; Park, K.-S., The Li-Ion Rechargeable Battery: A Perspective. *J. Am. Chem. Soc.* **2013,** *135*, 1167-1176.

9. Tarascon, J. M.; Armand, M., Issues and Challenges Facing Rechargeable Lithium Batteries. *Nature* **2001,** *414*, 359-367.

10. Bensalah, N.; Dawood, H., Review on Synthesis, Characterizations, and Electrochemical Properties of Cathode Materials for Lithium Ion Batteries *J. Material Sci. Eng.* **2016,** *5*, 258.

11. Liu, C.; Neale, Z. G.; Cao, G., Understanding Electrochemical Potentials of Cathode Materials in Rechargeable Batteries. *Mater. Today* **2016,** *19*, 109-123.

12. Bachman, J. C.; Muy, S.; Grimaud, A.; Chang, H.-H.; Pour, N.; Lux, S. F.; Paschos, O.; Maglia, F.; Lupart, S.; Lamp, P.; Giordano, L.; Shao-Horn, Y., Inorganic Solid-State Electrolytes for Lithium Batteries: Mechanisms and Properties Governing Ion Conduction. *Chem. Rev.* **2016,** *116*, 140-162.

13. Yoo, H. D.; Shterenberg, I.; Gofer, Y.; Gershinsky, G.; Pour, N.; Aurbach, D., Mg Rechargeable Batteries: An On-Going Challenge. *Energy Environ. Sci.* **2013,** *6*, 2265-2279.

14. Muldoon, J.; Bucur, C. B.; Gregory, T., Quest for Nonaqueous Multivalent Secondary Batteries: Magnesium and Beyond. *Chem. Rev.* **2014,** *114*, 11683-11720.

15. Goodenough, J. B.; Kim, Y., Challenges for Rechargeable Li Batteries. *Chem. Mater.* **2010,** *22*, 587-603.

16. Yang, Y.; Zheng, G.; Cui, Y., Nanostructured Sulfur Cathodes. *Chem. Soc. Rev.* **2013,** *42*, 3018-3032.

17. Adelhelm, P.; Hartmann, P.; Bender, C. L.; Busche, M.; Eufinger, C.; Janek, J., From Lithium to Sodium: Cell Chemistry of Room Temperature Sodium–Air and Sodium–Sulfur Batteries. *Beilstein J. Nanotechnol.* **2015,** *6*, 1016-1055.

18. Feng, X.; Ouyang, M.; Liu, X.; Lu, L.; Xia, Y.; He, X., Thermal Runaway Mechanism of Lithium Ion Battery for Electric Vehicles: A Review. *Energy Storage Mater.* **2018,** *10*, 246-267.

19. Tian, Y.; Zeng, G.; Rutt, A.; Shi, T.; Kim, H.; Wang, J.; Koettgen, J.; Sun, Y.; Ouyang, B.; Chen, T.; Lun, Z.; Rong, Z.; Persson, K.; Ceder, G., Promises and Challenges of Next-Generation "Beyond Li-Ion" Batteries for Electric Vehicles and Grid Decarbonization. *Chem. Rev.* **2021,** *121*, 1623-1669.

20. Banza Lubaba Nkulu, C.; Casas, L.; Haufroid, V.; De Putter, T.; Saenen, N. D.; Kayembe-Kitenge, T.; Musa Obadia, P.; Kyanika Wa Mukoma, D.; Lunda Ilunga, J.-M.; Nawrot, T. S.; Luboya Numbi, O.; Smolders, E.; Nemery, B., Sustainability of Artisanal Mining of Cobalt in DR Congo. *Nat. Sustain.* **2018,** *1*, 495-504.

21. Yamada, Y.; Wang, J.; Ko, S.; Watanabe, E.; Yamada, A., Advances and Issues in Developing Salt-Concentrated Battery Electrolytes. *Nat. Energy* **2019,** *4*, 269-280.

22. Suo, L.; Borodin, O.; Gao, T.; Olguin, M.; Ho, J.; Fan, X.; Luo, C.; Wang, C.; Xu, K., "Water-in-Salt" Electrolyte Enables High-Voltage Aqueous Lithium-Ion Chemistries. *Science* **2015,** *350*, 938-943.

23. Borodin, O.; Suo, L.; Gobet, M.; Ren, X.; Wang, F.; Faraone, A.; Peng, J.; Olguin, M.; Schroeder, M.; Ding, M. S.; Gobrogge, E.; von Wald Cresce, A.; Munoz, S.; Dura, J. A.; Greenbaum, S.; Wang, C.; Xu, K., Liquid Structure with Nano-Heterogeneity Promotes Cationic Transport in Concentrated Electrolytes. *ACS Nano* **2017,** *11*, 10462-10471.

24. Zheng, J.; Tan, G.; Shan, P.; Liu, T.; Hu, J.; Feng, Y.; Yang, L.; Zhang, M.; Chen, Z.; Lin, Y.; Lu, J.; Neuefeind, J. C.; Ren, Y.; Amine, K.; Wang, L.-W.; Xu, K.; Pan, F., Understanding Thermodynamic and Kinetic Contributions in Expanding the Stability Window of Aqueous Electrolytes. *Chem* **2018,** *4*, 2872-2882.

25. Wang, F.; Borodin, O.; Gao, T.; Fan, X.; Sun, W.; Han, F.; Faraone, A.; Dura, J. A.; Xu, K.; Wang, C., Highly Reversible Zinc Metal Anode for Aqueous Batteries. *Nat. Mater.* **2018,** *17*, 543-549.

26. Pan, H.; Hu, Y.-S.; Chen, L., Room-Temperature Stationary Sodium-Ion Batteries for Large-Scale Electric Energy Storage. *Energy Environ. Sci.* **2013,** *6*, 2338-2360.

27. Hwang, J.-Y.; Myung, S.-T.; Sun, Y.-K., Sodium-Ion Batteries: Present and Future. *Chem. Soc. Rev.* **2017,** *46*, 3529-3614.

28. Kim, J.; Kim, H.; Kang, K., Conversion-Based Cathode Materials for Rechargeable Sodium Batteries. *Adv. Energy Mater.* **2018,** *8*, 1702646.

29. Manthiram, A.; Fu, Y.; Chung, S.-H.; Zu, C.; Su, Y.-S., Rechargeable Lithium–Sulfur Batteries. *Chem. Rev.* **2014,** *114*, 11751-11787.

30. Li, T.; Bai, X.; Gulzar, U.; Bai, Y.-J.; Capiglia, C.; Deng, W.; Zhou, X.; Liu, Z.; Feng, Z.; Proietti Zaccaria, R., A Comprehensive Understanding of Lithium–Sulfur Battery Technology. *Adv. Funct. Mater.* **2019,** *29*, 1901730.

31. Seh, Z. W.; Sun, Y.; Zhang, Q.; Cui, Y., Designing High-Energy Lithium–Sulfur Batteries. *Chem. Soc. Rev.* **2016,** *45*, 5605-5634.

32. Rosenman, A.; Markevich, E.; Salitra, G.; Aurbach, D.; Garsuch, A.; Chesneau, F. F., Review on Li-Sulfur Battery Systems: an Integral Perspective. *Adv. Energy Mater.* **2015,** *5*, 1500212.

33. Wang, Y.-X.; Zhang, B.; Lai, W.; Xu, Y.; Chou, S.-L.; Liu, H.-K.; Dou, S.-X., Room-Temperature Sodium-Sulfur Batteries: A Comprehensive Review on Research Progress and Cell Chemistry. *Adv. Energy Mater.* **2017,** *7*, 1602829.

34. Xin, S.; Yin, Y.-X.; Guo, Y.-G.; Wan, L.-J., A High-Energy Room-Temperature Sodium-Sulfur Battery. *Adv. Mater.* **2014,** *26*, 1261-1265.

35. Li, H.; Ramakrishnan, S.; Freeland, J. W.; McCloskey, B. D.; Cabana, J., Definition of Redox Centers in Reactions of Lithium Intercalation in Li_3RuO_4 Polymorphs. *J. Am. Chem. Soc.* **2020,** *142*, 8160-8173.

36. Li, M.; Liu, T.; Bi, X.; Chen, Z.; Amine, K.; Zhong, C.; Lu, J., Cationic and Anionic Redox in Lithium-Ion Based Batteries. *Chem. Soc. Rev.* **2020,** *49*, 1688-1705.

Chapter 2: Potential Dependent Layering in the Electrochemical Double Layer of Water-in-Salt Electrolytes

2.1 Introduction

New electrolytes can enable new chemistries and opportunities for Li-based batteries.[1,2,3] Concentrated electrolytes have emerged as promising candidates.[4] These electrolytes contain a high salt-to-solvent ratio, as opposed to that of dilute electrolytes, and the number of free solvent molecules decreases due to coordination with Li^+ cations.[5,6] This high salt concentration and lack of free solvent molecules leads to improved electrolyte properties, such as faster Li^+ transport, an extended stability window, and a unique passivating solid-electrolyte interface (SEI).[7,8]

Among the concentrated electrolytes, water-in-salt electrolytes (WiSE) have attracted wide attention.[5,9] These electrolytes utilize H_2O as the solvent instead of flammable organic solvents. The addition of high concentration lithium salts (including: LiTFSI, LiOTF, LiFSI, etc.) allows coordination of H_2O molecules to Li^+ cations and produces a passivating SEI, which inhibits H_2O decomposition reactions and greatly expands the electrolyte stability window.[10,11] WiSE is considered a promising electrolyte for use in next-generation Li-ion batteries.

The electrical double layer formed by the WiSE at the solid-liquid interface is of great interest. Computational studies have investigated the change in the WiSE double layer with

potential.[12,13,14] Molecular dynamics (MD) simulations suggest that H_2O is depleted from the double layer when the electrode surface is positively biased, and enhanced when the electrode is negatively charged.[12] While substantial work investigates the bulk structure of WiSE and related electrolytes, experimental verification of the effect of potential on the double layer for WiSE is limited, with one surface enhanced infrared absorption spectroscopy (SEIRAS) study on mixed WiSE consisting of 21 m LiTFSI and 7 m LiOTf to investigate the preferred anion comprising the double layer.[9,15,16] This paucity of work stands in contrast to the considerable experimental effort examining the electrochemical double layer in dilute aqueous electrolytes.[17,18] Therefore, a study on the electrical double layer of WiSE would be informative in terms of understanding the electrode-WiSE interface.

Atomic force microscopy (AFM) can be utilized to probe double layer structure with changing potential.[19,20] Prior studies used potential-dependent AFM measurements on ionic liquids to show a layered double layer structure varying with potential.[21] AFM force curves also provides information on the composition of the double layer.[22,23]

The electrochemical behavior of small molecules in the WiSE is also of interest. The solvation environment of the WiSE system differs greatly from that of a dilute electrolyte, and its effect on processes including redox kinetics and diffusion remains to be explored.[5,9] Ultramicroelectrodes (UMEs) have been utilized to probe redox processes, and would be useful in understanding the difference between WiSE and dilute electrolyte in terms of the WiSE interaction with redox species.[24,25,26]

In this work, we use AFM, UME, and vibrational spectroscopy to probe changes at an electrode/WiSE interface. A layered double layer structure is observed on a (111) textured Au surface in AFM, and the layered-structure and consequently surface excess of electrolyte

components varies with potential. Spectroscopy coupled with AFM illuminates the composition of the double layer at different potentials. $[TFSI]^-$ and $[Li(H_2O)_x]^+([TFSI]^-)_y$ clusters are the predominant species at positive potentials and $[Li(H_2O)_x]^+$ comprises the double layer at negative potentials. In addition, electrochemical characterization reveals the presence of a surface-confinement effect for a ferricyanide ($[Fe(CN)_6]^{3-}/[Fe(CN)_6]^{4-}$) redox couple, possibly due to interaction with the strongly layered WiSE electrolyte structure.

2.2 Methods

2.2.1 Electrolyte Preparation

Lithium bis(trifluoromethane sulfonyl) imide (LiTFSI, 99.95 %, Sigma-Aldrich) was stored in an Ar-filled glovebox, which contained < 1ppm of O_2 and < 1 ppm of H_2O, before use. All electrolytes were purged with dry N_2 before measurements. Aqueous LiTFSI solutions of various molality (mol LiTFSI/kg H_2O) were prepared with Milli-Q water. 1 m and 21 m solutions were prepared by dissolving LiTFSI in H_2O.

1 mM and 5 mM potassium ferricyanide ($K_3Fe(CN)_6$, > 99%, Sigma-Aldrich) solutions were prepared by diluting 20 mM $K_3Fe(CN)_6$ stock solution with 1 m and 21 m LiTFSI solutions in volume ratios of 1 : 9 and 1 : 3 respectively.

2.2.2 Electrochemical Characterization

All electrochemical measurements were carried out using a CH Instruments 760D potentiostat (Austin, TX). A polycrystalline Au disk electrode (0.875 cm diameter) and a Pt ultramicroelectrode (UMEs, 10 μm diameter, CH Instruments, Austin, Texas) were used as working electrodes. A Au wire and a Ag wire were used as counter electrode and reference

electrode, respectively. Potentials are reported vs. Ag/Ag^+. The polycrystalline Au disk electrode was polished mechanically, followed by rinsing, with 9.0, 3.0, 0.25, and 0.05 μm MetaDi Monocrystalline Diamond Suspension (Buehler) on a MicroCloth polishing pad (Buehler). The Au disk was then annealed with a hydrogen flame, quenched in Milli-Q water, and dried under vacuum. The Pt UME was polished mechanically, followed by rinsing, with 3.0, 1.0, 0.5, and 0.25 μm MetaDi Monocrystalline Diamond Suspension (Buehler) on a MicroCloth polishing pad (Buehler) and electrochemically in a 0.1 M HNO_3 electrolyte by sweeping the potential from 2.0 to −0.5 V (vs Ag/AgCl) for 10 cycles prior use. Electrochemical impedance spectroscopy (EIS) was performed on a Biologic potentiostat (Model SP-150, France). The alternating current (AC) perturbation signal was ±10 mV and the frequency ranged from 100 mHz to 1 MHz. Differential capacitance was derived from EC-Lab software. COMSOL Multiphysics 5.3 simulation procedures were previously described.[25]

2.2.3 Raman Spectroscopy and Surface Enhanced Raman Spectroscopy (SERS)

Raman spectra were obtained by using a 632.8 nm He/Ne laser and the instrumental setup described previously.[27] The spectral resolution was calculated to be 3.0−3.3 cm^{-1} using a 50 μm slit. For bulk Raman spectroscopy, the electrolytes were placed in 20 mL scintillation vials.

Surface enhanced Raman spectroscopy (SERS) was carried out in a home-built cell described previously.[27] A polycrystalline Au disk electrode (0.875 cm diameter) was used as the working electrode. A Au wire and a Ag wire were used as the counter and reference electrodes, respectively. The Au disk was mechanically polished and annealed under the same procedure as described above. The Au disk was then electrochemically roughened in 0.1 M KCl as previously described.[28]

2.2.4 Attenuated Total Reflectance Surface Enhanced Infrared Absorption Spectroscopy (ATR-SEIRAS)

Attenuated total reflectance surface enhanced infrared absorption spectroscopy (ATR-SEIRAS) was carried out in a Nicolet Magna-IR 550 spectrometer using a home-built spectro-electrochemical cell similar to that described previously.[29] A μ-groove Si wafer (IRUBIS GmbH, Germany) is used as the internal reflectance element.[30] The Si wafer was polished for 15 mins with 3 and 0.25 μm MetaDi Monocrystalline Diamond Suspension (Buehler) on a MicroCloth polishing pad (Buehler). The Si wafer was rinsed and sonicated for 15 mins with Milli-Q water before and after polishing, and dried under N_2. A 20 nm thick Au film was evaporated on the Si wafer with a deposition rate of 0.01 nm/s in a Temescal E-beam evaporator. The 20 nm Au film was cleaned by cycling in 0.1 M H_2SO_4 between -0.5 V to 0.9 V vs Ag/Ag^+ for 20 cycles at 20 mV/s and used as the working electrode.[31] A Au wire and a Ag wire were used as the counter and reference electrodes, respectively. A Pike Technologies VeeMAX III ATR accessory provided control over angle of incidence. The angle of incidence is 35°. Potential dependent spectra were collected between 0.4 V and -0.5 V vs Ag/Ag^+. The resolution was 4 cm^{-1}. The reference spectrum was collected at 0.4 V vs Ag/Ag^+.

2.2.5 Atomic Force Microscopy (AFM)

Force measurements were conducted in a JPK (Santa Barbara, CA) atomic force microscope (AFM) equipped with CSC-37 tips (MikroMasch, CA), with spring constants of ~0.6 N/m as determined by the thermal noise method and a nominal radius of ca. 20 nm.[32] The tip was exposed to UV for 20 minutes prior to the measurement. Au on glass samples were purchased

from Phasis (Geneva, Switzerland) and were flame-annealed by the manufacturer to achieve a (111) texture. The surface was rinsed with Millipore water and ethanol, dried under N_2 and exposed to UV light for 20 minutes. The process was repeated twice, after which the surface was immediately mounted into the electrochemical cell. The cell was capped with a Teflon cover to minimize the exchange of water between solution and ambient air (maximum weight gain =3.1 wt.% at 33 % RH). The TFSI solution was filtered by using a 200 nm pore size PTFE membrane prior to the injection into the electrochemical cell. The system was equilibrated for 20 minutes before force and electrochemical measurements. AFM force measurements were obtained at the open circuit potential (OCP), +0.3, and -0.4 V against a Ag pseudo reference electrode. Electrochemical potential was applied using a CHI potentiostat. The tip velocity was set at 20 nm/s. A total of 64 force curves at each potential were collected from a 500 nm x 500 nm area by dividing the area into 64 separate squares and collecting a force curve from each square.

2.3 Results

2.3.1 Electrochemical Characterization

Figure 2.1a shows cyclic voltammograms (CVs) obtained from a Au disk electrode (d = 0.875 cm) immersed in a solution containing 1 mM $K_3Fe(CN)_6$ in 1 m LiTFSI at scan rates of 5 mV/s, 10 mV/s, 20 mV/s, 50 mV/s and 100 mV/s. The CV curves show reduction peaks at 0.09 V and oxidation peaks at 0.15 V vs. Ag/Ag^+, with a peak separation of 60 mV. The CVs correspond well to a diffusion-controlled reversible $[Fe(CN)_6]^{3-}$/ $[Fe(CN)_6]^{4-}$ faradaic process with an $E^0 = 0.12$ V vs. Ag/Ag^+.[33]

Figure 2.1b shows the CVs obtained from a Au electrode immersed in 1 mM $K_3Fe(CN)_6$ in 21 m LiTFSI at the same scan rates. The CV shows that the reduction and oxidation peaks are

at 0.24 V and 0.28 V respectively. The resulting separation between the two peaks is 40 mV, which is smaller than the 57 mV separation expected for a diffusion-controlled reversible faradaic process.[33] The smaller peak separation is typically associated with a surface-confined reversible redox process.[34] The redox potential shifts to an apparent $E^0 = 0.26$ V, which could be due to a change in the solvation structure of $[Fe(CN)_6]^{3-}$, or a change in the Ag/Ag^+ reference potential. Little discussion attends changes in this reference potential in highly concentrated electrolytes such as that used here. The use of an additional test redox couple is similarly complicated. A Ag pseudo-electrode has been reported to exhibit little potential drift in non-aqueous systems.[35] On the other hand, similar shift in the redox potential of a redox couple has been reported when using Li^+ and K^+-containing supporting electrolytes, due to different solvating interactions.[36] Therefore, we consider the change in solvation structure as the major contributor to the redox potential shift, which we will further discuss using Raman spectroscopy. Compared with the 1 m LiTFSI, the CVs exhibit more of a rectangular shape at the reversal potentials (0 V and 0.35 V vs. Ag/Ag^+). This rectangular shape in the CVs suggests the system may have increased capacitive character.[37]

Figure 2.1c shows linear plots of natural logarithm of peak current densities of $[Fe(CN)_6]^{3-}$ reduction versus natural logarithm of scan rates. In 1 m LiTFSI, the plot exhibits a slope of 0.51, which is characteristic of a diffusion-controlled reversible faradaic process, governed by the Randles-Sevcik equation.[38] In contrast, the plot for 21 m LiTFSI exhibits a slope of 0.80, which suggests a contribution from capacitive current and/or a surface-confined redox process.[34,37]

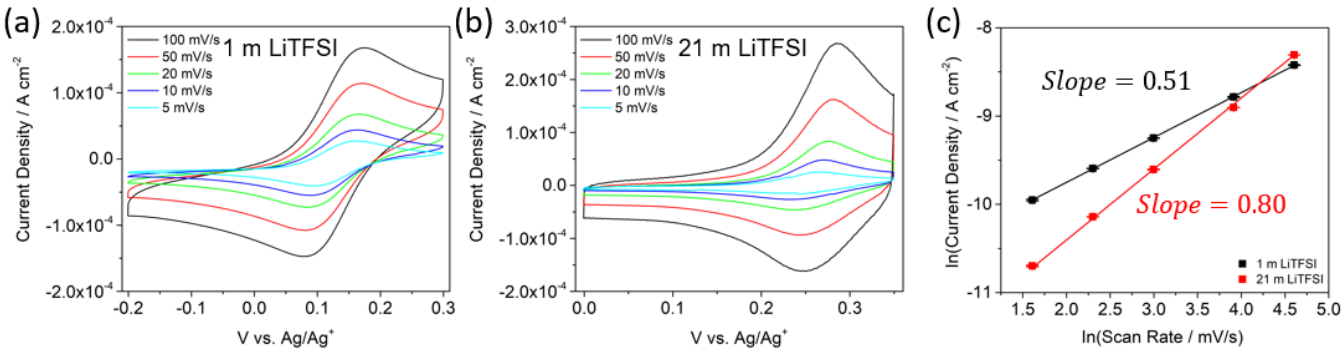

Figure 2.1. CVs obtained from a Au disk electrode (d = 0.875 cm) in 1 mM $K_3Fe(CN)_6$ in (a) 1 m LiTFSI, and (b) 21 m LiTFSI at different scan rates, and (c) the plot of ln(peak reduction current density) versus ln(scan rate) derived from corresponding CVs.

To understand the capacitance contribution to the system, we carried out electrochemical impedance spectroscopy (EIS, Figure 2.2) and obtained differential capacitance C_p (Figure 2.3) from 1 m LiTFSI and 21 m LiTFSI using the same electrodes. Here we note that capacitance can take a wide range of values both in experiment and simulation.[14,39] The capacitance values obtained in this work are comparable to those reported for dilute aqueous systems and ionic liquids in previous studies.[40,41] The 21 m LiTFSI system exhibits higher differential capacitance compared to the 1 m LiTFSI, supporting the presence of a greater capacitance contribution in the 21 m TFSI. Indeed, previous studies have utilized 21 m LiTFSI as an electrolyte for supercapacitors.[42,43] The differential capacity at 1 Hz (Figure 2.3a) exhibits a weak minimum at ca. -0.1 V which is typically associated with the potential of zero charge (pzc). The pzc found here is consistent with that measured on Au in other systems.[44] While the capacitance contribution in the 21 m LiTFSI system could lead to the 0.80 slope in the linear plot of ln(current density) vs. ln(scan rate), the 40 mV peak separation for $[Fe(CN)_6]^{3-}$ reduction/oxidation peaks in the CVs suggests the presence of a surface-confined redox process.

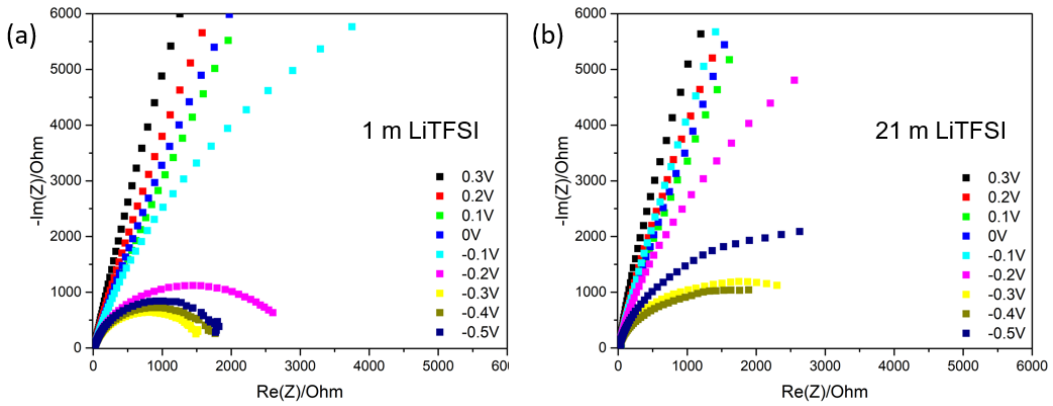

Figure 2.2. Nyquist plots of (a) 1 m LiTFSI and (b) 21 m LiTFSI with a Au disk working electrode at various potential vs. Ag/Ag^+.

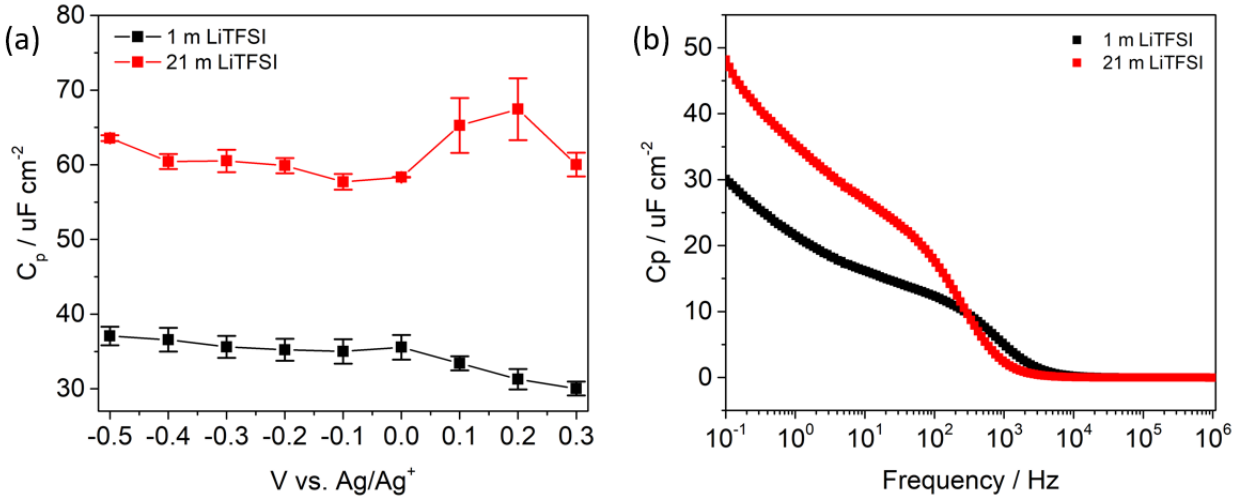

Figure 2.3. Capacitance obtained from a fit to the Nyquist plots above for 1 m LiTFSI and 21 m LiTFSI at (a) 1 Hz at various potentials vs. Ag/Ag^+, and (b) at various frequencies at 0 V vs. Ag/Ag^+.

To investigate the presence of putative surface-confinement in $[Fe(CN)_6]^{3-}$ in 21 m LiTFSI, we carried out cyclic voltammetry using a Pt UME (d = 25 μm). Figure 2.4a shows CVs obtained in 5 mM $K_3Fe(CN)_6$ in 1 m LiTFSI and 21 m LiTFSI at a scan rate of 2 mV/s. In the

CV of the 21 m LiTFSI solution, the half wave potential for $[Fe(CN)_6]^{3-}$ reduction is 0.22 V vs. Ag/Ag^+, which is more positive compared to that from 1 m LiTFSI (0.13 V). This shift in reduction potential with different LiTFSI concentrations is consistent with the CVs using Au disk electrode (Figure 2.1). The steady-state current density for $[Fe(CN)_6]^{3-}$ reduction is about 5 times smaller in 21 m LiTFSI compared with 1 m LiTFSI, which suggests a smaller diffusion coefficient, D_0, in the concentrated system.[24,25] More interestingly, the CV from 21 m LiTFSI exhibits an oxidation peak at 0.23 V upon the reverse positive potential sweep, which indicates the oxidation of reduced ferrocyanide $[Fe(CN)_6]^{4-}$ at this potential. In contrast, no such oxidation peak is observed in the CV of 1 m LiTSFI, which suggests that the reduced ferrocyanide $[Fe(CN)_6]^{4-}$ is not oxidized in the dilute system at the same potential. Previous studies on steady-state diffusion electrochemical processes, using UME or rotating disk electrode (RDE), have attributed the early oxidation/reduction peak in reverse potential sweep CVs to the presence of surface adsorbed/confined redox species.[45,46,47] The oxidation peak at 0.23 V in the CV in the UME study, together with the small 40 mV peak separation for $[Fe(CN)_6]^{3-}$ redox in the CVs with the Au disk electrode (Figure 2.1b), suggests that reduced $[Fe(CN)_6]^{4-}$ is adsorbed/confined on the electrode surface in 21 m LiTFSI and oxidizes at a lower potential during the reverse positive potential sweep. This adsorption/confinement is not present in the dilute 1 m LiTFSI.

The adsorption/confinement of reduced $[Fe(CN)_6]^{4-}$ on the electrode surface is characteristic of the concentrated 21 m LiTFSI, and thus would be induced by features specific to the electrode-electrolyte interface between the electrode surface and 21 m LiTFSI, which will be further discussed in AFM studies.

Figure 2.4b and 2.4c shows simulated and experimental CVs from 5 mM $K_3Fe(CN)_6$ in 1 m LiTFSI and 21 m LiTFSI. D_0 and electrochemical rate constant k^0 were derived from the

simulations. The oxidation peak of $[Fe(CN)_6]^{4-}$ in 21 m LiTFSI is not considered in the simulation. For 1 m LiTFSI, the best fit to the data from the simulation yields $D_0 = 3.4 \times 10^{-6}$ cm^2/s and $k^0 = 0.006$ cm/s, consistent with previous studies.[48,49] For 21 m LiTFSI, the simulation yields $D_0 = 7.4 \times 10^{-7}$ cm^2/s and $k^0 = 0.002$ cm/s. The decrease in D_0 is attributed to the high viscosity of 21 m LiTFSI.[50] On the other hand, the decrease in k^0 could be due to differences in the $[Fe(CN)_6]^{3-}$ solvation structure, which has been reported to affect charge transfer kinetics previously.[51]

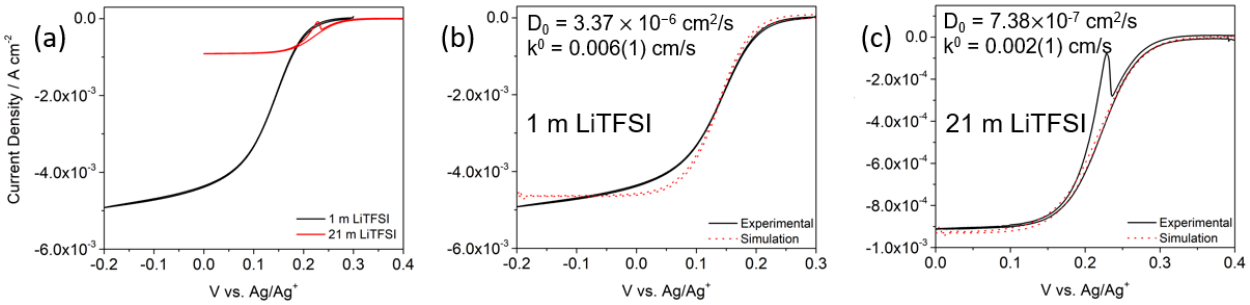

Figure 2.4. (a) Experimental CVs of 5 mM $K_3Fe(CN)_6$ in 1 m LiTFSI, and 21 m LiTFSI at 2 mV/s using a Pt UME (d = 25 μm), and experimental and simulated CVs of 5 mM $K_3Fe(CN)_6$ in (b) 1 m LiTFSI, and (c) 21 m LiTFSI.

2.3.2 Raman Spectroscopy

Raman spectroscopy was carried out to understand the solvation of $[Fe(CN)_6]^{3-}$ in 1 m LiTFSI and 21 m LiTFSI. Figure 2.5 shows the Raman spectra obtained for 100 mM $K_3Fe(CN)_6$ in H_2O, 1 m LiTFSI, and 21 m LiTFSI, respectively. In the spectra of H_2O and 1 m LiTFSI, a peak at 2125 cm^{-1} (Peak A) is observed, which is assigned to the CN stretching ν(CN) of cyanide in H_2O-solvated $[Fe(CN)_6]^{3-}$.[52] For 21 m LiTFSI, the ν(CN) peak appears asymmetric in shape, and shifts to higher wavenumber. Peak fitting yields two Gaussian peaks at 2125 cm^{-1} (Peak A) and 2144 cm^{-1} (Peak B). The peak at 2125 cm^{-1} (Peak A) corresponds to H_2O-solvated

$[Fe(CN)_6]^{3-}$, as observed in H_2O and 1 m LiTFSI. The peak at 2144 cm^{-1} (Peak B) is located at higher wavenumber, which suggests different $[Fe(CN)_6]^{3-}$ solvation. Previous Raman studies reported a positive shift in wavenumber for ν(CN) in $[Fe(CN)_6]^{3-}$ with addition of LiCl to the solution.[53] Given the high concentration of solvated Li^+ $[Li(H_2O)_x]^+$ in 21 m LiTFSI, the shift to 2144 cm^{-1} for CN stretch could be due to the interaction of cyanide ligand in $[Fe(CN)_6]^{3-}$ with $[Li(H_2O)_x]^+$.[9] This difference in solvation structure is likely responsible for change in electrochemical rate constant k^0 (Figure 2.4).[51,54] In addition, previous surface enhanced Raman spectroscopy (SERS) studies have reported on $[Fe(CN)_6]^{3-}$ reduction at a markedly positive potential with the addition of LiCl, which suggests that the interaction with $[Li(H_2O)_x]^+$ could lead to the reduction of $[Fe(CN)_6]^{3-}$ at a more positive potential, as observed in our electrochemical studies (Figure 2.1 and 2.4).

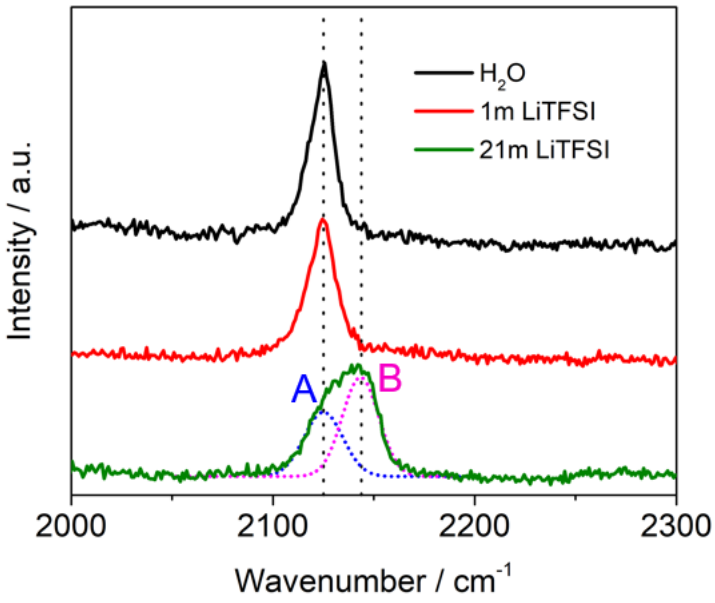

Figure 2.5. Raman spectra of 100 mM $K_3Fe(CN)_6$ solutions in H_2O, 1 m LiTFSI, and 21 m LiTFSI.

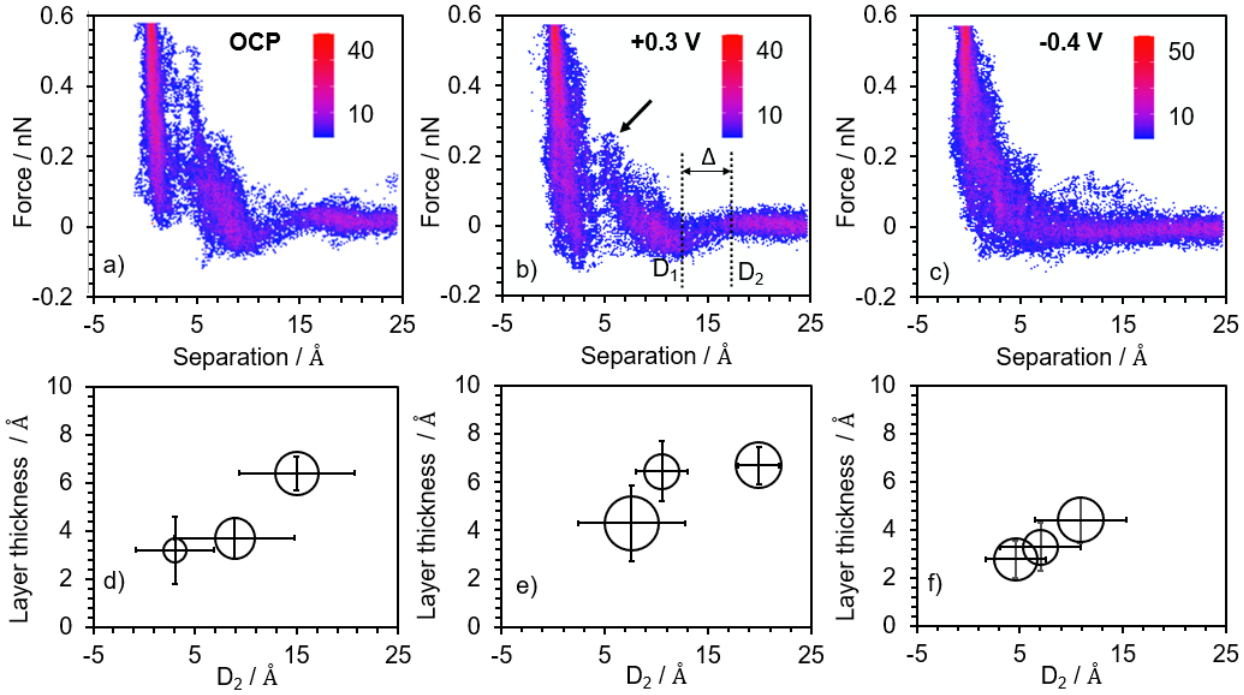

Figure 2.6. (a-c) Heatmaps of superposed force-separation curves measured by AFM in 21 m LiTFSI solution and (d-f) bubble diagrams with the layer thickness (Δ) as a function of the onset separation (D_2) at (a;d) OCP, (b;e) +0.3 V vs. Ag/Ag^+, and (c;f) -0.4 vs. Ag/Ag^+, respectively.

2.3.3 AFM Force Measurements

The short-range interfacial structure in 21 m LiTFSI was measured on a Au (111) textured surface under applied potential to compare to the electrochemical studies described earlier. Figure 2.6a-2.6c show heatmaps obtained by combining 64 separate force-distance curves at each potential. The measured force-distance curves reveal discontinuities in the profile (a typical discontinuity marked with an arrow in Figure 2.6b) as layers either of ions and/or water molecules are displaced with the sharp tip, and therefore, the steps reflect the arrangement of ions and water in layers at the WiSE/electrode interface.[55] A higher force typically suggests a stronger adsorption of the molecules or ions either to the surface or to the underlying layers. The

solvation structure vanishes beyond ~2-3 layers at all conditions. Good reproducibility of the curves was achieved at OCP (measured to be -0.16 V) and at +0.3 V, as evidenced by the high count density on the heatmap. Although steps were clearly resolved on individual curves (Figure 2.7), the presence of a step was less evident when the force curves were superposed in a heatmap. The layered structure of the double layer in 21 m LiTFSI likely leads to a thinner double layer and a higher capacitance (as observed in Figure 2.3), as reported in a previous study on ionic liquids.[56]

Figure 2.6d-2.6f show bubble diagrams plotting the layer thickness as a function of step onset distance. The layer thickness (Δ) is defined as the difference of the film thickness from the onset of the step (D_2) to the end of the step (D_1), i.e. $\Delta=D_2-D_1$, with $D_2>D_1$. Based on both the force required to push through the layer, as well as the position of the onset, three groups of layers were identified at each potential, which are shown in Figure 2.6d-2.6f. The size of the bubble is proportional to the frequency (or probability) this layer is found on the 64 force curves measured. We note that factors influencing the layer thickness include: the composition of the layer, the degree of disorder, the compressibility of the molecules and hydrated ions (at pressures as high as 0.5 GPa applied with the tip), and the possible pressure-induced dehydration of ions.[57,58] Indeed, recent MD simulations for ionic liquids suggest compressibility of ions at high pressures can result in substantially reduced layer thickness. Thus, the layer thickness may be smaller than the actual molecular size.

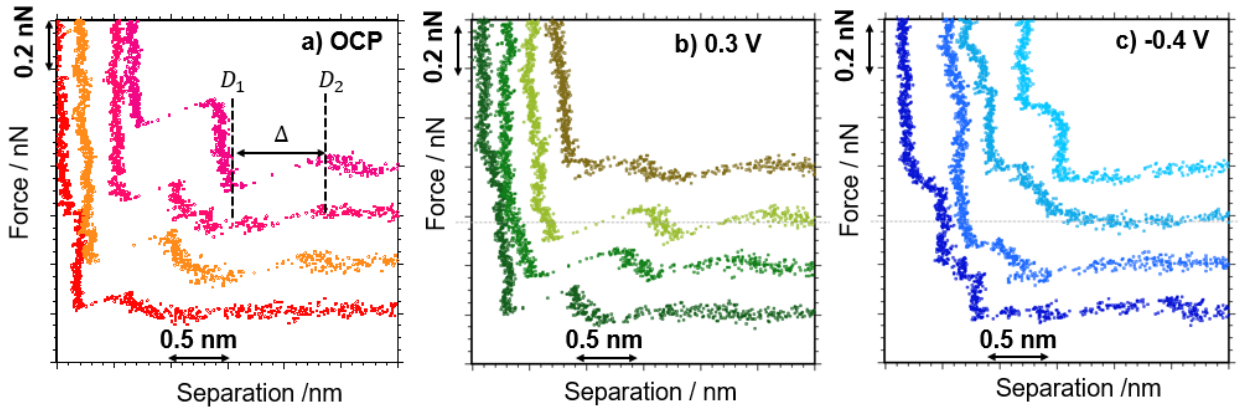

Figure 2.7. Representative force-separation curves measured by AFM in 21 m LiTFSI solution (a) OCP, (b) +0.3 V vs. Ag/Ag^+, and (c) -0.4 vs. Ag/Ag^+, respectively.

At OCP, the step beginning at D_2=15 Å is resolved in most of the curves. The thickness of this layer (Δ~6.7 Å) is significantly larger than the thickness of layers observed at closer separations (3.2 and 3.7 Å, respectively). The magnitudes of Δ values at +0.3 V (Δ= 4.3, 6.4 and 6.7 Å) are larger than that seen at OCP, while the thickness values at -0.4 V are smaller (Δ< 5 Å) than at OCP. At -0.4 V, the three resolved layers do not occur at distinct tip-surface separations, so the bubbles appear superposed along the D_2 axis. Nevertheless, the steps occur at distinct forces, which is illustrated in Figure 2.8.

Figure 2.8 is a bubble diagram of the force vs. layer thickness seen at the three potentials examined here. Figure 2.8 also presents the effective size of $[TFSI]^-$ and hydrated Li^+, the latter based on recent MD simulations of 21m LiTFSI in the bulk WiSE.[9] The Figure shows that the species interrogated by AFM change as a function of potential. At -0.4 V, steps are observed exhibiting a thickness Δ = 4.3 Å and then with progressively higher force Δ becomes 3.3 Å and 2.8 Å. The ca. 3 Å features at this layer is associated with hydrated Li^+ at the interface due to the negative applied potential and the relatively small layer thickness. The reduced layer thickness

relative to the effective size reported from MD simulations is likely a consequence of the dehydration of the Li^+ when it adsorbs to the surface. For example, Fenter and coworkers examined LiCl solutions and found a prominent Li^+ layer at 2.2-2.4 Å from a mica surface, followed by a less prominent layer at 5 Å from the surface, associated with partially dehydrated and highly hydrated Li^+, respectively.[58] At -0.4 V, this comparison thus suggests $[Li(H_2O)_x]^+$ populates the layers closer to the surface. The high force (0.2 and 0.75 nN) of the two groups of layers with Δ~3.3 Å and Δ~ 2.8 Å, respectively, indicates the presence of strong Coulombic interactions. The small thickness of these layers compared to the calculated size of the $[Li(H_2O)_4]^+$ (ca. 5.4 Å) is, however, intriguing. It is possible that the layer at ~0.2 nN is associated with the partial dehydration of the adsorbed $[Li(H_2O)_x]^+$, and the surface-adsorbed Li^+ is resolved at a much higher force (0.75 nN); a dehydration-associated step has been reported for dilute electrolytes in SFA experiments before.[59] This phenomenon would explain the less well-defined heat map, as shown in Figure 2.6c. Another source of the smaller dimension could be compression by the tip. For example, a distortion of the solvation shell induced by the AFM tip pressure and the adsorption to the electrode surface has been reported for Li^+ ions chelated to oligoether ligands with 3 to 4 repeating units.[60,61]

An additional feature at 4.3 Å and relatively low force is found at -0.4 V. There are several possible origins of this feature. First, we note the 4.3 Å layer thickness is close to that predicted for hydrated Li^+. The existence of a solvation layer with Δ~ 4.3 Å might indicate the presence of a second solvation layer rich in $[Li(H_2O)_x]^+$ to further counterbalance the surface potential. The two solvation layers rich in hydrated Li^+ may then reflect the so-called crowding of multiple layers of counter-ions in highly concentrated electrolytes.[62] On the other hand, previous works on $[TFSI]^-$ containing ionic liquids report that layers of ca. 4.4 Å represent layers

rich in $[TFSI]^-$, very close to the 4.3 Å spacing measured here, and slightly smaller than that calculated based on the packing dimension (4.7 Å) and the van der Waals diameter (5.3 Å).[61,63,64] We note the 4.3 Å spacing is also seen at +0.3 V, where the interface is expected to be $[TFSI]^-$-rich (vide infra).

At +0.3 V, a different set of layer thickness (4.3 Å and 6.7 Å) is observed. At +0.3 V, $[Li(H_2O)_x]^+$ is likely repelled from the Au electrode, and replaced by solvation layers rich in $[TFSI]^-$ associated with the surface. The layer thickness Δ = 4.3 Å suggests that it is associated with $[TFSI]^-$, based on the discussion above. However, we cannot completely rule out the occasional presence of the cation complex, since layers of around 3 Å thickness are sometimes detected, as inferred from the large error bars on the Δ = 4.3 Å layer.

Layers of thickness 6.4 Å and 6.7 Å are measured at +0.3V but not at -0.4 V. This size is too large to be associated with a single cation or anion. Thus, these larger solvation layers likely correspond to $[Li(H_2O)_x]^+([TFSI]^-)_y$ clusters. Layers composed of ion pairs have been widely reported in ionic liquids and solutions of metal salts in ionic liquids.[21,65,66,67,68] The presence of ion pairs suggests the applied potential is greatly screened by the surface-adsorbed layers. The larger thickness could reflect a weaker electrostatic attraction to the Au surface. Overall, solvation layers resolved farther from the surface will have a higher number of co-ions and will be more loosely packed because they are less strongly bound to the surface compared to the more strongly adsorbed surface layers.

Ion clusters $[Li(H_2O)_x]^+([TFSI]^-)_y$ are not detected at -0.4 V. The weakened cation-anion interaction close to the surface at negative potential might be associated with enrichment of H_2O at the interface. H_2O, in the solvation sheath of Li^+, disrupts the packing of the species near the surface, and may result in the somewhat less resolved heat map shown in Figure 2.6c. In

contrast, $[TFSI]^-$ forms a well-ordered layer near the positively charged surface. Due to the reduced abundance of water at positive potentials, significant cation-anion pairing happens near the surface, and more commensurate packing is achieved. The well-ordered structure on the cathode together with a randomized interfacial structure on the anode has been previously visualized by molecular dynamics.[13]

OCP is typically measured to be ca. -0.1 to -0.2 V. The layer thickness measured reflect an intermediate situation between the positive and negative potentials discussed above, with both $[Li(H_2O)_x]^+$ and $[Li(H_2O)_x]^+([TFSI]^-)_y$ near the surface.

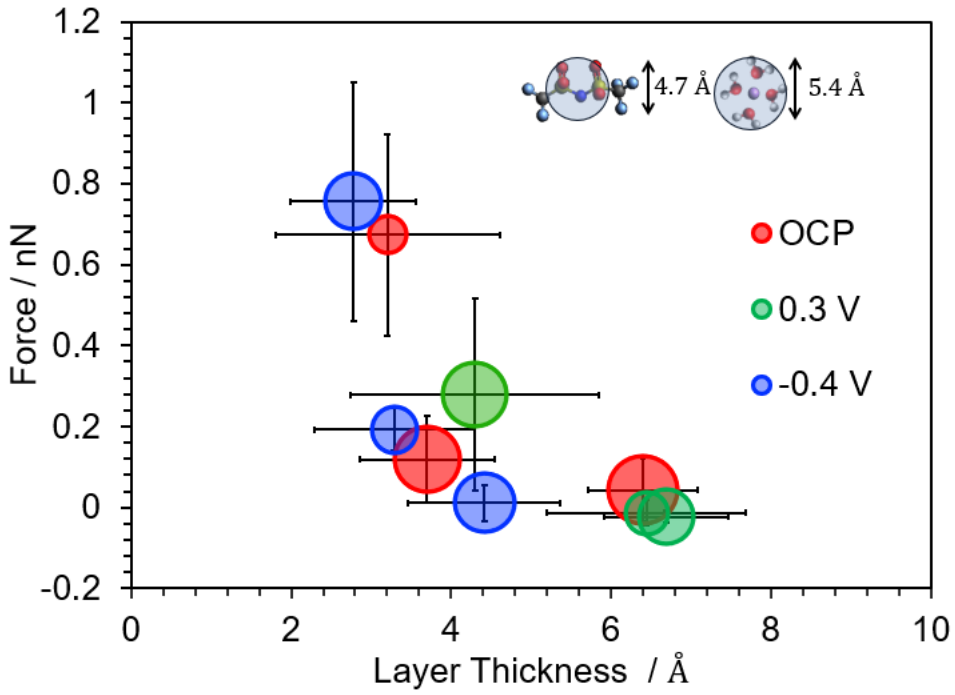

Figure 2.8. Bubble diagram of force vs. layer thickness for 21m LiTFSI solution on gold at OCP, +0.3 V and -0.4V. The inset shows the dimensions of the $[TFSI]^-$ anion and $Li(H_2O)_4$, for comparison.

2.3.4 Surface Vibrational Spectroscopy

To understand the change in chemical speciation in the double layer with potential, we carried out attenuated total reflectance surface enhanced infrared absorption spectroscopy (ATR-SEIRAS). Figure 2.9a shows the potential-dependent ATR-SEIRAS spectra of 21 m LiTFSI obtained from an Au-film deposited on μ-groove Si wafer vs. Ag/Ag^+. As the potential decreases from 0.4 V to -0.5 V, two peaks with negative absorbance at 1244 cm^{-1} and 1359 cm^{-1} are observed, assigned to the CF_3 symmetric stretching $\nu_s(CF_3)$ and SO_2 asymmetric stretching $\nu_a(SO_2)$ from $[TFSI]^-$.[9,50] The negative absorbance suggests that $[TFSI]^-$ decreases in the double layer on the Au surface at more negative potentials. This result is consistent with the previous SEIRAS study.[16] In contrast, a broad band ranging from 3000 - 3600 cm^{-1} exhibits an increasing positive absorbance as the potential decreases. This band is assigned to H_2O stretching $\nu(H_2O)$, and its increase suggests an increase in H_2O content in the double layer on the Au surface at negative potentials.[69] The absorbance peak at 1590 cm^{-1} is assigned to H_2O bending $\delta(H_2O)$.[70] The 1590 cm^{-1} peak position is considered low for $\delta(H_2O)$, and is assigned to H_2O molecules with little H-bonding, consistent with the presence of solvated Li^+ $[Li(H_2O)_x]^+$ in this system.[70,71] The $\delta(H_2O)$ absorbance peak intensity also increases as the potential decreases, which is also consistent with increased H_2O in the double layer at negative potentials.

Figure 2.9b shows plots of normalized absorbance of $\nu_s(CF_3)$, $\nu_a(SO_2)$, and $\nu(H_2O)$ as a function of potential. As the potential decreases, $\nu_s(CF_3)$ and $\nu_a(SO_2)$ decrease in intensity while $\nu(H_2O)$ increases in intensity, indicating a switch from a $[TFSI]^-$-rich DL at positive potentials to a H_2O-rich DL at negative potentials.

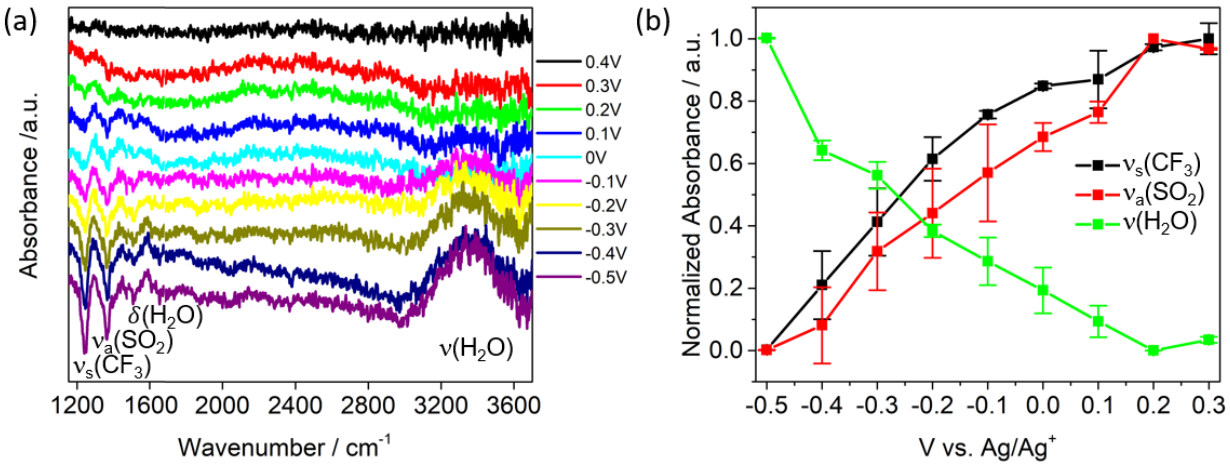

Figure 2.9. (a) ATR-SEIRAS spectra of 21 m LiTFSI at various potential vs. Ag/Ag^+. (b) Normalized absorbance of $\nu_s(CF_3)$, $\nu_a(SO_2)$, and $\nu(H_2O)$ as a function of potential vs. Ag/Ag^+. The reference spectrum was collected at 0.4 V vs Ag/Ag^+.

We also carried out potential dependent surface enhanced Raman spectroscopy (SERS) in the $\delta(H_2O)$ region obtained from 21 m LiTFSI on a Au disk electrode (Figure 2.10). Consistent with the SEIRAS study, the peak intensity of $\delta(H_2O)$ also increases as potential decreases, which suggests increased $[Li(H_2O)_x]^+$ content in the double layer at negative potential.

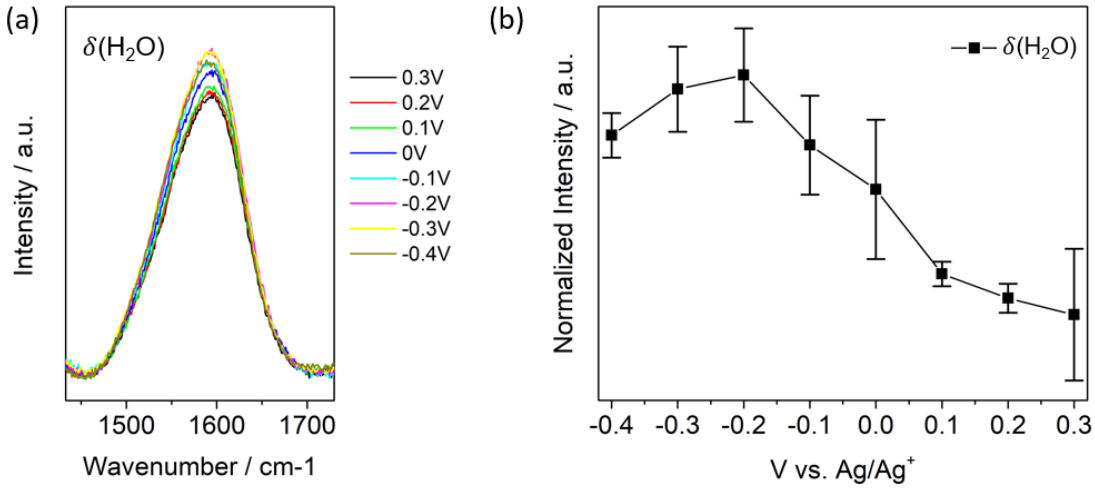

Figure 2.10 (cont.)

Figure 2.10. (a) SERS spectra of 21 m LiTFSI at various potential vs. Ag/Ag^+. (b) Normalized SERS intensity of $\delta(H_2O)$ as a function of potential vs. Ag/Ag^+.

The SEIRAS results support the potential-dependent AFM study. At positive potential, $[TFSI]^-$ dominates the double layer, and its larger size contributes to larger layer thickness in the AFM force curves. At negative potential, H_2O replaces $[TFSI]^-$, and smaller layers are seen in AFM. The H_2O molecules are likely coordinated by Li^+, and $[Li(H_2O)_x]^+$ would compose the double layer, as suggested by the low energy of the $\delta(H_2O)$ peak at 1590 cm^{-1}. The schematic diagram of the potential-dependent double layer of WiSE is shown in Figure 2.11.

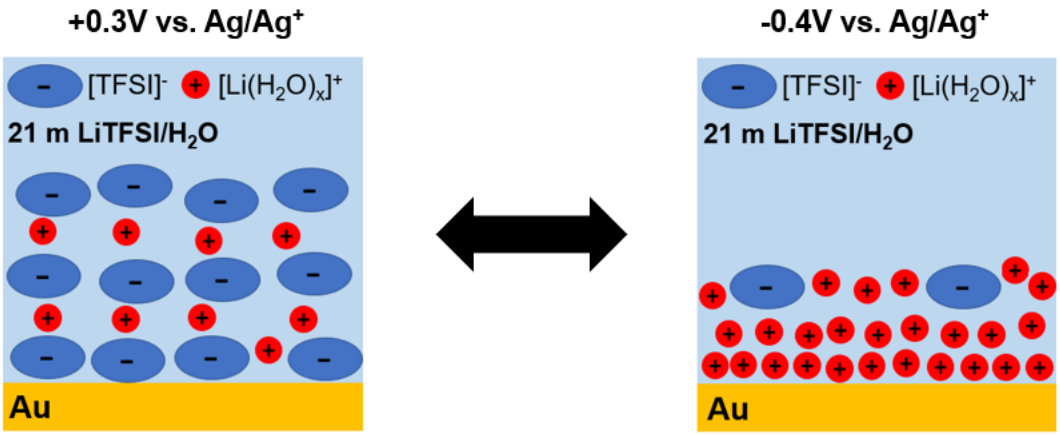

Figure 2.11. The schematic diagram of the potential-dependent double layer of WiSE at +0.3V and -0.4V vs. Ag/Ag^+. The red circle and blue oval denote $[Li(H_2O)_x]^+$ and $[TFSI]^-$ respectively.

The surface-confinement effect observed for $[Fe(CN)_6]^{3-}$ in 21 m LiTFSI is likely caused by the distinct interfacial structures at the $[Fe(CN)_6]^{3-/4-}$ redox potential (> 0V vs. Ag/Ag^+). The positive potential attendant the $[Fe(CN)_6]^{3-/4-}$ redox couple would produce a $[TFSI]^-$-rich, layered, double layer structure. The layered structure as well as the increased hydrophobicity from enhanced $[TFSI]^-$ would inhibit the diffusion of the hydrophilic $[Fe(CN)_6]^{4-}$ to the bulk

leaving $[Fe(CN)_6]^{4-}$ confined near the electrode surface. A test molecule with a more negative redox potential would likely exhibit opposite behavior and this is work in progress. The effect of LiTFSI concentration on the layered structure of the double layer is also under investigation.

2.4 Conclusions

A layered double layer structure is observed in the WiSE system on a (111) textured Au surface. The layered structure exhibits potential dependence, associated with the presence of different species, as inferred from spectroscopy and AFM. At negative potentials, $[Li(H_2O)_x]^+$ is enhanced at the interface. At positive potentials, $[TFSI]^-$ and $[Li(H_2O)_x]^+([TFSI]^-)_y$ clusters are dominant. The layered structure enforces a confinement effect on ferricyanide redox couple, due to its interaction with the layered interfacial structure. Our study brings new insight to understanding the double layer of WiSE and highlights an opportunity to exploit its interfacial structure properties beyond battery applications.

2.5 References

1. Zhao, Q.; Stalin, S.; Zhao, C.-Z.; Archer, L. A., Designing Solid-State Electrolytes for Safe, Energy-Dense Batteries. *Nat. Rev. Mater.* **2020,** *5*, 229-252.

2. Xu, K., Electrolytes and Interphases in Li-Ion Batteries and Beyond. *Chem. Rev.* **2014,** *114*, 11503-11618.

3. Li, M.; Wang, C.; Chen, Z.; Xu, K.; Lu, J., New Concepts in Electrolytes. *Chem. Rev.* **2020,** *120*, 6783-6819.

4. Yamada, Y.; Wang, J.; Ko, S.; Watanabe, E.; Yamada, A., Advances and Issues in Developing Salt-Concentrated Battery Electrolytes. *Nat. Energy* **2019,** *4*, 269-280.

5. Suo, L.; Borodin, O.; Gao, T.; Olguin, M.; Ho, J.; Fan, X.; Luo, C.; Wang, C.; Xu, K., "Water-in-Salt" Electrolyte Enables High-Voltage Aqueous Lithium-Ion Chemistries. *Science* **2015,** *350*, 938-943.

6. Chen, L.; Zhang, J.; Li, Q.; Vatamanu, J.; Ji, X.; Pollard, T. P.; Cui, C.; Hou, S.; Chen, J.; Yang, C.; Ma, L.; Ding, M. S.; Garaga, M.; Greenbaum, S.; Lee, H.-S.; Borodin, O.; Xu, K.; Wang, C., A 63 m Superconcentrated Aqueous Electrolyte for High-Energy Li-Ion Batteries. *ACS Energy Lett.* **2020,** *5*, 968-974.

7. Yamada, Y.; Furukawa, K.; Sodeyama, K.; Kikuchi, K.; Yaegashi, M.; Tateyama, Y.; Yamada, A., Unusual Stability of Acetonitrile-Based Superconcentrated Electrolytes for Fast-Charging Lithium-Ion Batteries. *J. Am. Chem. Soc.* **2014,** *136*, 5039-5046.

8. Wang, F.; Borodin, O.; Ding, M. S.; Gobet, M.; Vatamanu, J.; Fan, X.; Gao, T.; Eidson, N.; Liang, Y.; Sun, W.; Greenbaum, S.; Xu, K.; Wang, C., Hybrid Aqueous/Non-aqueous Electrolyte for Safe and High-Energy Li-Ion Batteries. *Joule* **2018,** *2*, 927-937.

9. Borodin, O.; Suo, L.; Gobet, M.; Ren, X.; Wang, F.; Faraone, A.; Peng, J.; Olguin, M.; Schroeder, M.; Ding, M. S.; Gobrogge, E.; von Wald Cresce, A.; Munoz, S.; Dura, J. A.; Greenbaum, S.; Wang, C.; Xu, K., Liquid Structure with Nano-Heterogeneity Promotes Cationic Transport in Concentrated Electrolytes. *ACS Nano* **2017,** *11*, 10462-10471.

10. Zheng, J.; Tan, G.; Shan, P.; Liu, T.; Hu, J.; Feng, Y.; Yang, L.; Zhang, M.; Chen, Z.; Lin, Y.; Lu, J.; Neuefeind, J. C.; Ren, Y.; Amine, K.; Wang, L.-W.; Xu, K.; Pan, F., Understanding Thermodynamic and Kinetic Contributions in Expanding the Stability Window of Aqueous Electrolytes. *Chem* **2018,** *4*, 2872-2882.

11. Wang, F.; Borodin, O.; Gao, T.; Fan, X.; Sun, W.; Han, F.; Faraone, A.; Dura, J. A.; Xu, K.; Wang, C., Highly Reversible Zinc Metal Anode for Aqueous Batteries. *Nat. Mater.* **2018,** *17*, 543-549.

12. Vatamanu, J.; Borodin, O., Ramifications of Water-in-Salt Interfacial Structure at Charged Electrodes for Electrolyte Electrochemical Stability. *J. Phys. Chem. Lett.* **2017,** *8*, 4362-4367.

13. McEldrew, M.; Goodwin, Z. A. H.; Kornyshev, A. A.; Bazant, M. Z., Theory of the Double Layer in Water-in-Salt Electrolytes. *J. Phys. Chem. Lett.* **2018,** *9*, 5840-5846.

14. Li, Z.; Jeanmairet, G.; Méndez-Morales, T.; Rotenberg, B.; Salanne, M., Capacitive Performance of Water-in-Salt Electrolytes in Supercapacitors: A Simulation Study. *J. Phys. Chem. C* **2018,** *122*, 23917-23924.

15. Lim, J.; Park, K.; Lee, H.; Kim, J.; Kwak, K.; Cho, M., Nanometric Water Channels in Water-in-Salt Lithium Ion Battery Electrolyte. *J. Am. Chem. Soc.* **2018,** *140*, 15661-15667.

16. Borodin, O.; Ren, X.; Vatamanu, J.; von Wald Cresce, A.; Knap, J.; Xu, K., Modeling Insight into Battery Electrolyte Electrochemical Stability and Interfacial Structure. *Acc. Chem. Res.* **2017,** *50*, 2886-2894.

17. Bard, A. J.; Abruna, H. D.; Chidsey, C. E.; Faulkner, L. R.; Feldberg, S. W.; Itaya, K.; Majda, M.; Melroy, O.; Murray, R. W., The Electrode/Electrolyte Interface - A Status Report. *J. Phys. Chem.* **1993,** *97*, 7147-7173.

18. Wu, C. H.; Weatherup, R. S.; Salmeron, M. B., Probing Electrode/Electrolyte Interfaces in Situ by X-Ray spectroscopies: Old Methods, New Tricks. *Phys. Chem. Chem. Phys.* **2015,** *17*, 30229-30239.

19. Han, M.; Espinosa-Marzal, R. M., Strong Stretching of Poly(ethylene glycol) Brushes Mediated by Ionic Liquid Solvation. *J. Phys. Chem. Lett.* **2017,** *8*, 3954-3960.

20. Kim, H.; Han, M.; Bandara, S. R.; Espinosa-Marzal, R. M.; Leal, C., Mixing Oil and Water with Ionic Liquids: Bicontinuous Microemulsions under Confinement. *Soft Matter* **2019,** *15*, 9609-9613.

21. Hayes, R.; Borisenko, N.; Tam, M. K.; Howlett, P. C.; Endres, F.; Atkin, R., Double Layer Structure of Ionic Liquids at the Au(111) Electrode Interface: An Atomic Force Microscopy Investigation. *J. Phys. Chem. C* **2011,** *115*, 6855-6863.

22. Endres, F.; Borisenko, N.; El Abedin, S. Z.; Hayes, R.; Atkin, R., The Interface Ionic Liquid(s)/Electrode(s): In Situ STM and AFM Measurements. *Faraday Discuss.* **2012,** *154*, 221-233.

23. Jurado, L. A.; Espinosa-Marzal, R. M., Insight into the Electrical Double Layer of an Ionic Liquid on Graphene. *Sci. Rep.* **2017,** *7*, 4225.

24. Ta, K.; See, K. A.; Gewirth, A. A., Elucidating Zn and Mg Electrodeposition Mechanisms in Nonaqueous Electrolytes for Next-Generation Metal Batteries. *J. Phys. Chem. C* **2018,** *122*, 13790-13796.

25. Ta, K.; Zhang, R.; Shin, M.; Rooney, R. T.; Neumann, E. K.; Gewirth, A. A., Understanding Ca Electrodeposition and Speciation Processes in Nonaqueous Electrolytes for Next-Generation Ca-Ion Batteries. *ACS Appl. Mater. Interfaces* **2019,** *11*, 21536-21542.

26. Boyle, D. T.; Kong, X.; Pei, A.; Rudnicki, P. E.; Shi, F.; Huang, W.; Bao, Z.; Qin, J.; Cui, Y., Transient Voltammetry with Ultramicroelectrodes Reveals the Electron Transfer Kinetics of Lithium Metal Anodes. *ACS Energy Lett.* **2020,** *5*, 701-709.

27. Schmitt, K. G.; Gewirth, A. A., In Situ Surface-Enhanced Raman Spectroscopy of the Electrochemical Reduction of Carbon Dioxide on Silver with 3,5-Diamino-1,2,4-Triazole. *J. Phys. Chem. C* **2014,** *118*, 17567-17576.

28. Li, X.; Gewirth, A. A., Peroxide Electroreduction on Bi-Modified Au Surfaces: Vibrational Spectroscopy and Density Functional Calculations. *J. Am. Chem. Soc.* **2003,** *125*, 7086-7099.

29. Ataka, K.-i.; Yotsuyanagi, T.; Osawa, M., Potential-Dependent Reorientation of Water Molecules at an Electrode/Electrolyte Interface Studied by Surface-Enhanced Infrared Absorption Spectroscopy. *J. Phys. Chem.* **1996,** *100*, 10664-10672.

30. Morhart, T. A.; Unni, B.; Lardner, M. J.; Burgess, I. J., Electrochemical ATR-SEIRAS Using Low-Cost, Micromachined Si Wafers. *Anal. Chem.* **2017,** *89*, 11818-11824.

31. Ataka, K.-i.; Osawa, M., In Situ Infrared Study of Water−Sulfate Coadsorption on Gold(111) in Sulfuric Acid Solutions. *Langmuir* **1998,** *14*, 951-959.

32. Hutter, J. L.; Bechhoefer, J., Calibration of Atomic-Force Microscope Tips. *Rev. Sci. Instrum.* **1993,** *64*, 1868-1873.

33. Elgrishi, N.; Rountree, K. J.; McCarthy, B. D.; Rountree, E. S.; Eisenhart, T. T.; Dempsey, J. L., A Practical Beginner's Guide to Cyclic Voltammetry. *J. Chem. Educ.* **2018,** *95*, 197-206.

34. Bueno, P. R.; Fabregat-Santiago, F.; Davis, J. J., Elucidating Capacitance and Resistance Terms in Confined Electroactive Molecular Layers. *Anal. Chem.* **2013,** *85*, 411-417.

35. Amatucci, G. G.; Badway, F.; DuPasquier, A., Novel Asymmetric Hybrid Cells and the Use of Pseudo-Reference Electrodes in Three Electrode Cell Characterization. In *The*

Electrochemical Society Proceedings Series, S., M. G.; W., H. D., Eds. Pennington, NJ, 2000; Vol. 94-24, pp 344-352.

36. Zhao, Y.; Yu, Z.; Robertson, L. A.; Zhang, J.; Shi, Z.; Bheemireddy, S. R.; Shkrob, I. A.; Y, Z.; Li, T.; Zhang, Z.; Cheng, L.; Zhang, L., Unexpected Electrochemical Behavior of An Anolyte Redoxmer in Flow Battery Electrolytes: Solvating Cations Help to Fight Against the Thermodynamic-Kinetic Dilemma. *J. Mater. Chem. A* **2020**, DOI: 10.1039/d0ta02214d.

37. Eftekhari, A., Metrics for Fast Supercapacitors as Energy Storage Devices. *ACS Sustainable Chem. Eng.* **2019,** *7*, 3688-3691.

38. Zhang, R.; Pan, C.; Nuzzo, R. G.; Gewirth, A. A., CoS_2 as a Sulfur Redox-Active Cathode Material for High-Capacity Nonaqueous Zn Batteries. *J. Phys. Chem. C* **2019,** *123*, 8740-8745.

39. Vatamanu, J.; Borodin, O.; Olguin, M.; Yushin, G.; Bedrov, D., Charge Storage at the Nanoscale: Understanding the Trends from the Molecular Scale Perspective. *J. Mater. Chem. A* **2017,** *5*, 21049-21076.

40. Raberg, J. H.; Vatamanu, J.; Harris, S. J.; van Oversteeg, C. H. M.; Ramos, A.; Borodin, O.; Cuk, T., Probing Electric Double-Layer Composition via in Situ Vibrational Spectroscopy and Molecular Simulations. *J. Phys. Chem. Lett.* **2019,** *10*, 3381-3389.

41. Aoki, K. J.; Chen, J.; Tang, P., Double Layer Impedance in Mixtures of Acetonitrile and Water. *Electroanalysis* **2018,** *30*, 1634-1641.

42. Bu, X.; Su, L.; Dou, Q.; Lei, S.; Yan, X., A Low-Cost "Water-in-Salt" Electrolyte for a 2.3 V High-Rate Carbon-Based Supercapacitor. *J. Mater. Chem. A* **2019,** *7*, 7541-7547.

43. Ma, M.; Shi, Z.; Li, Y.; Yang, Y.; Zhang, Y.; Wu, Y.; Zhao, H.; Xie, E., High-Performance 3 V "Water in Salt" Aqueous Asymmetric Supercapacitors Based on VN Nanowire Electrodes. *J. Mater. Chem. A* **2020,** *8*, 4827-4835.

44. Dickinson, K. M.; Hanson, K. E.; Fredlein, R. A., Potentials of Zero Charge and Capacitance Minima of Polycrystalline Gold in Sodium Fluoride Solutions. *Electrochim. Acta* **1992,** *37*, 139-141.

45. Zheng, Q.; Shao, H., Correlation Between Redox Species Adsorption and Electron Transfer Kinetics of Mildly Oxidized Graphene: A Chronocoulometry and SECM Study. *Electrochem. Commun.* **2019,** *103*, 83-87.

46. Salazar-Banda, G. R.; Eguiluz, K. I. B.; Carvalho, A. E. d.; Avaca, L. A., Ultramicroelectrode Array Behavior of Electrochemically Partially Blocked Boron-Doped Diamond Surface. *J Braz. Chem. Soc.* **2013,** *24*, 1206-1211.

47. Szulborska, A.; Baranski, A., Kinetics and Thermodynamics of Thioglycol Adsorption on Mercury Ultramicroelectrodes. *J. Electroanal. Chem.* **1994,** *377*, 269-281.

48. Konopka, S. J.; McDuffie, B., Diffusion Coefficients of Ferri- and Ferrocyanide Ions in Aqueous Media, Using Twin-Electrode Thin-Layer Electrochemistry. *Anal. Chem.* **1970,** *42*, 1741-1746.

49. Pletcher, D.; Tian, Z.-Q.; Williams, D., *Developments in Electrochemistry: Science Inspired by Martin Fleischmann*. John Wiley & Sons: 2014.

50. Yamada, Y.; Yamada, A., Review—Superconcentrated Electrolytes for Lithium Batteries. *J. Electrochem. Soc.* **2015,** *162*, A2406-A2423.

51. Fu, C.; Xu, L.; Aquino, F. W.; v. Cresce, A.; Gobet, M.; Greenbaum, S. G.; Xu, K.; Wong, B. M.; Guo, J., Correlating Li^+-Solvation Structure and its Electrochemical Reaction Kinetics with Sulfur in Subnano Confinement. *J. Phys. Chem. Lett.* **2018,** *9*, 1739-1745.

52. Martín-Yerga, D.; Pérez-Junquera, A.; González-García, M. B.; Perales-Rondon, J. V.; Heras, A.; Colina, A.; Hernández-Santos, D.; Fanjul-Bolado, P., Quantitative Raman Spectroelectrochemistry Using Silver Screen-Printed Electrodes. *Electrochim. Acta* **2018,** *264*, 183-190.

53. Fleischmann, M.; Graves, P. R.; Robinson, J., The Raman Spectroscopy of the Ferricyanide/Ferrocyanide System at Gold, β-Palladium Hydride and Platinum Electrodes. *J. Electroanal. Chem. Interf. Electrochem.* **1985,** *182*, 87-98.

54. Ong, M. T.; Verners, O.; Draeger, E. W.; van Duin, A. C. T.; Lordi, V.; Pask, J. E., Lithium Ion Solvation and Diffusion in Bulk Organic Electrolytes from First-Principles and Classical Reactive Molecular Dynamics. *J. Phys. Chem. B* **2015,** *119*, 1535-1545.

55. Lin, W.-C.; Marcellan, A.; Hourdet, D.; Creton, C., Effect of polymer–particle interaction on the fracture toughness of silica filled hydrogels. *Soft Matter* **2011,** *7*, 6578-6582.

56. Mao, X.; Brown, P.; Červinka, C.; Hazell, G.; Li, H.; Ren, Y.; Chen, D.; Atkin, R.; Eastoe, J.; Grillo, I.; Padua, A. A. H.; Costa Gomes, M. F.; Hatton, T. A., Self-Assembled Nanostructures in Ionic Liquids Facilitate Charge Storage at Electrified Interfaces. *Nat. Mater.* **2019,** *18*, 1350-1357.

57. Heuberger, M.; Zach, M., Nanofluidics: Structural Forces, Density Anomalies, and the Pivotal Role of Nanoparticles. *Langmuir* **2003,** *19*, 1943-1947.

58. Lee, S. S.; Fenter, P.; Nagy, K. L.; Sturchio, N. C., Monovalent Ion Adsorption at the Muscovite (001)–Solution Interface: Relationships among Ion Coverage and Speciation, Interfacial Water Structure, and Substrate Relaxation. *Langmuir* **2012,** *28*, 8637-8650.

59. Zachariah, Z.; Espinosa-Marzal, R. M.; Spencer, N. D.; Heuberger, M. P., Stepwise Collapse of Highly Overlapping Electrical Double Layers. *Phys. Chem. Chem. Phys.* **2016,** *18*, 24417-24427.

60. Cook, A.; Ueno, K.; Watanabe, M.; Atkin, R.; Li, H., Effect of Variation in Anion Type and Glyme Length on the Nanostructure of the Solvate Ionic Liquid/Graphite Interface as a Function of Potential. *J. Phys. Chem. C* **2017,** *121*, 15728-15734.

61. McLean, B.; Li, H.; Stefanovic, R.; Wood, R. J.; Webber, G. B.; Ueno, K.; Watanabe, M.; Warr, G. G.; Page, A.; Atkin, R., Nanostructure of [Li(G_4)]TFSI and [Li(G_4)]NO_3 Solvate Ionic Liquids at HOPG and Au(111) Electrode Interfaces as a Function of Potential. *Phys. Chem. Chem. Phys.* **2015,** *17*, 325-333.

62. Bazant, M. Z.; Storey, B. D.; Kornyshev, A. A., Double Layer in Ionic Liquids: Overscreening versus Crowding. *Phys. Rev. Lett.* **2011,** *106*, 046102.

63. Carstens, T.; Gustus, R.; Höfft, O.; Borisenko, N.; Endres, F.; Li, H.; Wood, R. J.; Page, A. J.; Atkin, R., Combined STM, AFM, and DFT Study of the Highly Ordered Pyrolytic Graphite/1-Octyl-3-methyl-imidazolium Bis(trifluoromethylsulfonyl)imide Interface. *J. Phys. Chem. C* **2014,** *118*, 10833-10843.

64. McEwen, A. B., Electrochemical Properties of Imidazolium Salt Electrolytes for Electrochemical Capacitor Applications. *J. Electrochem. Soc.* **1999,** *146*, 1687.

65. Atkin, R.; El Abedin, S. Z.; Hayes, R.; Gasparotto, L. H. S.; Borisenko, N.; Endres, F., AFM and STM Studies on the Surface Interaction of [BMP]TFSA and [EMIm]TFSA Ionic Liquids with Au(111). *J. Phys. Chem. C* **2009,** *113*, 13266-13272.

66. Li, H.; Endres, F.; Atkin, R., Effect of Alkyl Chain Length and Anion Species on the Interfacial Nanostructure of Ionic Liquids at the Au(111)–Ionic Liquid Interface as a Function of Potential. *Phys. Chem. Chem. Phys.* **2013,** *15*, 14624-14633.

67. Carstens, T.; Lahiri, A.; Borisenko, N.; Endres, F., [Py1,4]FSI-NaFSI-Based Ionic Liquid Electrolyte for Sodium Batteries: Na^+ Solvation and Interfacial Nanostructure on Au(111). *J. Phys. Chem. C* **2016,** *120*, 14736-14741.

68. Lahiri, A.; Carstens, T.; Atkin, R.; Borisenko, N.; Endres, F., In Situ Atomic Force Microscopic Studies of the Interfacial Multilayer Nanostructure of LiTFSI–[Py1, 4]TFSI on Au(111): Influence of Li^+ Ion Concentration on the Au(111)/IL Interface. *J. Phys. Chem. C* **2015,** *119*, 16734-16742.

69. Rieth, A. J.; Wright, A. M.; Skorupskii, G.; Mancuso, J. L.; Hendon, C. H.; Dincă, M., Record-Setting Sorbents for Reversible Water Uptake by Systematic Anion Exchanges in Metal–Organic Frameworks. *J. Am. Chem. Soc.* **2019,** *141*, 13858-13866.

70. Petit, T.; Puskar, L.; Dolenko, T.; Choudhury, S.; Ritter, E.; Burikov, S.; Laptinskiy, K.; Brzustowski, Q.; Schade, U.; Yuzawa, H.; Nagasaka, M.; Kosugi, N.; Kurzyp, M.; Venerosy, A.; Girard, H.; Arnault, J.-C.; Osawa, E.; Nunn, N.; Shenderova, O.; Aziz, E. F., Unusual Water Hydrogen Bond Network around Hydrogenated Nanodiamonds. *J. Phys. Chem. C* **2017,** *121*, 5185-5194.

71. Laporta, M.; Pegoraro, M.; Zanderighi, L., Perfluorosulfonated Membrane (Nafion): FT-IR Study of the State of Water with Increasing Humidity. *Phys. Chem. Chem. Phys.* **1999,** *1*, 4619-4628.

Chapter 3: Conversion of Co Nanoparticles to CoS in MOF-Derived Porous Carbon During Cycling Facilitates Na_2S Reactivity in a Na-S Battery

Reproduced with permission from Zhang, R.; Esposito, A. M.; Thornburg, E. S.; Chen X.; Zhang; X.; Philip, M. A.; Magaña, A.; Gewirth, A. A. Conversion of Co Nanoparticles to CoS in Metal–Organic Framework-Derived Porous Carbon during Cycling Facilitates Na_2S Reactivity in a Na–S Battery. *ACS Appl. Mater. Interfaces 2020. 12, 29285−29295. Copyright 2020 ACS Applied Materials & Interfaces.*

3.1 Introduction

The growing market in portable electronic devices and electric vehicles has created a demand for high-energy-density batteries exhibiting performance beyond that available from current Li-ion batteries.[1,2] Sulfur batteries (Li-S, Na-S, etc.) have emerged as potential candidates due to their high theoretical capacity (1672 mAh/g S), low cost, as well as the high natural abundance of S.[3,4] Among the sulfur batteries, room-temperature Na-S batteries are desirable due to the higher natural abundance of Na relative to Li and expected low operation cost.[5] With a high theoretical specific energy of 1274 Wh/kg on a Na and S basis, room-temperature Na-S batteries would be a promising alternative to Li-based energy storage devices.[6]

The development of room-temperature Na-S batteries, however, faces more challenges compared to the Li-S systems. Sodium polysulfides are more soluble than their Li analogous.[7] Polysulfides dissolution leads to drastic capacity fade due to loss of active material and the shuttle effect.[8,9] Na is also more reactive with aprotic solvent molecules and the solid electrolyte interphase (SEI) formed is less stable, leading to poor Coulombic efficiency (C.E.) on the anode

side.[6,10] In addition, Na^+ ions are larger than Li^+ ions.[11] Therefore, reactions at the cathode are more limited by transport and kinetics.[12] Na_2S and Na_2S_2 are also nonconductive, which makes achieving full sulfur reactivity more challenging.[5] Previous studies have reported on the sluggish kinetics of the conversion of Na_2S or short-chain Na polysulfides to long-chain polysulfide and elemental S_8, leading to low reversible capacity and fast capacity fade.[8,13,14]

Various strategies have been utilized to tackle the problems facing Na-S batteries. Concentrated electrolytes can be used to prevent polysulfide dissolution, as widely demonstrated in Li-S systems.[15] The high concentration of Li^+ ions present in the electrolyte disrupts the equilibrium of lithium polysulfide, and thereby inhibits its dissolution, also known as the common ion effect.[16] Concentrated electrolytes also contain fewer free solvent molecules and stabilize the solvent through cation coordination, inhibiting their decomposition at the anode.[17]

A wide group of concentrated Na electrolytes have been reported, using sodium bis(trifluoromethanesulfonyl)imide (NaTFSI), sodium bis(fluorosulfonyl)imide (NaFSI), and sodium trifluoromethanesulfonate (NaOTF) as salts, glymes as solvents, and hydrofluoroether (HFE) as cosolvents.[18,19,20,21] Studies on their application in Na-S batteries, however, are limited.[18] Among the concentrated Na electrolytes, 5.2 M NaFSI/DME system is the most promising, with a Na plating/striping C.E. of > 99%.[21] The addition of bis(2,2,2-trifluoroethyl) ether (BTFE) lowers the viscosity of the electrolyte while maintaining the high C.E. of Na electrodeposition.[22] The application of the NaFSI/DME/BTFE concentrated electrolyte in a Na-S battery would not only prevent sodium polysulfide dissolution, but also promote reversible Na electrodeposition on the anode.

The poor conductivity of sulfur and its reduced products can be mitigated by introducing a conductive porous carbon sulfur host, such as hollow carbon spheres, carbon fibers, and carbon

nanotubes.[6,8,23] Furthermore, the introduction of catalytic species can promote sulfur reactivity, which is widely demonstrated in Li-S systems.[24] These catalysts contain active sites which interact with various lithium sulfides, enabling facile reversible conversion between lithium polysulfides and Li_2S_2 and Li_2S.[24,25] Various transition metals (Pt, Co), transition metal oxides (MnO_2, Ti_4O_7) and sulfides (CoS_2, MoS_2) have all been reported to be electrocatalysts for Li-S batteries.[26,27,28,29,30,31] Among the transition metals, Co attracts wide attention due to the catalytic activity observed in its metallic phase (Co), oxide phase (Co_3O_4) as well as sulfide phases (CoS_2, CoS).[27,30,32,33,34] Therefore, a Co-containing porous carbon host could promise enhanced sulfur reactivity in Na-S batteries.

A Co-containing porous carbon host can be derived from metal-organic-framework (MOF) materials. Previous studies on the oxygen reduction reaction (ORR) have reported MOF-derived N-doped porous carbon host containing both Co nanoparticles and CoN_4 sites as ORR catalysts.[35,36,37] In the ORR literature there is substantial controversy as to active site responsible for the ORR activity, with both Co nanoparticles and CoN_4 implicated.[37,38] One of the interesting features of these MOF-derived materials is that the removal of Co content with acid washing improves ORR activity, and the removed Co species are considered as unstable and non-catalytic.[35,36] Nonetheless, the MOF-derived porous carbon with Co content present could be applied as conductive catalytic sulfur host in Na-S systems, and understanding the role that Co species plays in the sulfur battery is important.

In this work, we used a MOF-derived Co-containing N-doped porous carbon host (CoNC) and NaFSI/DME/BTFE concentrated electrolyte in a Na-S battery. We investigate the effect of Co-content on the sulfur cycling performance by controlling the amount of Co in the carbon host via acid-washing. Significant improvement in sulfur reactivity is observed with

higher Co-content (600 mAh/g for CoNC and 261 mAh/g for acid-washed CoNC at cycle 50 at 80 mAh/g). More importantly, we carried out postmortem characterization (XPS, TEM and Selected Area Electron Diffraction(SAED)) on the Co species present in the sulfur cathode after cycling. CoS forms with cycling replacing the Co nanoparticles and CoN_4 sites initially present in the carbon host. Finally, we confirm the catalytic effect of CoS on the oxidation of Na_2S via Raman spectroscopy. Our study provides guidelines in developing Co-containing porous carbon host for application in high-performance Na-S batteries.

3.2 Experimental

NaFSI (99.7% pure) was purchased from Solvionic, France. 2-(2,2,2-trifluoroethoxy)-1,1,1-trifluoroethane (BTFE, 99% pure) was purchased from Synquest, Alachua, Florida. Sulfur nanopowder (Nano S, 30nm, 99.99%) was purchased from US Research Nanomaterials, Houston, Texas. Other chemicals were purchased from Sigma-Aldrich and Alfa Aesar, and used as received.

3.2.1 Material Synthesis

3.2.1.1 Synthesis of CoNC

CoNC was prepared following a previously published method.[35] The precursor was prepared by dissolving 9 mmol of zinc nitrate hexahydrate, 4 mmol cobalt(II) nitrate hexahydrate, and 1 g of cetyltrimethylammonium bromide (CTAB) in 50 mL of methanol. 39 mmol of 2-methylimidazole was dissolved in a separate flask in 50 mL of methanol. The two flasks were combined and stirred for 5 min at room temperature. Then the flask was stirred at 60 ^{o}C under reflux for 30 min. The resulting solution was washed with methanol and then

centrifuged. Then the solid was washed with ethanol and centrifuged. The resulting solid was dried at 80 ºC overnight and then crushed to form a purple powder. The resulting purple powder was pyrolyzed in a ceramic boat under N_2 gas. Gas flow rates were 1000 cc/min. The temperature was ramped at ~ 30 ºC/min until 900 ºC was reached and held constant for 3 hr. The catalyst was then allowed to cool to room temperature under N_2 gas flow. Acid-washed CoNC was prepared by stirring CoNC in 6 M HCl at 60 ºC overnight. The material was collected by vacuum filtration and dried at 80 ºC for at least 5 h.

3.2.1.2 Synthesis of Co Nanoparticles

Co nanoparticles (Nano Co) were synthesized following a previously reported method.[39] In short, 0.25 mmol of $Co(OAc)_2$ and 0.05 mmol of oleic acid were dissolved in 100mL ethanol. $NaBH_4$ ethanol solution was added dropwise into the $Co(OAc)_2$ solution. The mixture was then centrifuged and the Co nanoparticles were rinsed three times with ethanol, and dried at 60 ºC for 5 hours.

3.2.1.3 Synthesis of CoS

CoS was synthesized using a previously reported method.[40] In brief, 6mmol $CoCl_2$ and 24mmol thiourea were dissolved in 75mL of H_2O and 15mL of ethylene glycol. The solution is transferred into a 100mL Teflon-lined stainless steel autoclave, and then heated at 180ºC for 15 hours. The CoS particles were collected via centrifuge, and washed three times with water and ethanol. The obtained CoS was dried at 50ºC under vacuum for 5 hours.

3.2.2 Cathode Preparation

The CoNC or acid-washed CoNC were mixed with sulfur in a 1:1 mass ratio and heated at 155 ºC for 12 hours to carry out the sulfur melt-diffusion process. The active material (CoNC@S and acid-washed CoNC@S), super P Li Carbon (Timcal), and carboxymethyl cellulose (CMC) were mixed in a 7:2:1 mass ratio in water. The mixture was mixed in a conditioning mixer and a sonicator, cast onto a Cu foil using a doctor blade with a thickness of ~50 μm, and dried in a vacuum oven at 60 ºC overnight. The dried cathode was then punched into a 12.7mm disk, with a typical loading of active material of 1.4-1.5 mg. The corresponding sulfur loading was 0.6-0.7 mg/cm^2. The Nano Co + Nano S and CoS + Nano S cathodes were prepared by mixing the respective Nano Co, CoS and Nano S in a 1:1 mass ratio with grinding in mortar and pestle. The mixed active material or Nano S alone, Ketjenblack EC600JD (Akzo), and poly(vinylidene difluoride) (PVDF) were mixed in a weight ratio of 7:2:1 in N-methyl-2-pyrrolidone (NMP) (to avoid CoS dissolution) and the respective cathode materials were prepared undergoing the same following procedure.

3.2.3 Coin Cell Assembly

Galvanostatic cycling measurements were carried out in 2032 coin-type cells using an MTI 8 Channel Battery Analyzer. The coin cells were assembled in an Ar-filled glovebox, which contained <4ppm of O_2 and <1 ppm of H_2O. Na foil was used as counter/reference electrode. Glass fiber separators were used. Solvate electrolyte was prepared with NaFSI, DME and BTFE.[22] NaFSI was dissolved in DME in a 1:1 molar ratio (~5.2 M), and then diluted with BTFE in a 2:1 volume ratio, corresponding to a molar ratio of NaFSI:DME:BTFE = 1:1:0.8. The result mixture was used as the electrolyte. Typical current density is 80 mA/g, corresponding to 0.1C.

Cyclic Voltammetry (CV) measurements were carried out on a Biologic potentiostat (Model SP-150, France).

3.2.4 Characterization

X-ray photoelectron spectroscopy (XPS) studies were performed using a Kratos Axis ULTRA X-Ray Photoelectron Spectrometer with focused monochromatized Al Kα radiation (1486.8 eV). CasaXPS software was used for peak analysis. To minimize exposure to air and moisture, the cathodes were stored and transferred in Ar. Scanning electron microscopy (SEM) imaging was performed using a JEOL 7000F Analytical SEM. Transmission electron microscopy (TEM) and high resolution (HR)-TEM imaging were performed on JEOL 2010 LaB_6 and Hitachi H-9500 microscopes, with accelerating voltages of 200 kV and 300 kV, respectively. Selected area electron diffraction (SAED) was carried out on single particles on the Hitachi H-9500 TEM at an accelerating voltage of 300 kV, camera length of 0.25 m, and using the smallest SA aperture. All diffraction patterns were calibrated using the polycrystalline Au(111) diffraction ring scattered from sputtered Au TEM calibration standards, which was acquired prior to all SAED analysis. Electrochemical impedance spectroscopy (EIS) was performed on a Biologic potentiostat (Model SP-150, France). The alternating current (AC) perturbation signal was ±10 mV and the frequency ranged from 10 mHz to 1 MHz. The analysis of the spectra was carried out using Zview software (Scribner Associates Inc.). The X-ray diffraction (XRD) measurements were carried out using a Siemens/Bruker D-5000 instrument with a Cu Kα radiation source, which generates X-rays of energy 8 keV (1.5418 Å). XRD pattern analysis was carried out using Jade 9.0 software. Raman spectroscopy study was carried out using a 632.8nm He/Ne laser with an instrument setup described previously.[41] The Na_2S + CoS Raman sample is

prepared by grinding Na_2S and CoS in a 2 : 1 ratio in 0.2 mL DME in mortar and pestle. DME is then evaporated to yield powder mixture.

3.3 Results

3.3.1 Electrochemical Performance of CoNC and Role of Cobalt in Na-S System

Figure 3.1a shows the SEM image of CoNC. The MOF-derived carbon spheres appear spherical with a ~ 500 nm diameter. Consistent with prior reports, the spheres appear to have a narrow size distribution.[35] The narrow size distribution is associated with the confinement effect attendant the addition CTAB as a surfactant which controls the size of the MOF nanocrystal precursor.[35] The BET specific surface area is determined to be 640 cm^2/g. No obvious particles can be observed on the spherical carbon structure. Figure 3.1b shows the XRD pattern of CoNC. Two peaks at 2θ = 44° and 51° correspond to the (111) and (200) planes of Co, and the broad peak at 2θ = 25° is associated with graphitic carbon.[27] The TEM image of CoNC is shown in Figure 3.1c. Dark spots are seen in the image, which are associated with Co nanoparticles in the carbon framework consistent with prior results.[42] Vibrating sample magnetometer (VSM) data shows ferromagnetic properties of CoNC at room temperature, which suggests that the dark spots present in the carbon structure are indeed Co nanoparticles (Figure 3.2).[43] ICP-OES result yields a 9.3$\pm$0.1 wt% Co.

TEM images of the acid-washed CoNC is shown in Figure 3.1d. The image still evinces the presence dark spots, albeit at a reduced density relative to the as-prepared CoNC sample. This observation indicates that a significant amount of Co nanoparticles is removed. Indeed, the measured Co content from ICP-OES is 4.3$\pm$0.2 wt%. The BET specific surface area is determined to be 706 cm^2/g, suggesting a 10% increase of surface area in acid-washed CoNC

compared with CoNC. VSM shows that consistent with CoNC, the acid-washed CoNC is also ferromagnetic (Figure 3.2), which suggests that the Co speciation does not change with acid washing. A decrease in ferromagnetism is observed due to the decrease in Co content. Previous studies have shown minimal change in size and shape of CoNC after acid-washing.[35,36] Our study also shows that other than a decrease in Co content, acid-washing has minimal impact on the spherical shape of the carbon structure or the speciation of Co.

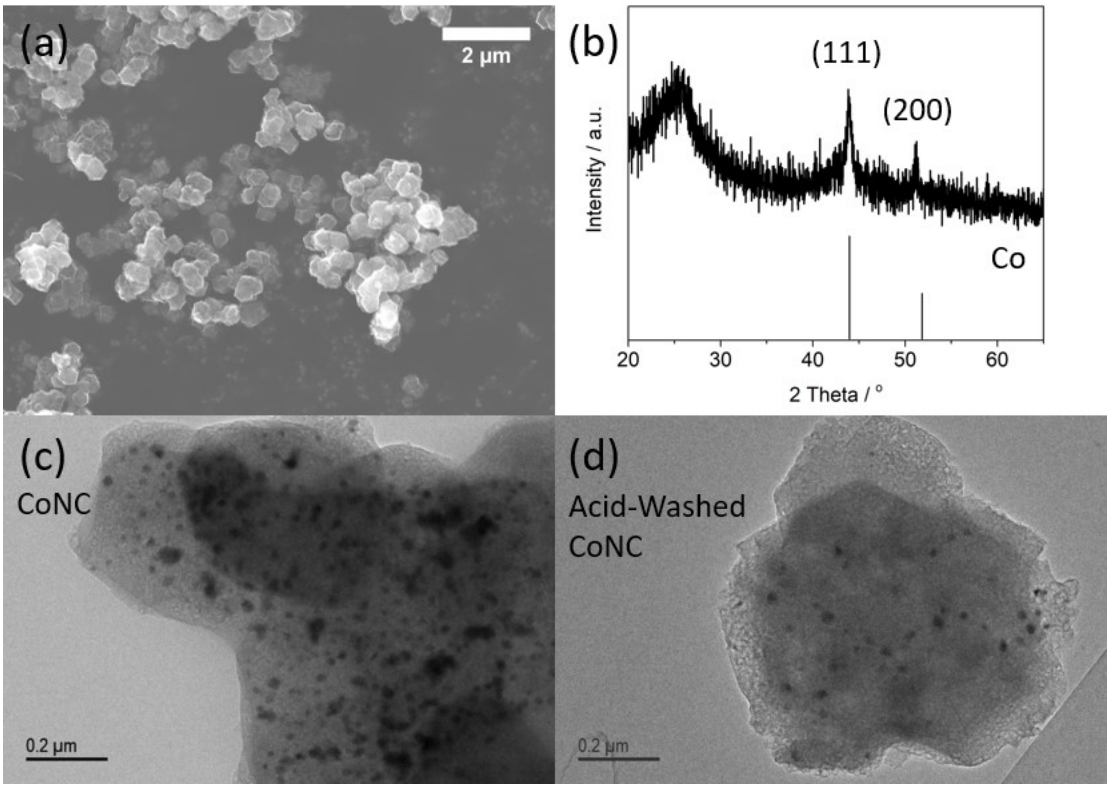

Figure 3.1. (a) SEM image of CoNC. (b) XRD pattern of CoNC. (c) TEM image of CoNC. (c) TEM image of acid-washed CoNC.

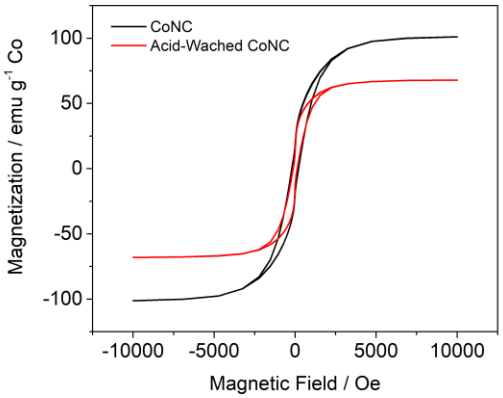

Figure 3.2. Vibrating Sample Magnetometer (VSM) data of CoNC and acid-washed CoNC.

We carried out XPS to investigate the valence states of Co and S prior to battery cycling. Figure 3.3a shows the Co 2p photoemission spectra of the CoNC sample before and after the sulfur melt-diffusion process. Before the S melt-diffusion process, the CoNC Co 2p spectrum contains two main peaks at 780.1 eV ($2p_{3/2}$) and 795.6 eV ($2p_{1/2}$), which can be assigned to cobalt oxide with a mixed Co^{2+}/Co^{3+} valence state, with their corresponding satellite peaks at 786.0 eV and 802.9 eV.[32,44,45] The XPS components at 781.7 eV and 797.9 eV (required for the fit) are assigned to the presence of Co-N bond, which is assigned to CoN_4 sites in previous studies.[35,46] After S melt-diffusion, the two main peaks shift to 781.0 eV and 797.2 eV, along with their satellite peaks at 785.6 eV and 802.4 eV respectively. This change in spectra indicates a change in Co valence state. Deconvolution of Co^{2+} and Co^{3+} $2p_{3/2}$ peaks is challenging due to their small binding energy difference. Alternatively, the position and intensity of the shake-up satellite peaks is a stronger indicator of Co valence state, where CoO exhibits satellite peaks with higher intensity and smaller splitting above the $2p_{3/2}$ binding energy compared to Co_3O_4.[47,48] In the spectrum of CoNC after S melt-diffusion (CoNC@S), the satellite peaks are more intense and lower in binding energy compared to the spectrum before S melt-diffusion, indicating that the Co content takes on more CoO character after S melt-diffusion process, possibly due to interaction

with the sulfur and reduction of the oxide.[14,49] Nonetheless, the Co 2p spectra suggests that the Co nanoparticles in the samples contain surface oxides.

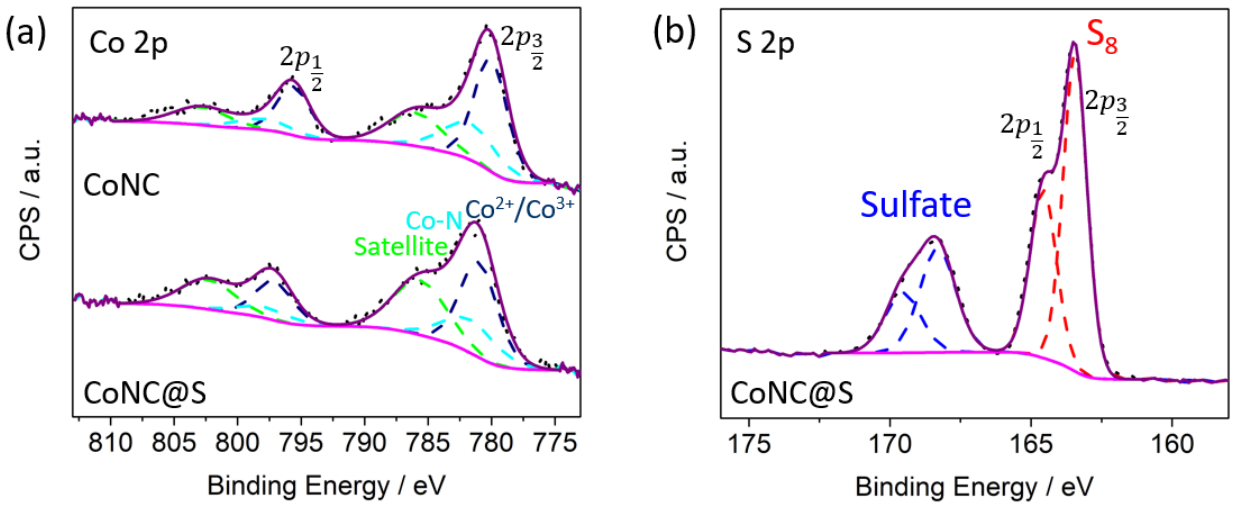

Figure 3.3. XPS spectra for (a) Co 2p and (b) S 2p of CoNC and CoNC@S before cycling. The color dashed lines represent fits of different species to the XPS. Components in Co 2p XPS spectra include Co^{2+}/Co^{3+} (navy), Co-N (light blue) and satellite (green). Components in S 2p XPS spectrum include S_8 (red) and sulfate (blue).

S 2p XPS spectrum of the CoNC@S is shown in Figure 3.3b. Two main peaks at 163.4 eV ($2p_{3/2}$) and 164.6 eV ($2p_{1/2}$) correspond to elemental sulfur S_8.[14,50,51] The peak at 168.3 eV can be assigned to the presence of sulfate species as a result of sulfur oxidation on the surface, which has been observed in the melt-diffusion process.[14,42]

We evaluated the battery cycling performance of CoNC@S and acid-washed CoNC@S with melt-diffused sulfur utilizing a Na metal anode and NaFSI/DME/BTFE concentrated electrolyte (molar ratio 1:1:0.8) in coin cells. The utilization of concentrated electrolytes may mitigate polysulfide dissolution, enhancing cycling performance of sulfur cathodes.[52,53] Figure 3.4a and 3.4b show the galvanostatic cycling data of CoNC@S and acid-washed CoNC@S

cycled between 2.7 V and 1.0 V, under the same current density of 80 mA/g. As shown in Figure 3.4a, CoNC@S exhibits an initial capacity of 1095 mAh/g. At cycle 2, the capacity is 784 mAh/g, retaining 72% of the initial capacity. The decrease in capacity after the first cycle is due to the irreversible conversion of Na_2S, which has been reported previously for Na-S systems.[8,23] From cycle 2 to cycle 50, the capacity retention is 77%, with a capacity of 600 mAh/g and Coulombic efficiency (C.E.) of 99% at cycle 50. At cycle 100 and 150, the capacity is 530 mAh/g and 500 mAh/g respectively, with C.E. > 99%. In contrast, acid-washed CoNC@S exhibits 863 mAh/g and 469 mAh/g for cycle 1 and cycle 2 respectively (Figure 3.4b), yielding a lower initial capacity and a more drastic capacity fade in the second cycle with only 54% reversibility. At cycle 50, the capacity is 261 mAh/g and the capacity retention is 56%.

The difference in initial capacity and capacity retention between CoNC@S and acid-washed CoNC@S samples suggests that Co nanoparticles have a significant effect on facilitating sulfur reactivity in Na-S battery systems. The small increase in porosity (from BET) in acid-washed CoNC doesn't affect the sulfur reactivity as much as the diminished Co content. Figure 3.4c and 3.4d compare the discharge and charge curves of CoNC@S and acid-washed CoNC@S at cycle 1, 2, 5 and 10. From the discharge and charge curves, the 1st charge capacity in acid-washed CoNC@S is 445 mAh/g (Figure 3.4d), which is much lower compared to that of CoNC@S (734 mAh/g, Figure 3.4c). The charge capacity also decreases drastically with cycling for acid-washed CoNC@S, while that of CoNC@S is quite stable. In addition, the charge profiles for acid-washed CoNC@S contain two voltage plateaus at 1.6-1.9 V and 2.0-2.25 V respectively, while CoNC@S exhibits one voltage plateaus at 1.6-2.05 V. The difference in both charge capacity and the shape of the charge profiles suggests different activity in the reverse oxidation of Na_2S to sodium polysulfides and S_8.

To investigate the difference in charge and discharge profiles between the two samples, differential capacity curves are shown in Figure 3.4e and Figure 3.4f. For CoNC@S (Fig. 3.4e), two peaks are observed for the initial discharge at 1.45 V and 1.2 V. In the following cycles, three peaks during discharge at 1.85 V, 1.5 V and 1.25 V can be observed. The differential capacity curves are consistent with previous studies, where the peak at 1.85 V is attributed to the reduction of sulfur to long chain polysulfides, and the following two peaks correspond to further sodiation to Na_2S_4, and then to Na_2S.[14,23,54] The discharge peaks gradually shift to positive potential, indicating decrease in overpotential with cycling.[55] Acid-washed CoNC@S shows similar discharge behavior, with discharge peaks at 1.85 V, 1.55 V and 1.2 V respectively (Figure 3.4f). The differential capacity peak intensity decreases with cycling, which is associated with the capacity fade seen in Figure 3.4d.

For the charging process, CoNC@S exhibits one broad peak from 1.5 V to 2.2 V with a maximum at 1.8 V during charge, while two separated charge peaks at 1.75 V and 2.1 V are observed for acid-washed CoNC@S, which can be assigned to oxidation of Na_2S to Na_2S_4 and further desodiation to S_8.[56] The single charge peak at lower potential indicates a smaller overall polarization as well as facile reactivity of polysulfide intermediates during the conversion from Na_2S to sodium polysulfides and S_8, which is also supported by the higher charge capacity of CoNC@S relative to acid-washed CoNC@S. The improved charging behavior of CoNC@S suggests that the increased presence of available Co nanoparticles in the carbon framework facilitates the charging step, which is crucial to reversible sulfur utilization and capacity retention.

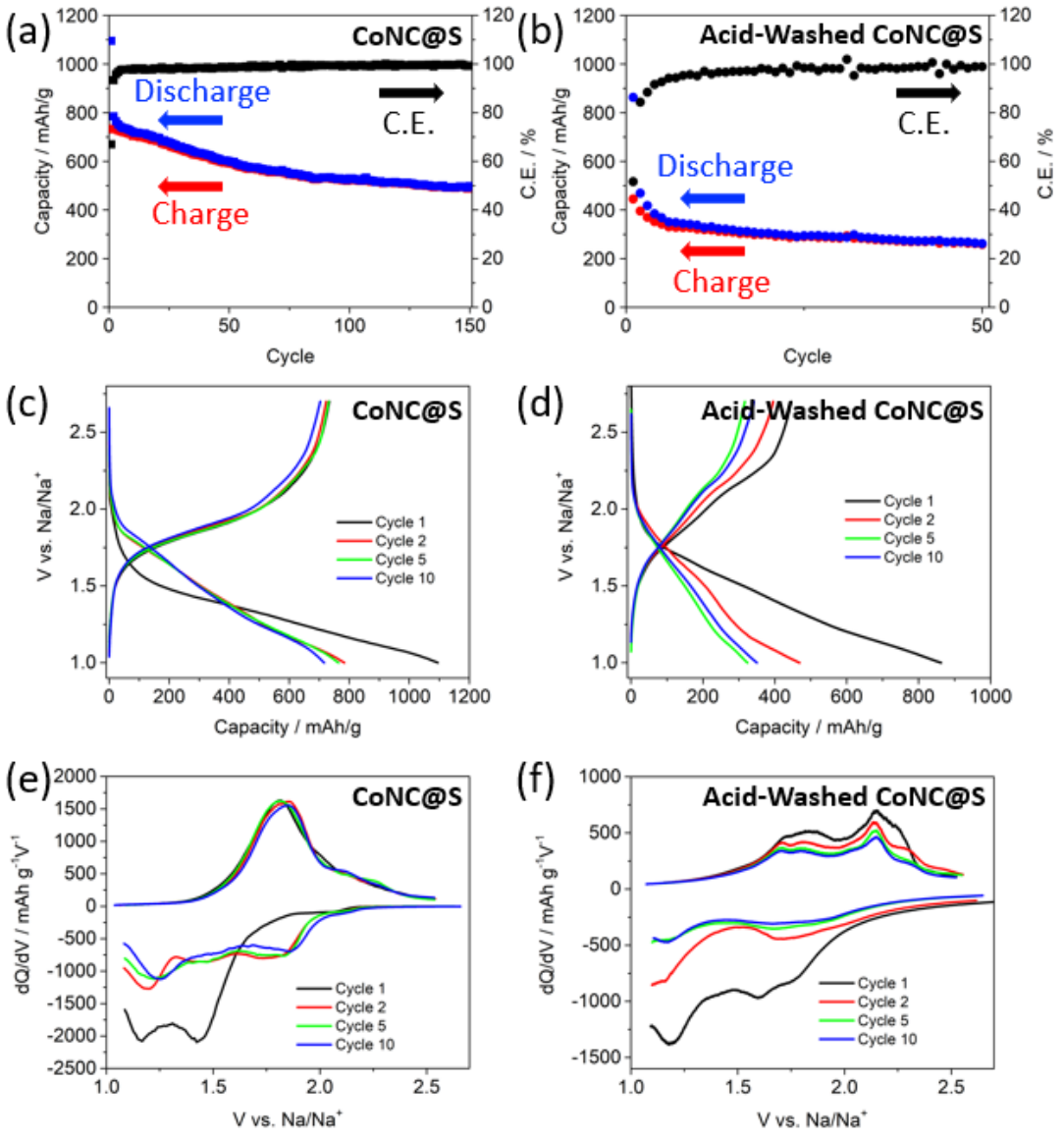

Figure 3.4. Cycling performance of the CoNC@S (a), and (b) acid-washed CoNC@S samples and the corresponding discharge-charge curves (c, d), and differential capacity plots (e, f). The current density is 80 mA/g, corresponding to 0.1 C for the CoNC@S samples.

Electrochemical impedance spectroscopy (EIS) reveals a smaller charge transfer resistance R_{ct} for CoNC@S compared to acid-washed CoNC@S (Figure 3.5), confirming the improved reactivity of sulfur with more Co content. The improvement in sulfur utilization

leading to improved capacity and capacity retention from the presence of Co nanoparticles in this concentrated electrolyte system is likely associated with improved electrocatalytic conversion of Na_2S to S_8. We note that while 4.3% Co remains in the acid-washed CoNC, the remaining Co is likely inaccessible by acid. We suggest that this acid-inaccessibility may also lead to electrolyte inaccessibility to the Co in the battery and thus inactivity of this Co in a Na-S system. N-doped carbon has also been reported to have a positive effect on polysulfide retention, which results in sulfur battery capacity retention.[27,55,57] In our system, polysulfide dissolution is mitigated by the use of a concentrated electrolyte, as reported previously in NaTFSI/pentaglyme system.[18] In contrast, shuttle effect is observed in dilute 1 M NaFSI/DME electrolyte (Figure 3.6), suggesting that N-doped sites are not sufficient for polysulfide retention in this system.

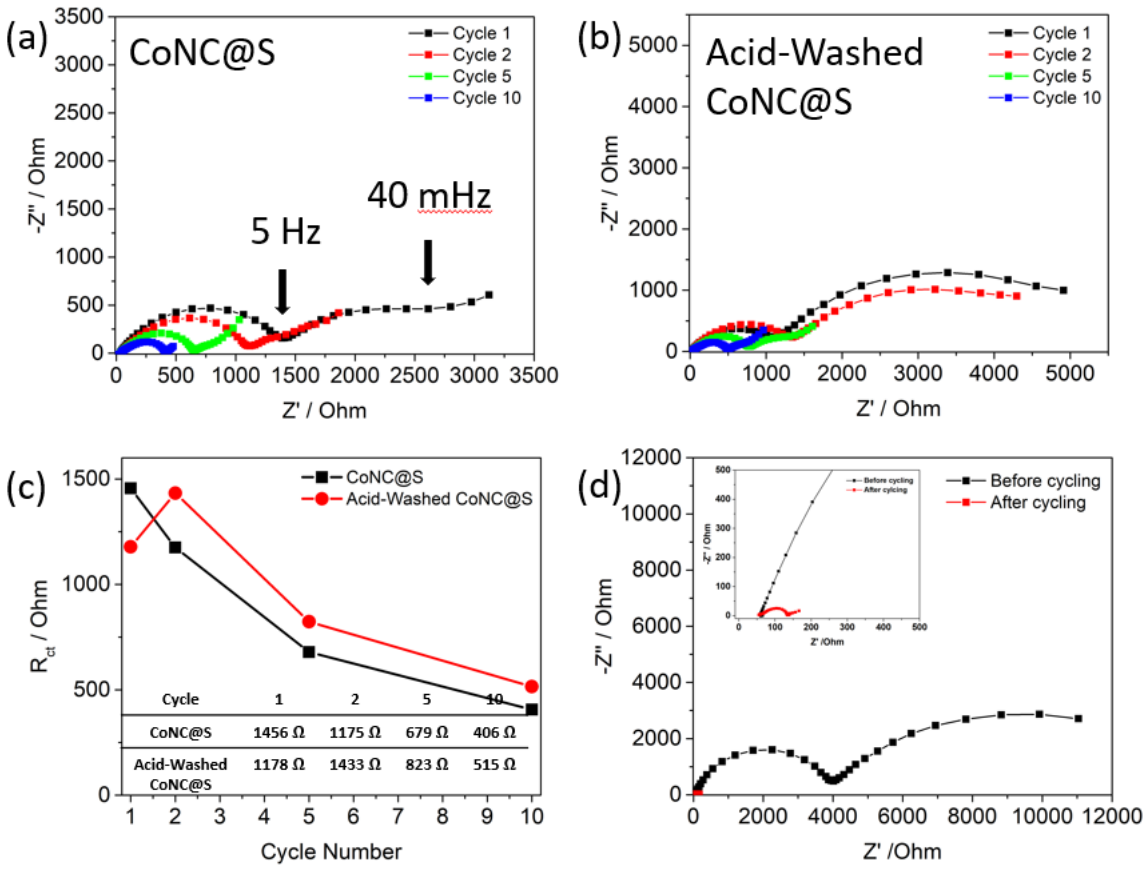

Figure 3.5 (cont.)

Figure 3.5. Electrochemical impedance spectra of (a) CoNC@S and (b) acid-washed CoNC@S samples and (c) corresponding evolution of R_{ct} with cycle number. (d) Electrochemical impedance spectra of Na/Na symmetric cell using NaFSI/DME/BTFE electrolyte (inset: zoomed in EIS spectra). The semicircle in the mid-frequency range can be assigned to a passivation layer on Na metal, which disappears with cycling via electrochemical polishing.[58]

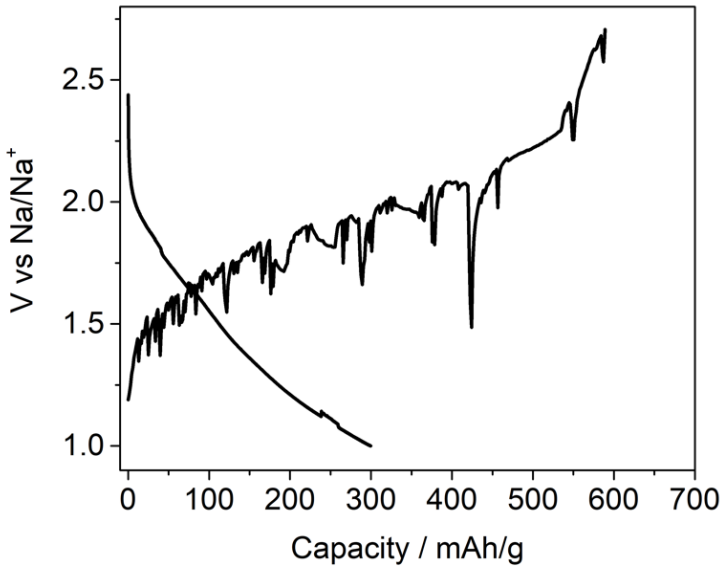

Figure 3.6. Typical discharge-charge curves of CoNC@S in 1 M NaFSI/DME. The current density is 80 mA/g.

Further studies are carried out to evaluate the electrochemical performance of CoNC@S. Figure 3.7a and 3.7b show the C-rate-dependent capacity and representative discharge and charge curves at various C rates. The capacities are 1079 mAh/g, 612 mAh/g, 413 mAh/g and 255 mAh/g at 0.1 C (80 mA/g), 0.25 C (160 mA/g), 1 C (400 mA/g) and 2.5 C (800 mA/g) respectively. When the C-rate returns to 0.1 C, a capacity of 700 mAh/g is obtained, suggesting a good capacity recovery after fast cycling rates. Figure 3.7c and 3.7d show the cyclic

voltammograms (CV) obtained at various scan rates and the corresponding plots of natural logarithm of peak anodic and cathodic currents versus natural logarithm of scan rates. The slopes for the linear plots are 0.56 and 0.67 for anodic and cathodic peak currents respectively, which indicates that a diffusion-controlled process is the dominant contributor to the capacity, as expected.[12,59]

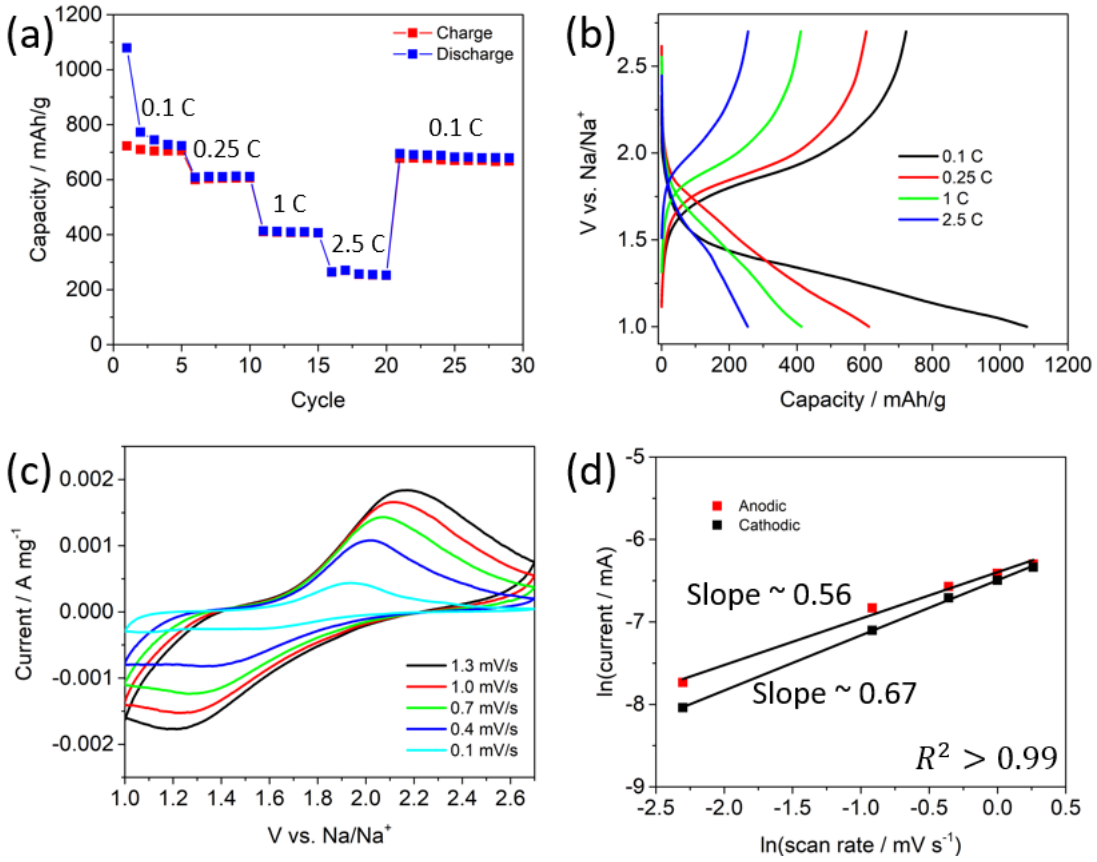

Figure 3.7. (a) C-rate-dependent performance of CoNC@S. (b) Discharge-charge curves at different C-rates. (c) CV of CoNC@S at various scan rates. (d) The plot of ln(peak current) versus ln(scan rate) derived from CV.

Postmortem XPS was carried out to investigate Co speciation after cycling. CoNC@S samples are characterized after 10 cycles. Figure 3.8a shows the Co 2p XPS spectra obtained

following discharge and charge. Interestingly, two peaks are observed at 779.6 eV ($2p_{3/2}$) and 795.0 eV ($2p_{1/2}$), which are lower in binding energy compared to the cobalt oxide and Co-N species in the CoNC sample before cycling (Figure 3.3a). In addition, no satellite peaks can be observed after cycling, as opposed to the prominent satellite peaks present before cycling. The 779.6 eV and 795.0 eV binding energy, together with weak satellite peaks, suggests the presence of a Co-S bond, possibly from CoS or CoS_2.[60,61,62] The difference in Co photoemission spectra in spectra obtained before and after cycling suggests that the Co speciation has evolved during battery cycling.

The origin of the different oxidation state behavior reflects the Co environment. Since the as-prepared CoNC sample is handled in ambient environment during cathode preparation, the Co nanoparticles become surface oxidized state due to inevitable exposure to ambient oxygen. This exposure is reflected in the Co oxides inferred from the XPS prior to cycling (Figure 3.3a). During cycling the cathode is maintained at a potential between 1.0-2.7 V vs. Na/Na^+, which is a much more reducing (and oxygen free) environment compared to the as-prepared cathode. Indeed, Cobalt oxide species exhibit redox activity in Na battery systems.[63,64] As suggested by the postmortem characterization, the Co content transforms to become a cobalt sulfide species such as CoS or CoS_2 in the presence of elemental S. This new species is stable with cycling as no change is seen between the Co 2p XPS spectra obtained following charge and following discharge.

Figure 3.8b shows the S 2p XPS spectra obtained from the discharged and charged samples. For both samples, two S $2p_{3/2}$ peaks are present at 168.3 eV and 166.2 eV, which are attributed to the presence of decomposition products of NaFSI, which is known to occur upon cycling.[65,66] The peak at 159.4 eV ($2p_{3/2}$) in the discharge sample is associated with the presence

of Na_2S.[8,67] This peak is absent in the charged sample, and a new peak is present at 163.3 eV ($2p_{3/2}$), which is associated with the presence of elemental sulfur S_8.[14,51] The presence of Na_2S and elemental sulfur S_8 in the discharged and charged samples, respectively, supports the reversible sulfur reactivity of the system.

Interestingly, XPS peaks ranging from 160 eV to 162.5 eV are also observed in both samples. These binding energies could be assigned to various cobalt sulfides.[59,68,69,70] However, the peaks between 160 eV and 162.6 eV could also originate from short-chain sodium polysulfides Na_2S_x ($1<x\leq4$) due to incomplete sulfur reactivity, as observed previously in Na-S batteries.[7,12,71] Thus, overlap in the XPS of CoS and sodium polysulfide species limits the utility of S 2p XPS in evaluating the state of Co in this system. Therefore, further studies need to be carried out to understand the change in Co speciation after cycling.

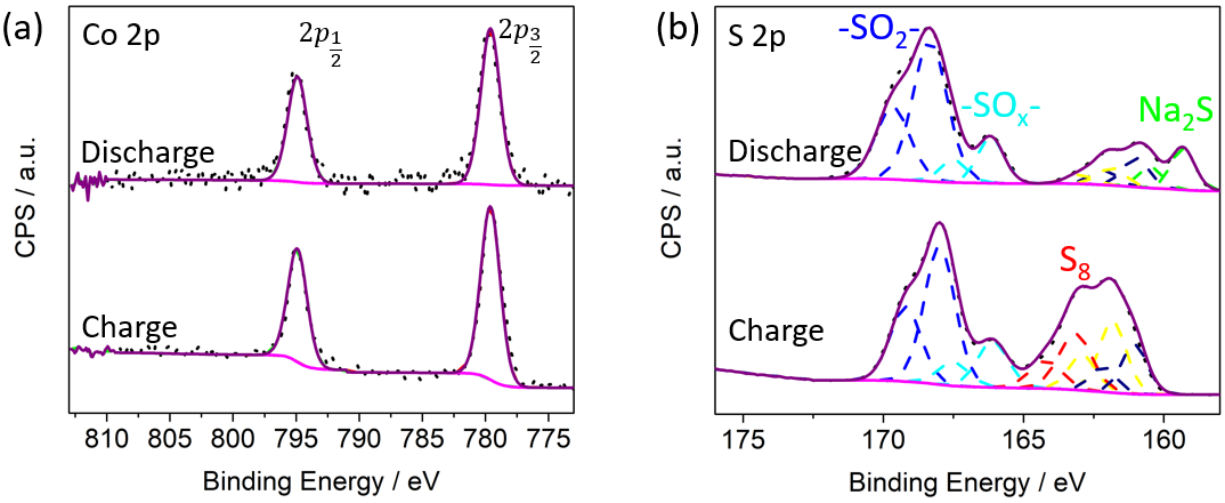

Figure 3.8. XPS spectra for (a) Co 2p and (b) S 2p of the discharge and charge CoNC@S samples after 10 cycles. The color dashed lines represent fits of different species to the XPS. Components in S 2p XPS spectra include $-SO_2-$ (blue), $-SO_x-$ (light blue), S_8 (red), Na_2S (green), Na_2S_4 (yellow) and Na_2S_2 (navy).

3.3.2 Use of a Nano Co + Nano S Cathode to Enable SAED

In order to evaluate Co speciation following charge and discharge, we utilized TEM imaging and SAED. Here we note that XRD was unable to detect the Co nanoparticles on the cathode due to small loading (Figure 3.9), which has been the case in previous studies.[72,73] The cathode in this case was formed by using Co nanoparticles (Nano Co) combined with S nanoparticles (Nano S) alone, absent the carbon framework. The carbon framework in the CoNC samples was found to limit SAED pattern resolution and yield lower resolution images. In the Nano Co + Nano S cathodes, the electronic conductivity of the porous sulfur host is sacrificed, and the sulfur reactivity is expected to decrease. Nano S is used as a compromise to improve Na^+ diffusion and sulfur utilization.[74] Ketjenblack (1400 m^2/g) is used as higher surface area conductive carbon instead of Super P (62 m^2/g) to promote sulfur reactivity, as demonstrated in previous studies.[75]

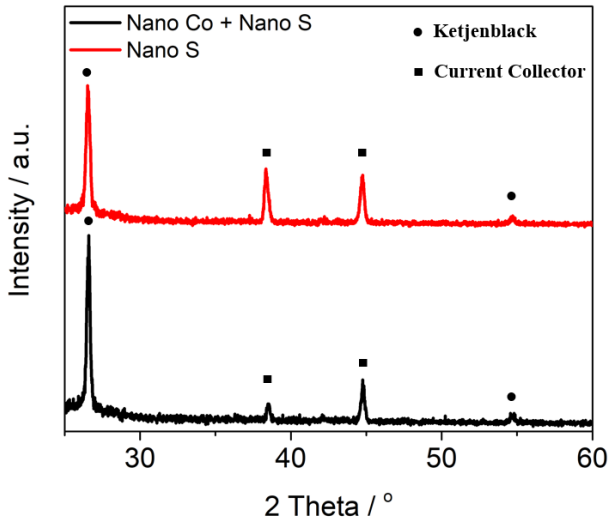

Figure 3.9. XRD patterns of pristine Nano Co + Nano S and Nano S cathodes.

Figure 3.10a and 3.10b show the discharge and charge curves and the corresponding differential capacity plots of the Nano S and Nano Co + Nano S cathodes. Consistent with the

CoNC@S and acid-washed CoNC@S samples (Figure 3.4), the charge profiles for the Nano S sample contain two voltage plateaus at 1.7-2.0 V and 2.1-2.25 V respectively, while the Nano Co + Nano S cathode exhibits one voltage plateau at 1.7-2.25 V and a higher capacity. The differential capacity curves show discharge peaks at 1.85 V, 1.5 V and 1.2 V (Figure 3.10b). One broad charge peak with maximum at 1.8 V is observed for Nano Co + Nano S, and two charge peaks are present at 1.8 V and 2,15 V for Nano S alone, which agrees with the differential capacity curve found for the CoNC@S and acid-washed CoNC@S samples (Figure 3.4e and Figure 3.4f). The presence of Co nanoparticles enables a higher charging capacity via a single charge peak at lower potential, facilitating reverse oxidation of Na_2S. The similarity in the electrochemical behavior compared with the CoNC@S samples suggests that Co nanoparticles in the Nano S + Nano Co sample exhibit the same electrocatalytic effect on sulfur reactivity, and thus undergo the same change in Co speciation with cycling relative to the CoNC@S sample.

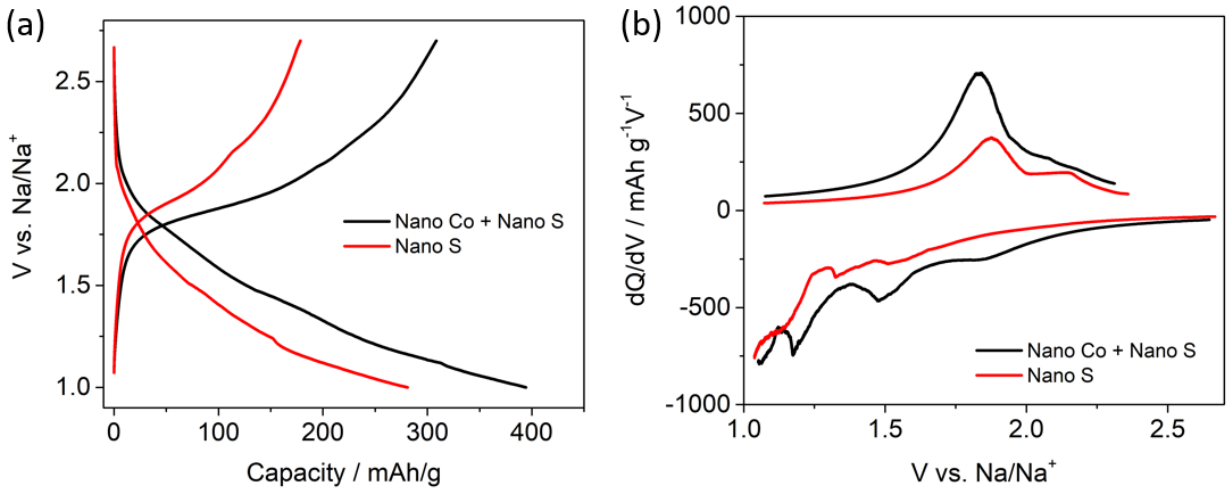

Figure 3.10. (a) Discharge-charge curves and corresponding (b) differential capacity plots of Nano Co + Nano S and Nano S alone at cycle 2. The current density is 20 mA/g.

Having established that the Nano Co + Nano S cathode exhibits reactivity similar to that found in the CoNC@S cathode (albeit with much lower capacity), we next interrogated the Nano Co + Nano S cathode with TEM and SAED. The cycled samples were prepared by cycling for 10 cycles and stopping at 1.8 V during charge; this potential is where the maximum activity in Na_2S oxidation is found, as suggested by the maximum in differential charge capacity (Figure 3.10b).

Figure 3.11a and 3.11b show the TEM images and the corresponding SAED patterns of the Co nanoparticles in the Nano Co + Nano S cathode before and after cycling. Before cycling, the inset to Figure 3.11a shows the Co nanoparticles are spherical, and the SAED pattern presents diffraction rings that can be assigned to (002) planes of Co and (112) planes of Co_3O_4.[76,77,78] The (112) lattice planes of Co_3O_4 have been reported previously to be surface located, suggesting that this species might be present on the surface of Co nanoparticles prior to cycling (Figure 3.3a).[78,79]

After cycling, the inset to Figure 3.11b shows the Co nanoparticle exhibits a distinct change in morphology in that the particle appears irregular in shape and expanded relative to the Co nanoparticle observed before cycling. The SAED pattern in Figure 3.11b contains diffraction rings corresponding to the (100) and (101) planes of CoS.[69,80,81] No diffraction rings could be attributed to either Co or Co_3O_4, indicating that these species are no longer present in the cathode following cycling.

Figure 3.11c shows the high-resolution transmission electron microscopy (HR-TEM) image of the cycled Co nanoparticle. Lattice fringes can be observed with interplanar spacing of 5.17 Å, which can be assigned to the (001) plane of CoS.[82] The SAED patterns and HR-TEM image strongly suggest that the Co nanoparticles transform into CoS nanoparticles during cycling.

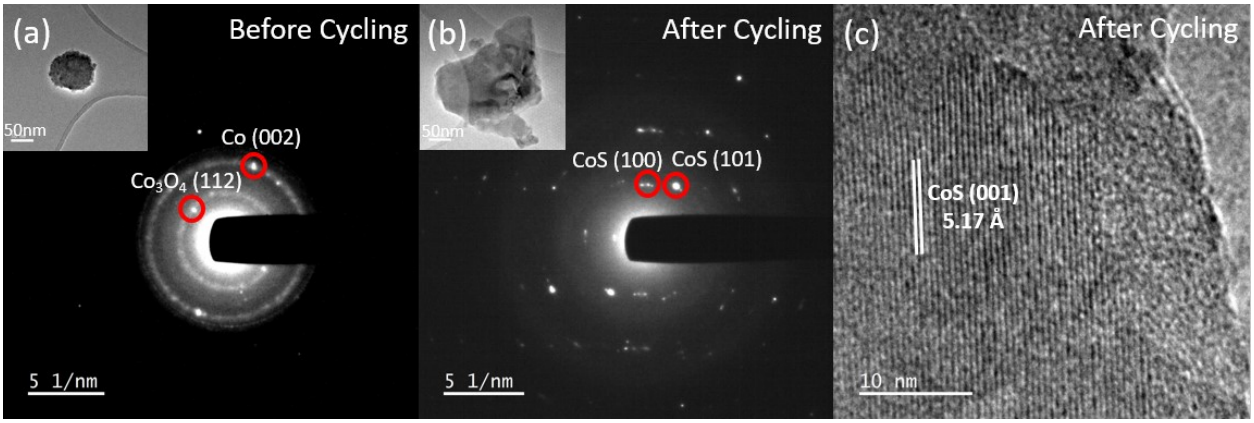

Figure 3.11. SAED patterns (inset: TEM images) of Co nanoparticles (a) before cycling, and (b) after cycling. (c) HR-TEM image of the Co nanoparticles after cycling.

3.3.3 Study of CoS in Na-S Batteries

CoS nanoparticles have been reported to facilitate redox conversion of sulfur species in Li-S batteries.[33,83,84] We suggest that CoS could also be an electrocatalyst in Na-S battery as well. We compared the cycling performance of Nano S with and without CoS (Figure 3.12). Greater capacity can be achieved with Nano S containing CoS, confirming its electrocatalytic activity. We note that previous studies have shown that the potential to initiate redox activity in CoS in Na systems is 0.7 V vs. Na/Na^+, which is not within our voltage window.[69] In addition, CoS redox involves reduction of Co^{2+} to Co(0). As suggested by XPS study on CoNC@S (Figure 3.8a), no Co(0) can be observed in the discharged sample, which suggests that Co species remains as Co^{2+} during cycling in our system. Therefore, we consider the capacity contribution of CoS to be minimal, and the increase in capacity in Nano CoS + Nano S compared with Nano S is due to the presence of a CoS catalytic effect on S conversion.

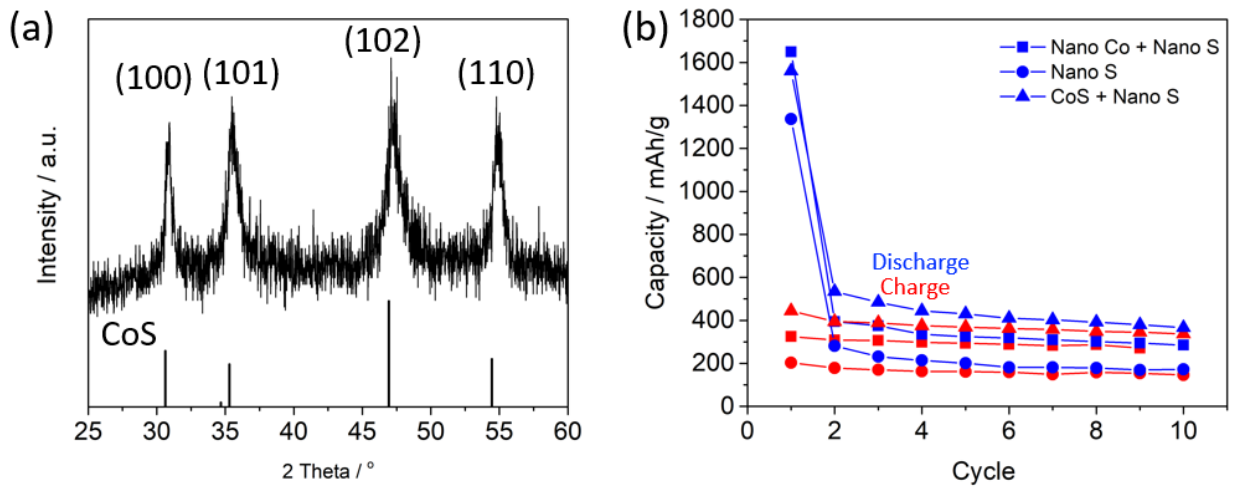

Figure 3.12. (a) XRD pattern for CoS. (b) Cycling performance of the sulfur nanoparticles with CoS. The current density is 20 mA/g.

To understand the origin of the catalytic effect of CoS in a Na-S battery. We carried out Raman spectroscopy to study the interaction between Na_2S and CoS. Figure 3.13 shows the Raman spectra of Na_2S, CoS, and Na_2S + CoS. The pure Na_2S spectrum exhibits a peak at 187 cm^{-1}, consistent with previous studies.[8] The CoS spectrum exhibits no peaks in the Raman shift region shown. Prior work on partially oxidized samples revealed a peak at 382 cm^{-1} attributed to CoS.[85] This peak was not observed in the fully reduced sample here. A new broad peak emerges in the Na_2S + CoS spectrum. The peak exhibits its maximum from 439 cm^{-1} to 490 cm^{-1}. This broad band has been attributed to Na_2S_2 (457 cm^{-1}) and Na_2S_4 (437 cm^{-1}).[8,86] The emergence of this peak indicates that the presence of CoS facilitates the oxidation of Na_2S to products such as Na_2S_2 and Na_2S_4. We suggest the CoS is then partially reduced. Raman spectroscopy results consequently support the catalytic effect of CoS in the Na-S battery, which facilitates Na_2S oxidation.

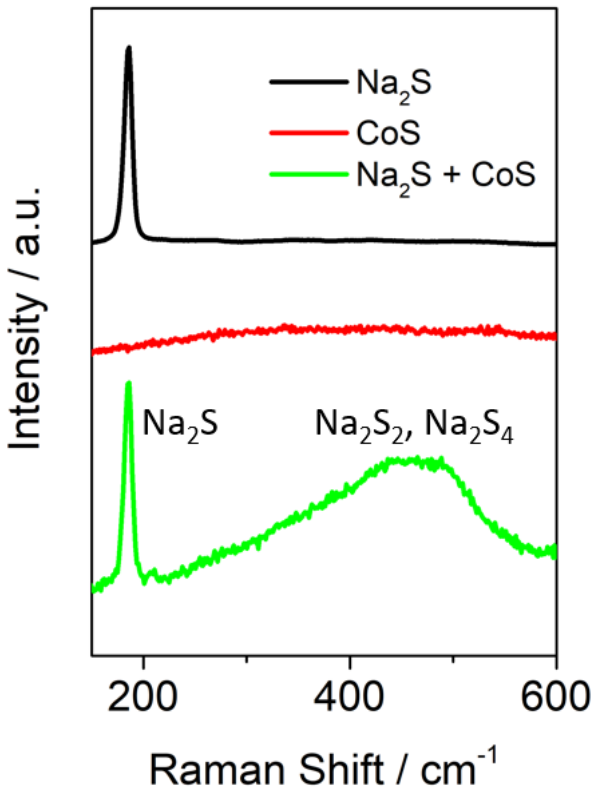

Figure 3.13. Raman spectra of Na_2S, CoS and Na_2S + CoS.

3.4 Discussions

The results above show that addition of Co nanoparticles to a Na-S cathode yields increased S utilization and better cyclability relative to a Na-S cathode absent the Co nanoparticles. The effect appears to be greatest in systems that have a higher nanoparticle density relative to that with a lower concentration of Co nanoparticles. Interestingly, the XPS studies, together with TEM and SAED, suggest that the Co converts to become CoS during battery cycling. Thus the electrocatalyst which facilitates Na_2S oxidation is CoS rather than Co nanoparticles or Co oxides (Figure 3.14). CoS is determined to pose a catalytic effect on sulfur reactivity. The conversion of Co to CoS is irreversible, as suggested by the XPS measurements on CoNC@S before and after cycling, which is consistent with previous studies.[84] In CoNC@S,

the irreversible conversion of the 9.3% Co to CoS would consume 5% S and thus lead to a 5% decrease in the 1675 mAh/g theoretical capacity of S (84 mAh/g).

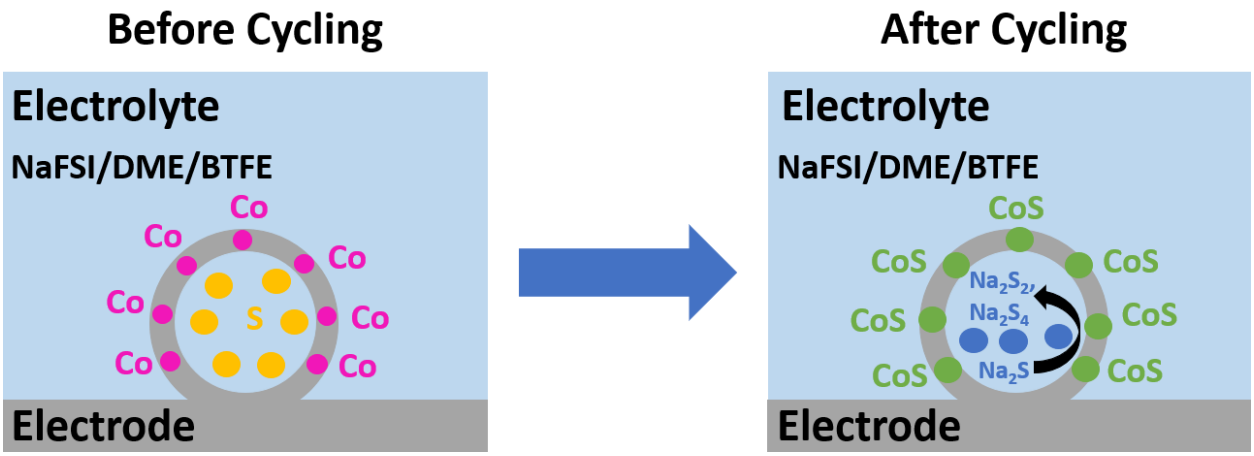

Figure 3.14. The schematic diagram of the catalytic effect of Co nanoparticles in a Na-S battery. Co nanoparticles convert to CoS after cycling. CoS facilitates Na_2S oxidation.

With regarding to transformation of Co to CoS in our system, previous studies have shown that CoS can form by electrochemically cycling Co in Na_2S_4 solution via cyclic voltammetry.[84] Other studies have reported on synthesis of CoS by immersing Co_3O_4 into Na_2S solution.[87,88] In this study, we show that the S_8 + Co environment in the cathode also facilities a redox reaction wherein Co metal is converted to CoS at the potentials experienced by the Na-S cathode. We note that in prior studies, conversion of Co into CoS (in a context different from that reported here) required repeated (250 cycles) oxidation/reduction of a Co surface in Na_2S_4 solution via cyclic voltammetry. This result suggests the conversion of Co into CoS is slow and further suggests that repeated cycling is required to obtain CoS formation (10 cycles in our study).[84] The conversion of Co to CoS is not observed in differential capacity plots. Since CoS formation takes place slowly through multiple cycles, charge passed from the sulfur consumption

required to convert Co into CoS would spread out over multiple cycles, and would be hard to observe relative to the charge from general Na-S reactivity.

In addition, the postmortem Co 2p XPS spectra shows no change between the charge and discharge samples (Figure 3.8a), indicating that the Co valence state is stable within the 1.0-2.7 V window used for cycling and thus the CoS formed during cycling is stable. In agreement with our XPS data, previous studies have reported that CoS is only redox active in Na systems below 1 V.[69]

We used Raman to investigate the origin of the electrocatalytic activity of CoS in the Na-S cathode. The emergence of peaks associated with Na_2S_2 and Na_2S_4 after mixing Na_2S with CoS suggests that Na_2S is converted to more oxidized sodium sulfides in the presence of the CoS. This result supports the presence of a catalytic effect associated with CoS in Na-S batteries. The CoS promotes facile oxidation of Na_2S. Indeed, the facile conversion of Na_2S enabled by CoS is demonstrated by the higher charging capacity in the presence of higher Co content in both the CoNC@S (Figure 3.4) and Nano Co + Nano S (Figure 3.10) systems.

Our study demonstrates the importance of postmortem studies in understanding Co-based electrocatalysts in sulfur battery systems. To utilize sulfur redox reactivity, sulfur batteries are cycled to quite reducing potentials. Since the electrocatalysts are usually prepared under ambient conditions, the Co species in the as-prepared cathode are likely to exhibit valence states different from those occurring at the actual operating potentials of the sulfur battery. The stability window of the catalyst must be taken into consideration, as pointed out in previous studies incorporating MnO_2, CuO, and VO_2 in Li-S systems.[28,89,90]

3.5 Conclusions

In summary, we utilized a MOF-derived Co-decorated CoNC porous carbon as sulfur host in a Na-S battery. A NaFSI/DME/BTFE concentrated electrolyte is used for the first time with a sulfur cathode to mitigate polysulfide dissolution. We found that the presence of Co promotes high sulfur utilization. Postmortem XPS, TEM, and SAED show that CoS is formed in place of Co nanoparticles and CoN_4 sites during cycling. Raman spectroscopy supports the catalytic effect of CoS on Na_2S oxidation to Na_2S_2 and Na_2S_4. Our study highlights an opportunity to explore cobalt sulfides/carbon composites as catalytic sulfur host for high-performance Na-S batteries.

3.6 References

1. Li, M.; Lu, J.; Ji, X.; Li, Y.; Shao, Y.; Chen, Z.; Zhong, C.; Amine, K., Design Strategies for Nonaqueous Multivalent-Ion and Monovalent-Ion Battery Anodes. *Nat. Rev. Mater.* **2020,** *5*, 276-294.

2. Yan, G.; Mariyappan, S.; Rousse, G.; Jacquet, Q.; Deschamps, M.; David, R.; Mirvaux, B.; Freeland, J. W.; Tarascon, J.-M., Higher Energy and Safer Sodium Ion Batteries via an Electrochemically Made Disordered $Na_3V_2(PO_4)_2F_3$ Material. *Nat. Commun.* **2019,** *10*, 585.

3. Yang, C.-P.; Yin, Y.-X.; Guo, Y.-G.; Wan, L.-J., Electrochemical (De)Lithiation of 1D Sulfur Chains in Li–S Batteries: A Model System Study. *J. Am. Chem. Soc.* **2015,** *137*, 2215-2218.

4. Manthiram, A.; Fu, Y.; Chung, S.-H.; Zu, C.; Su, Y.-S., Rechargeable Lithium–Sulfur Batteries. *Chem. Rev.* **2014,** *114*, 11751-11787.

5. Wang, Y.-X.; Zhang, B.; Lai, W.; Xu, Y.; Chou, S.-L.; Liu, H.-K.; Dou, S.-X., Room-Temperature Sodium-Sulfur Batteries: A Comprehensive Review on Research Progress and Cell Chemistry. *Adv. Energy Mater.* **2017,** *7*, 1602829.

6. Xin, S.; Yin, Y.-X.; Guo, Y.-G.; Wan, L.-J., A High-Energy Room-Temperature Sodium-Sulfur Battery. *Adv. Mater.* **2014,** *26*, 1261-1265.

7. Manthiram, A.; Yu, X., Ambient Temperature Sodium–Sulfur Batteries. *Small* **2015,** *11*, 2108-2114.

8. Xu, X.; Zhou, D.; Qin, X.; Lin, K.; Kang, F.; Li, B.; Shanmukaraj, D.; Rojo, T.; Armand, M.; Wang, G., A Room-Temperature Sodium–Sulfur Battery with High Capacity and Stable Cycling Performance. *Nat. Commun.* **2018,** *9*, 3870.

9. Wang, A.; Hu, X.; Tang, H.; Zhang, C.; Liu, S.; Yang, Y.-W.; Yang, Q.-H.; Luo, J., Processable and Moldable Sodium-Metal Anodes. *Angew. Chem. Int. Ed.* **2017,** *56*, 11921-11926.

10. Komaba, S.; Ishikawa, T.; Yabuuchi, N.; Murata, W.; Ito, A.; Ohsawa, Y., Fluorinated Ethylene Carbonate as Electrolyte Additive for Rechargeable Na Batteries. *ACS Appl. Mater. Interfaces* **2011,** *3*, 4165-4168.

11. Adelhelm, P.; Hartmann, P.; Bender, C. L.; Busche, M.; Eufinger, C.; Janek, J., From Lithium to Sodium: Cell Chemistry of Room Temperature Sodium–Air and Sodium–Sulfur Batteries. *Beilstein J. Nanotechnol.* **2015,** *6*, 1016-1055.

12. Wei, S.; Xu, S.; Agrawral, A.; Choudhury, S.; Lu, Y.; Tu, Z.; Ma, L.; Archer, L. A., A Stable Room-Temperature Sodium–Sulfur Battery. *Nature Commun.* **2016,** *7*, 11722.

13. Fan, L.; Ma, R.; Yang, Y.; Chen, S.; Lu, B., Covalent Sulfur for Advanced Room Temperature Sodium-Sulfur Batteries. *Nano Energy* **2016,** *28*, 304-310.

14. Zhang, B.-W.; Sheng, T.; Liu, Y.-D.; Wang, Y.-X.; Zhang, L.; Lai, W.-H.; Wang, L.; Yang, J.; Gu, Q.-F.; Chou, S.-L.; Liu, H.-K.; Dou, S.-X., Atomic Cobalt as an Efficient Electrocatalyst in Sulfur Cathodes for Superior Room-Temperature Sodium-Sulfur Batteries. *Nat. Commun.* **2018,** *9*, 4082.

15. Suo, L.; Hu, Y.-S.; Li, H.; Armand, M.; Chen, L., A New Class of Solvent-in-Salt Electrolyte for High-Energy Rechargeable Metallic Lithium Batteries. *Nat. Commun.* **2013,** *4*, 1481.

16. Shin, E. S.; Kim, K.; Oh, S. H.; Cho, W. I., Polysulfide Dissolution Control: the Common Ion Effect. *Chem. Commun.* **2013,** *49*, 2004-2006.

17. Zheng, J.; Lochala, J. A.; Kwok, A.; Deng, Z. D.; Xiao, J., Research Progress towards Understanding the Unique Interfaces between Concentrated Electrolytes and Electrodes for Energy Storage Applications. *Adv. Sci.* **2017,** *4*, 1700032.

18. Terada, S.; Susa, H.; Tsuzuki, S.; Mandai, T.; Ueno, K.; Umebayashi, Y.; Dokko, K.; Watanabe, M., Dissociation and Diffusion of Glyme-Sodium Bis(trifluoromethanesulfonyl)amide Complexes in Hydrofluoroether-Based Electrolytes for Sodium Batteries. *J. Phys. Chem. C* **2016,** *120*, 23339-23350.

19. Terada, S.; Mandai, T.; Nozawa, R.; Yoshida, K.; Ueno, K.; Tsuzuki, S.; Dokko, K.; Watanabe, M., Physicochemical Properties of Pentaglyme–Sodium Bis(trifluoromethanesulfonyl)amide Solvate Ionic Liquid. *Phys. Chem. Chem. Phys.* **2014,** *16*, 11737-11746.

20. Galle Kankanamge, S. R.; Li, K.; Fulfer, K. D.; Du, P.; Jorn, R.; Kumar, R.; Kuroda, D. G., Mechanism behind the Unusually High Conductivities of High Concentrated Sodium Ion Glyme-Based Electrolytes. *J. Phys. Chem. C* **2018,** *122*, 25237-25246.

21. Cao, R.; Mishra, K.; Li, X.; Qian, J.; Engelhard, M. H.; Bowden, M. E.; Han, K. S.; Mueller, K. T.; Henderson, W. A.; Zhang, J.-G., Enabling Room Temperature Sodium Metal Batteries. *Nano Energy* **2016,** *30*, 825-830.

22. Zheng, J.; Chen, S.; Zhao, W.; Song, J.; Engelhard, M. H.; Zhang, J.-G., Extremely Stable Sodium Metal Batteries Enabled by Localized High-Concentration Electrolytes. *ACS Energy Lett.* **2018,** *3*, 315-321.

23. Wang, Y.-X.; Yang, J.; Lai, W.; Chou, S.-L.; Gu, Q.-F.; Liu, H. K.; Zhao, D.; Dou, S. X., Achieving High-Performance Room-Temperature Sodium–Sulfur Batteries With S@Interconnected Mesoporous Carbon Hollow Nanospheres. *J. Am. Chem. Soc.* **2016,** *138*, 16576-16579.

24. Liu, D.; Zhang, C.; Zhou, G.; Lv, W.; Ling, G.; Zhi, L.; Yang, Q.-H., Catalytic Effects in Lithium–Sulfur Batteries: Promoted Sulfur Transformation and Reduced Shuttle Effect. *Adv. Sci.* **2018,** *5*, 1700270.

25. Liu, X.; Huang, J.-Q.; Zhang, Q.; Mai, L., Nanostructured Metal Oxides and Sulfides for Lithium–Sulfur Batteries. *Adv. Mater.* **2017,** *29*, 1601759.

26. Al Salem, H.; Babu, G.; V. Rao, C.; Arava, L. M. R., Electrocatalytic Polysulfide Traps for Controlling Redox Shuttle Process of Li–S Batteries. *J. Am. Chem. Soc.* **2015,** *137*, 11542-11545.

27. Li, Y.-J.; Fan, J.-M.; Zheng, M.-S.; Dong, Q.-F., A Novel Synergistic Composite with Multi-Functional Effects for High-Performance Li–S Batteries. *Energy Environ. Sci.* **2016,** *9*, 1998-2004.

28. Liang, X.; Hart, C.; Pang, Q.; Garsuch, A.; Weiss, T.; Nazar, L. F., A Highly Efficient Polysulfide Mediator for Lithium–Sulfur Batteries. *Nat. Commun.* **2015,** *6*, 5682.

29. Pang, Q.; Kundu, D.; Cuisinier, M.; Nazar, L. F., Surface-Enhanced Redox Chemistry of Polysulphides on a Metallic and Polar Host for Lithium-Sulphur Batteries. *Nat. Commun.* **2014,** *5*, 4759.

30. Yuan, Z.; Peng, H.-J.; Hou, T.-Z.; Huang, J.-Q.; Chen, C.-M.; Wang, D.-W.; Cheng, X.-B.; Wei, F.; Zhang, Q., Powering Lithium–Sulfur Battery Performance by Propelling Polysulfide Redox at Sulfiphilic Hosts. *Nano Lett.* **2016,** *16*, 519-527.

31. Wang, H.; Zhang, Q.; Yao, H.; Liang, Z.; Lee, H.-W.; Hsu, P.-C.; Zheng, G.; Cui, Y., High Electrochemical Selectivity of Edge versus Terrace Sites in Two-Dimensional Layered MoS_2 Materials. *Nano Lett.* **2014,** *14*, 7138-7144.

32. Wang, W.; Zhao, Y.; Zhang, Y.; Wang, J.; Cui, G.; Li, M.; Bakenov, Z.; Wang, X., Defect-Rich Multishelled Fe-Doped Co_3O_4 Hollow Microspheres with Multiple Spatial Confinements to Facilitate Catalytic Conversion of Polysulfides for High-Performance Li–S Batteries. *ACS Appl. Mater. Interfaces* **2020,** *12*, 12763-12773.

33. He, J.; Chen, Y.; Manthiram, A., Metal Sulfide-Decorated Carbon Sponge as a Highly Efficient Electrocatalyst and Absorbant for Polysulfide in High-Loading Li_2S Batteries. *Adv. Energy Mater.* **2019,** *9*, 1900584.

34. Chen, T.; Zhang, Z.; Cheng, B.; Chen, R.; Hu, Y.; Ma, L.; Zhu, G.; Liu, J.; Jin, Z., Self-Templated Formation of Interlaced Carbon Nanotubes Threaded Hollow Co_3S_4 Nanoboxes for High-Rate and Heat-Resistant Lithium–Sulfur Batteries. *J. Am. Chem. Soc.* **2017,** *139*, 12710-12715.

35. He, Y.; Hwang, S.; Cullen, D. A.; Uddin, M. A.; Langhorst, L.; Li, B.; Karakalos, S.; Kropf, A. J.; Wegener, E. C.; Sokolowski, J.; Chen, M.; Myers, D.; Su, D.; More, K. L.; Wang, G.; Litster, S.; Wu, G., Highly Active Atomically Dispersed CoN_4 Fuel Cell Cathode Catalysts

Derived from Surfactant-Assisted MOFs: Carbon-Shell Confinement Strategy. *Energy Environ. Sci.* **2019,** *12*, 250-260.

36. Zhang, M.; Wang, C.; Yan, X.; Kwame, K. P.; Chen, S.; Xiao, C.; Qi, J.; Sun, X.; Wang, L.; Li, J., Metal Organic Framework-Derived Hollow Cactus-like Carbon Sheets for Oxygen Reduction. *J. Mater. Chem. A* **2019,** *7*, 20162-20168.

37. Zhou, Q.; Zhang, Z.; Cai, J.; Liu, B.; Zhang, Y.; Gong, X.; Sui, X.; Yu, A.; Zhao, L.; Wang, Z.; Chen, Z., Template-Guided Synthesis of Co Nanoparticles Embedded in Hollow Nitrogen Doped Carbon Tubes as a Highly Efficient Catalyst for Rechargeable Zn-Air Batteries. *Nano Energy* **2020,** *71*, 104592.

38. Chen, L.; Zhang, Y.; Dong, L.; Yang, W.; Liu, X.; Long, L.; Liu, C.; Dong, S.; Jia, J., Synergistic Effect Between Atomically Dispersed Fe and Co Metal Sites for Enhanced Oxygen Reduction Reaction. *J. Mater. Chem. A* **2020,** *8*, 4369-4375.

39. Zola, A. S.; Ribeiro, R. U.; Bueno, J. M. C.; Zanchet, D.; Arroyo, P. A., Cobalt Nanoparticles Prepared by Three Different Methods. *J. Exp. Nanosci.* **2014,** *9*, 398-405.

40. Ding, Y.; Hu, Y.; Peng, X.; Xiao, Y.; Huang, J., Micro-Nano Structured CoS: An Efficient Catalyst for Peroxymonosulfate Activation for Removal of Bisphenol A. *Sep. Purif. Technol.* **2020,** *233*, 116022.

41. Ta, K.; Zhang, R.; Shin, M.; Rooney, R. T.; Neumann, E. K.; Gewirth, A. A., Understanding Ca Electrodeposition and Speciation Processes in Nonaqueous Electrolytes for Next-Generation Ca-Ion Batteries. *ACS Appl. Mater. Interfaces* **2019,** *11*, 21536-21542.

42. Wang, R.; Yang, J.; Chen, X.; Zhao, Y.; Zhao, W.; Qian, G.; Li, S.; Xiao, Y.; Chen, H.; Ye, Y.; Zhou, G.; Pan, F., Highly Dispersed Cobalt Clusters in Nitrogen-Doped Porous Carbon

Enable Multiple Effects for High-Performance Li–S Battery. *Adv. Energy Mater.* **2020,** *10*, 1903550.

43. Dai, Q.; Tang, J., The Optical and Magnetic Properties of CoO and Co Nanocrystals Prepared by a Facile Technique. *Nanoscale* **2013,** *5*, 7512-7519.

44. Barr, T. L., An ESCA Study of the Termination of the Passivation of Elemental Metals. *J. Phys. Chem.* **1978,** *82*, 1801-1810.

45. Ding, J.; Li, L.; Zheng, H.; Zuo, Y.; Wang, X.; Li, H.; Chen, S.; Zhang, D.; Xu, X.; Li, G., Co_3O_4–$CuCoO_2$ Nanomesh: An Interface-Enhanced Substrate that Simultaneously Promotes CO Adsorption and O_2 Activation in H_2 Purification. *ACS Appli. Mater. Interfaces* **2019,** *11*, 6042-6053.

46. Wang, X. X.; Cullen, D. A.; Pan, Y.-T.; Hwang, S.; Wang, M.; Feng, Z.; Wang, J.; Engelhard, M. H.; Zhang, H.; He, Y.; Shao, Y.; Su, D.; More, K. L.; Spendelow, J. S.; Wu, G., Nitrogen-Coordinated Single Cobalt Atom Catalysts for Oxygen Reduction in Proton Exchange Membrane Fuel Cells. *Adv. Mater.* **2018,** *30*, 1706758.

47. Barreca, D.; Massignan, C.; Daolio, S.; Fabrizio, M.; Piccirillo, C.; Armelao, L.; Tondello, E., Composition and Microstructure of Cobalt Oxide Thin Films Obtained from a Novel Cobalt(II) Precursor by Chemical Vapor Deposition. *Chem. Mater.* **2001,** *13*, 588-593.

48. Younis, A.; Chu, D.; Lin, X.; Lee, J.; Li, S., Bipolar Resistive Switching in P-Type Co_3O_4 Nanosheets Prepared by Electrochemical Deposition. *Nanoscale Res. Lett.* **2013,** *8*, 36-36.

49. Zhang, Z.; Kong, L.-L.; Liu, S.; Li, G.-R.; Gao, X.-P., A High-Efficiency Sulfur/Carbon Composite Based on 3D Graphene Nanosheet@Carbon Nanotube Matrix as Cathode for Lithium–Sulfur Battery. *Adv. Energy Mater.* **2017,** *7*, 1602543.

50. Guan, R.; Zhong, L.; Wang, S.; Han, D.; Xiao, M.; Sun, L.; Meng, Y., Synergetic Covalent and Spatial Confinement of Sulfur Species by Phthalazinone-Containing Covalent Triazine Frameworks for Ultrahigh Performance of Li–S Batteries. *ACS Appl. Mater. Interfaces* **2020,** *12*, 8296-8305.

51. Shao, A. H.; Zhang, Z.; Xiong, D.-G.; Yu, J.; Cai, J.-X.; Yang, Z.-Y., Facile Synthesis of a "Two-in-One" Sulfur Host Featuring Metallic-Cobalt-Embedded N-Doped Carbon Nanotubes for Efficient Lithium-Sulfur Batteries. *ACS Appl. Mater. Interfaces* **2020,** *12*, 5968-5978.

52. Shin, M.; Wu, H.-L.; Narayanan, B.; See, K. A.; Assary, R. S.; Zhu, L.; Haasch, R. T.; Zhang, S.; Zhang, Z.; Curtiss, L. A.; Gewirth, A. A., Effect of the Hydrofluoroether Cosolvent Structure in Acetonitrile-Based Solvate Electrolytes on the Li^+ Solvation Structure and Li–S Battery Performance. *ACS Appl. Mater. Interfaces* **2017,** *9*, 39357-39370.

53. Philip, M. A.; Sullivan, P. T.; Zhang, R.; Wooley, G. A.; Kohn, S. A.; Gewirth, A. A., Improving Cell Resistance and Cycle Life with Solvate-Coated Thiophosphate Solid Electrolytes in Lithium Batteries. *ACS Appl. Mater. Interfaces* **2019,** *11*, 2014-2021.

54. Yu, X.; Manthiram, A., Capacity Enhancement and Discharge Mechanisms of Room-Temperature Sodium–Sulfur Batteries. *ChemElectroChem* **2014,** *1*, 1275-1280.

55. Tu, S.; Zhao, X.; Cheng, M.; Sun, P.; He, Y.; Xu, Y., Uniform Mesoporous MnO_2 Nanospheres as a Surface Chemical Adsorption and Physical Confinement Polysulfide Mediator for Lithium–Sulfur Batteries. *ACS Appl. Mater. Interfaces* **2019,** *11*, 10624-10630.

56. Wang, N.; Wang, Y.; Bai, Z.; Fang, Z.; Zhang, X.; Xu, Z.; Ding, Y.; Xu, X.; Du, Y.; Dou, S.; Yu, G., High-Performance Room-Temperature Sodium–Sulfur Battery Enabled by Electrocatalytic Sodium Polysulfides Full Conversion. *Energy Environ. Sci.* **2020,** *13*, 562-570.

57. Pang, Q.; Nazar, L. F., Long-Life and High-Areal-Capacity Li–S Batteries Enabled by a Light-Weight Polar Host with Intrinsic Polysulfide Adsorption. *ACS Nano* **2016,** *10*, 4111-4118.

58. Kundu, D.; Hosseini Vajargah, S.; Wan, L.; Adams, B.; Prendergast, D.; Nazar, L. F., Aqueous vs. Nonaqueous Zn-Ion Batteries: Consequences of the Desolvation Penalty at the Interface. *Energy Environ. Sci.* **2018,** *11*, 881-892.

59. Zhang, R.; Pan, C.; Nuzzo, R. G.; Gewirth, A. A., CoS_2 as a Sulfur Redox-Active Cathode Material for High-Capacity Nonaqueous Zn Batteries. *J. Phys. Chem. C* **2019,** *123*, 8740-8745.

60. de Jong, A. M.; de Beer, V. H. J.; van Veen, J. A. R.; Niemantsverdriet, J. W., Surface Science Model of a Working Cobalt-Promoted Molybdenum Sulfide Hydrodesulfurization Catalyst: Characterization and Reactivity. *J. Phys. Chem.* **1996,** *100*, 17722-17724.

61. Huo, J.; Wu, J.; Zheng, M.; Tu, Y.; Lan, Z., High Performance Sponge-like Cobalt Sulfide/Reduced Graphene Oxide Hybrid Counter Electrode for Dye-Sensitized Solar Cells. *J. Power Sources* **2015,** *293*, 570-576.

62. Xin, W.; Jiang, W.-J.; Lian, Y.; Li, H.; Hong, S.; Xu, S.; Yan, H.; Hu, J.-S., NiS_2 Nanodotted Carnation-like CoS_2 for Enhanced Electrocatalytic Water Splitting. *Chem. Commun.* **2019,** *55*, 3781-3784.

63. Li, H.-H.; Li, Z.-Y.; Wu, X.-L.; Zhang, L.-L.; Fan, C.-Y.; Wang, H.-F.; Li, X.-Y.; Wang, K.; Sun, H.-Z.; Zhang, J.-P., Shale-like Co_3O_4 for High Performance Lithium/Sodium Ion Batteries. *J. Mater. Chem. A* **2016,** *4*, 8242-8248.

64. Kang, W.; Zhang, Y.; Fan, L.; Zhang, L.; Dai, F.; Wang, R.; Sun, D., Metal–Organic Framework Derived Porous Hollow Co_3O_4/N–C Polyhedron Composite with Excellent Energy Storage Capability. *ACS Appl. Mater. Interfaces* **2017,** *9*, 10602-10609.

65. Takada, K.; Yamada, Y.; Watanabe, E.; Wang, J.; Sodeyama, K.; Tateyama, Y.; Hirata, K.; Kawase, T.; Yamada, A., Unusual Passivation Ability of Superconcentrated Electrolytes toward Hard Carbon Negative Electrodes in Sodium-Ion Batteries. *ACS Appl. Mater. Interfaces* **2017,** *9*, 33802-33809.

66. Patra, J.; Huang, H.-T.; Xue, W.; Wang, C.; Helal, A. S.; Li, J.; Chang, J.-K., Moderately Concentrated Electrolyte Improves Solid–Electrolyte Interphase and Sodium Storage Performance of Hard Carbon. *Energy Storage Mater.* **2019,** *16*, 146-154.

67. Wu, E. A.; Kompella, C. S.; Zhu, Z.; Lee, J. Z.; Lee, S. C.; Chu, I.-H.; Nguyen, H.; Ong, S. P.; Banerjee, A.; Meng, Y. S., New Insights into the Interphase between the Na Metal Anode and Sulfide Solid-State Electrolytes: A Joint Experimental and Computational Study. *ACS Appl. Mater. Interfaces* **2018,** *10*, 10076-10086.

68. Luo, X.; Zhou, Q.; Du, S.; Li, J.; Zhong, J.; Deng, X.; Liu, Y., Porous Co_9S_8/Nitrogen, Sulfur-Doped Carbon@Mo_2C Dual Catalyst for Efficient Water Splitting. *ACS Appl. Mater. Interfaces* **2018,** *10*, 22291-22302.

69. Guo, Q.; Ma, Y.; Chen, T.; Xia, Q.; Yang, M.; Xia, H.; Yu, Y., Cobalt Sulfide Quantum Dot Embedded N/S-Doped Carbon Nanosheets with Superior Reversibility and Rate Capability for Sodium-Ion Batteries. *ACS Nano* **2017,** *11*, 12658-12667.

70. Guo, Y.; Tang, J.; Qian, H.; Wang, Z.; Yamauchi, Y., One-Pot Synthesis of Zeolitic Imidazolate Framework 67-Derived Hollow Co_3S_4@MoS_2 Heterostructures as Efficient Bifunctional Catalysts. *Chem. Mater.* **2017,** *29*, 5566-5573.

71. Fantauzzi, M.; Elsener, B.; Atzei, D.; Rigoldi, A.; Rossi, A., Exploiting XPS for the Identification of Sulfides and Polysulfides. *RSC Adv.* **2015,** *5*, 75953-75963.

72. Sun, X.; Gutierrez, A.; Yacaman, M. J.; Dong, X.; Jin, S., Investigations on Magnetic Properties and Structure for Carbon Encapsulated Nanoparticles of Fe, Co, Ni. *Mater. Sci. Eng. A* **2000,** *286*, 157-160.

73. Matsumoto, Y.; Murakami, M.; Shono, T.; Hasegawa, T.; Fukumura, T.; Kawasaki, M.; Ahmet, P.; Chikyow, T.; Koshihara, S.-y.; Koinuma, H., Room-Temperature Ferromagnetism in Transparent Transition Metal-Doped Titanium Dioxide. *Science* **2001,** *291*, 854-856.

74. Chen, H.; Wang, C.; Dong, W.; Lu, W.; Du, Z.; Chen, L., Monodispersed Sulfur Nanoparticles for Lithium–Sulfur Batteries with Theoretical Performance. *Nano Lett.* **2015,** *15*, 798-802.

75. Jozwiuk, A.; Sommer, H.; Janek, J.; Brezesinski, T., Fair Performance Comparison of Different Carbon Blacks in Lithium–Sulfur Batteries with Practical Mass Loadings – Simple Design Competes with Complex Cathode Architecture. *J. Power Sources* **2015,** *296*, 454-461.

76. Song, Y.; Modrow, H.; Henry, L. L.; Saw, C. K.; Doomes, E. E.; Palshin, V.; Hormes, J.; Kumar, C. S. S. R., Microfluidic Synthesis of Cobalt Nanoparticles. *Chem. Mater.* **2006,** *18*, 2817-2827.

77. Song, A.; Yang, W.; Yang, W.; Sun, G.; Yin, X.; Gao, L.; Wang, Y.; Qin, X.; Shao, G., Facile Synthesis of Cobalt Nanoparticles Entirely Encapsulated in Slim Nitrogen-Doped Carbon Nanotubes as Oxygen Reduction Catalyst. *ACS Sustainable Chem. Eng.* **2017,** *5*, 3973-3981.

78. Jha, A.; Jeong, D.-W.; Lee, Y.-L.; Nah, I. W.; Roh, H.-S., Enhancing the Catalytic Performance of Cobalt Oxide by Doping on Ceria in the High Temperature Water–Gas Shift Reaction. *RSC Adv.* **2015,** *5*, 103023-103029.

79. Hu, L.; Peng, Q.; Li, Y., Selective Synthesis of Co_3O_4 Nanocrystal with Different Shape and Crystal Plane Effect on Catalytic Property for Methane Combustion. *J. Am. Chem. Soc.* **2008,** *130*, 16136-16137.

80. Powell, A. E.; Hodges, J. M.; Schaak, R. E., Preserving Both Anion and Cation Sublattice Features during a Nanocrystal Cation-Exchange Reaction: Synthesis of Metastable Wurtzite-Type CoS and MnS. *J. Am. Chem. Soc.* **2016,** *138*, 471-474.

81. Kale, S. B.; Lokhande, A. C.; Pujari, R. B.; Lokhande, C. D., Cobalt Sulfide Thin Films for Electrocatalytic Oxygen Evolution Reaction and Supercapacitor Applications. *J. Colloid Interf. Sci.* **2018,** *532*, 491-499.

82. Lee, C.; Lee, C.; Shin, K.; Song, T.; Jeong, H. Y.; Jeon, D. Y.; Lee, H. M., Ag_2S-CoS Hetero-Nanowires Terminated with Stepped Surfaces for Improved Oxygen Evolution Reaction. *Catal. Commun.* **2019,** *129*, 105749.

83. Ma, L.; Zhang, W.; Wang, L.; Hu, Y.; Zhu, G.; Wang, Y.; Chen, R.; Chen, T.; Tie, Z.; Liu, J.; Jin, Z., Strong Capillarity, Chemisorption, and Electrocatalytic Capability of Crisscrossed Nanostraws Enabled Flexible, High-Rate, and Long-Cycling Lithium–Sulfur Batteries. *ACS Nano* **2018,** *12*, 4868-4876.

84. Gross, M. M.; Manthiram, A., Rechargeable Zinc-Aqueous Polysulfide Battery with a Mediator-Ion Solid Electrolyte. *ACS Appl. Mater. Interfaces* **2018,** *10*, 10612-10617.

85. Kornienko, N.; Resasco, J.; Becknell, N.; Jiang, C.-M.; Liu, Y.-S.; Nie, K.; Sun, X.; Guo, J.; Leone, S. R.; Yang, P., Operando Spectroscopic Analysis of an Amorphous Cobalt Sulfide Hydrogen Evolution Electrocatalyst. *J. Am. Chem. Soc.* **2015,** *137*, 7448-7455.

86. El Jaroudi, O.; Picquenard, E.; Gobeltz, N.; Demortier, A.; Corset, J., Raman Spectroscopy Study of the Reaction between Sodium Sulfide or Disulfide and Sulfur: Identity of the Species Formed in Solid and Liquid Phases. *Inorg. Chem.* **1999,** *38*, 2917-2923.

87. Kung, C.-W.; Chen, H.-W.; Lin, C.-Y.; Huang, K.-C.; Vittal, R.; Ho, K.-C., CoS Acicular Nanorod Arrays for the Counter Electrode of an Efficient Dye-Sensitized Solar Cell. *ACS Nano* **2012,** *6*, 7016-7025.

88. Das, S.; Sudhagar, P.; Nagarajan, S.; Ito, E.; Lee, S. Y.; Kang, Y. S.; Choi, W., Synthesis of Graphene-CoS Electro-Catalytic Electrodes for Dye Sensitized Solar Cells. *Carbon* **2012,** *50*, 4815-4821.

89. Liang, X.; Kwok, C. Y.; Lodi-Marzano, F.; Pang, Q.; Cuisinier, M.; Huang, H.; Hart, C. J.; Houtarde, D.; Kaup, K.; Sommer, H.; Brezesinski, T.; Janek, J.; Nazar, L. F., Tuning Transition Metal Oxide–Sulfur Interactions for Long Life Lithium Sulfur Batteries: The "Goldilocks" Principle. *Adv. Energy Mater.* **2016,** *6*, 1501636.

90. Lim, W.-G.; Kim, S.; Jo, C.; Lee, J., A Comprehensive Review of Materials with Catalytic Effects in Li–S Batteries: Enhanced Redox Kinetics. *Angewandte Chemie International Edition* **2019,** *58*, 18746-18757.

Chapter 4: CoS_2 as a Sulfur-Redox Active Cathode Material for High Capacity Non-Aqueous Zn Batteries

Reproduced with permission from Zhang, R.; Pan, C.; Nuzzo, R. G.; Gewirth, A. A. CoS_2 as a Sulfur Redox-Active Cathode Material for High-Capacity Nonaqueous Zn Batteries. *J. Phys. Chem. C 2019. 123, 8740−8745.*

4.1 Introduction

The increasing demand for energy storage densities in electric vehicles and portable electronics is making evident the need for a "beyond Li-ion" technology.[1] Multivalent-ion batteries have emerged as promising candidates to this end.[2] These batteries include a multivalent metal anode (e.g., Mg, Zn, and Ca), which possesses a higher inherent volumetric capacity compared to Li-ion batteries (LIBs). Zn exhibits a volumetric capacity of 5851 mAh/mL, which is higher than that of Mg and Ca (3833 mAh/mL and 2073 mAh/mL).[3] In addition, the development of non-aqueous Zn electrolytes allows reversible electrodeposition on a Zn anode and a wide electrochemical window.[4] Zn metal also possesses advantages such as safety and high natural abundance as well as being environmentally benign. In part for these reasons, a high capacity non-aqueous Zn-ion battery would be a prospective alternative to current Li-based energy storage devices.

Several new materials have been reported as cathodes for Zn-ion batteries utilizing a non-aqueous Zn electrolyte. Bilayer V_2O_5 has been reported to have a maximum capacity of 196 mAh/g in $Zn(TFSI)_2$ in acetonitrile.[5] δ-MnO_2 exhibits a capacity of 123 mAh/g in the same

electrolyte.[6] Our group previously reported $ZnAl_xCo_{2-x}O_4$[7] and $ZnNi_xMn_xCo_{2-2x}O_4$[8] spinels with capacities of 134 mAh/g and 180 mAh/g respectively in $Zn(OTf)_2$ in acetonitrile.

As noted above, previous studies on cathode materials for Zn-ion battery have been focusing on metal oxides. Transition metal sulfides, including Chevrel phases,[9,10] Ti_2S_4 spinel,[11] and layered TiS_2,[12] are among the few known cathode materials for use in a Mg-ion battery at room (or slightly elevated) temperature. Unlike oxide cathode materials, in which the Mg^{2+} would exhibit sluggish kinetics, metal sulfides benefit from the weaker coulombic interaction between the multivalent cation and a soft sulfur anion, enhancing ion mobility and facilitating reversible intercalation.[11] In a manner similar to Mg^{2+}, it is likely that suitable metal sulfides could enhance ion mobilities of Zn^{2+} within the lattice.

High capacity can also be associated with anionic redox activity in cathode materials.[13] Traditional cathode materials usually contain cationic redox centers, in which redox reactions take place on transition metal ions. Anionic redox chemistry involves an anionic redox center (e.g. O, S and P) with a smaller atomic mass, thus promising a higher capacity per unit mass. Li-rich layered oxides, including Li_2IrO_3[14] and $Li[Li_{0.2}Ni_{0.2}Mn_{0.6}]O_2$,[15], have been reported to exhibit capacities up to 300 mAh/g in LIBs, with a reversible $2\ O^{2-} \leftrightarrow (O_2)^{n-}$ redox reaction along with conversions of $M^{n+} \leftrightarrow M^{(n+1)+}$. Metal sulfides, such as pyrites (FeS_2 and CoS_2)[16,17,18,19] and patronite (VS_4),[20,21] have been reported to exhibit reversible sulfur redox activity between $S_2^{2-} \leftrightarrow 2\ S^{2-}$ in Li/Na-ion batteries, where a metal-bound disulfide bond $(S\text{-}S)^{2-}$ undergoes breakage and reformation. Given the sluggish kinetics of multivalent cations in oxide lattices, metal sulfides with sulfur anion redox centers suggest themselves as promising candidates for use as cathode materials in high capacity Zn-ion batteries.

Among the anionic redox active metal sulfides, the pyrites (FeS_2 and CoS_2) exhibit both low-cost and high-earth-abundance, which are desirable for mass production. Primary Li/FeS_2 batteries were in fact commercialized in the 1980s.[22] In non-aqueous Li-ion batteries, eqn (1) has been proposed for the first discharge step of pyrites (M = Fe, Co). Further discharge would lead to the conversion reaction forming Li_2S and metal M.[23] The latter conversion reaction, however, leads to drastic capacity

$$MS_2 + 2Li \rightarrow Li_2MS_2 \quad (1)$$

fade due to a redox shuttle consisting of polysulfide species.[17] On the other hand, the first discharge step alone can afford a high capacity of > 400 mAh/g.[24] Hu et al. reported a capacity loss of less than 10% after 20000 cycles when adjusting the cut-off voltage to allow only the reversible intercalation reaction.[25] These findings suggest that pyrite may be a potential high capacity cathode material for multivalent cation storage.

In this work, the cycling performance of CoS_2 (theoretical capacity = 435 mAh/g, crystal structure shown in Figure 4.1) in a non-aqueous Zn electrolyte is investigated. We construct a Zn/CoS_2 cell which exhibits a maximum capacity of 283mAh/g. Studies on valence state, compositional and structural changes reveal for the first time a reversible redox activity of S_2^{2-} which mediates multivalent cation de-/intercalation. These findings show that anionic redox active metal sulfides can achieve high capacities exploitable for use in multivalent cation batteries.

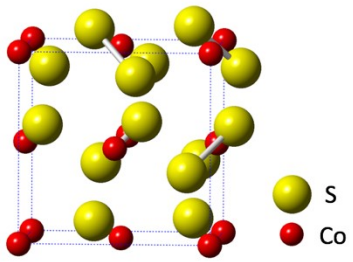

Figure 4.1. Crystal structure of CoS_2.

4.2 Experimental

4.2.1 Cathode Preparation

CoS_2 powder (99.5% pure, Alfa Aesar), Super P Li Carbon (Timcal) and polyvinylidene difluoride (PVDF) were mixed in a weight ratio of 6:3:1 in N-methyl-2-pyrrolidone (NMP). The mixture was sonicated for ~ 1 h, cast onto a current collector (carbon paper, Ion Power Inc., GDL 34 BC) using a doctor blade with a thickness of approximately 25 μm, and dried overnight at room temperature. Then the current collector was further dried in the vacuum oven at 75 ℃ for ~ 2 h, then punched into a 12.7 mm diameter disk before use. The loading of active material on the disk was measured to be 1.0-1.2 mg, which corresponds to 0.8-0.9 mg cm^{-2}.

4.2.2 Coin Cell Assembly

Galvanostatic cycling measurements were carried out in 2032 coin-type cells by using a MTI 8 Channel Battery Analyzer. Zn foil (Sigma-Aldrich, >99.995% pure) was used as the counter/reference electrode. The coin cells were assembled in an Ar-filled glovebox, which contains < 4 ppm of O_2 and < 0.1 ppm of H_2O. A Celgard 2325 membrane was employed as separator. 0.3 M $Zn(OTf)_2$ in acetonitrile (Sigma Aldrich) (electrolyte ~53 ppm H_2O as measured by Karl Fischer titration) was used as electrolyte. 200 ppm 1,4-

Diazabicyclo[2.2.2]octane (DABCO) was added into the electrolyte to prevent acetonitrile polymerization as reported previously.[7] Cyclic voltammetry (CV) measurements were carried out using a CH Instruments electrochemical workstation (Model 620A, Austin, TX).

4.2.3 Characterization

X-ray Photoelectron Spectroscopy (XPS) studies were performed using Kratos Axis ULTRA X-Ray Photoelectron Spectrometer with focused monochromatized Al Kα radiation (1486.8 eV). CasaXPS software was used for peak analysis. To minimize exposure to air and moisture, the cathodes were stored and transferred in Ar. Scanning Electron Microscopy (SEM) imaging was performed using a JEOL JSM-6060LV with an accelerating voltage of 20kV. EDX (Energy-dispersive X-ray spectroscopy) studies were carried out on an Oxford Instruments ISIS EDX attached to the SEM. IXRF analysis software was used to performed quantitative analysis on EDX data. The X-ray Diffraction (XRD) measurements were carried out using a Siemens/Bruker D-5000 instrument with a Cu Kα radiation source, which generates X-rays of energy 8 keV (1.5418 Å). XRD pattern analysis was carried out using Jade 9.0 software. The electrochemical impedance spectroscopy (EIS) was performed on a Biologic potentiostat (Model SP-150, France). The ac perturbation signal was ±10mV and the frequency ranged from 10 mHz to 1 MHz. The analysis of the spectra was carried out using Zview software (Scribner Associates Inc.).

4.3 Results and Discussions

4.3.1 Electrochemical Performance

Figure 4.2a shows the cyclic voltammogram (CV) of CoS_2 in 0.3 M $Zn(OTf)_2$ in acetonitile during the first discharge and the following three cycles, as obtained at a scan rate of 0.5 mV/s. The first discharge exhibits a peak at 0.08 V. An additional peak at 0.65 V appears during discharge in the following cycles, with the peak at lower potential decreased in magnitude. This behavior is consistent with previous reports on the electrochemical cycling of pyrites using either Li or Na. [16,26] The presence of the additional peak at 0.65 V on the second cycle indicates that the recharge process does not follow the reverse path of the first discharge. This change between first and subsequent cycles is consistent with previous studies of Li^+ intercalation in pyrites, where the Li_2MS_2 (M = Co, Fe) produced from Li^+ intercalation during the first discharge forms a new phase, into which a reversible intercalation of Li^+ takes place at a higher potential.[16,17,27,28] Starting from the third cycle, an additional shoulder peak appeared prior to the cathodic peak at lower potential during discharge. The presence of shoulder peak can be attributed to irreversible structural changes, as have been similarly reported for transition metal oxide cathode materials.[29,30]

The charging process exhibits a peak at 1.37 V. The gradual shift of the anodic peak to a more positive voltage upon cycling might be caused by irreversible structural changes due to repeated cycling, which has been observed in the Li/CoS_2 battery.[31]

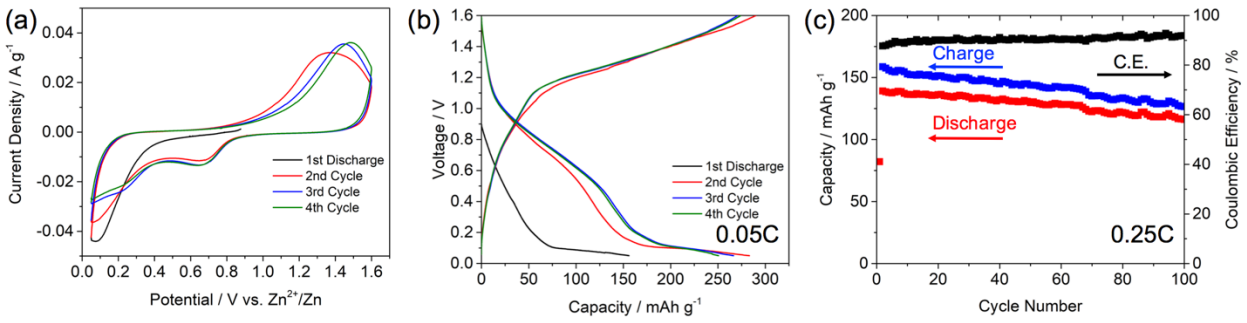

Figure 4.2 (cont.)

Figure 4.2. (a) CV for the first 4 cycles of CoS_2. (b) Charge-discharge curves for the first 4 cycles at a 0.05 C rate. (c) Cycling data for Zn/CoS_2 coin cell operated at a 0.25 C rate.

Figure 4.2b shows the charge-discharge curves of the first discharge and the following three cycles of a Zn/CoS_2 coin cell at a 0.05 C rate. The first discharge exhibits a capacity of 156 mAh/g, with only one plateau at 0.1 V. The second discharge exhibits a capacity of 283 mAh/g, with a new plateau and onset at 1.1 V, which is consistent with the CV. This capacity is 65% of the theoretical capacity, indicating an insufficient utilization of the active material, possibly due to diffusion limitation of Zn^{2+} within the cathode. Controlled experiments were carried out to rule out the possible capacity contribution from carbon.[32] Coin cells with only carbon and PVDF on carbon paper exhibit negligible capacity (Figure 4.3). The cycling data measured at a 0.05 C rate shows a dramatic decrease in discharge capacity as well as Coulombic efficiency (C.E.) after the initial cycles (Figure 4.4). This decrease might be caused by dissolution and/or oxidation of CoS_2 active material during charge causing a shuttle effect.[33] The presence of dissolution is supported by XPS spectra (Figure 4.5), where metallic cobalt and sulfide species are observed on the Zn anode after cycling. The dissolution of active material can be mitigated, however, by increasing the C rate. Figure 4.2c shows the cycling data of a coin cell operated at a 0.25 C rate for 100 cycles. The second cycle exhibits a discharge capacity of 139 mAh/g. The 100th cycle exhibits a discharge capacity of 116 mAh/g, with a C.E. of 92% and a capacity retention of 83%.

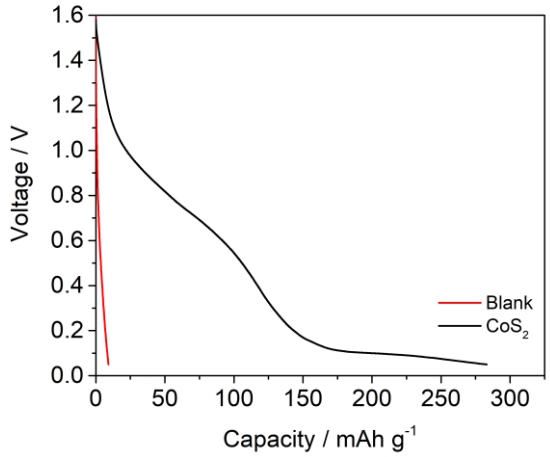

Figure 4.3. Cycling data of blank electrode (carbon and PVDF) and CoS_2.

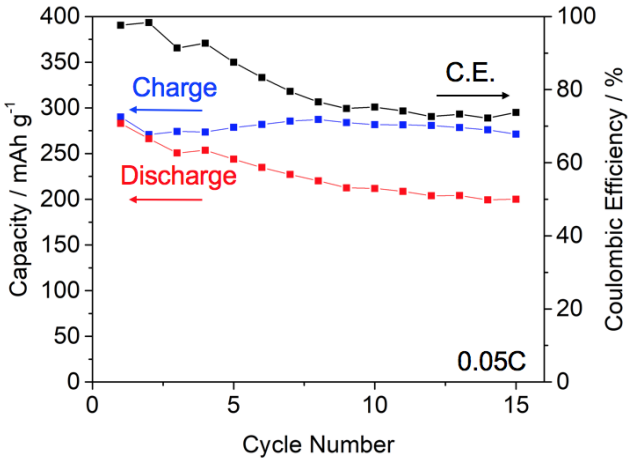

Figure 4.4. Cycling data for Zn/CoS_2 coin cell at a 0.05 C rate. C.E. stabilizes after 10 cycles, and the discharge capacity is 212 mAh/g.

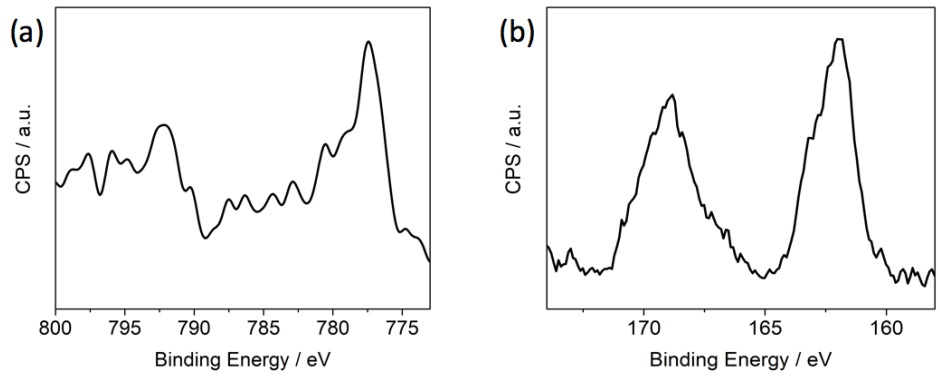

Figure 4.5. XPS spectra for (a) Co 2p and (b) S 2p on Zn anode after 30 cycles. The peaks at 777.9 eV in (a) and 161.9 eV in (b) indicate the presence of metallic Co and S^{2-} species respectively.[25,34,35,36]

4.3.2 Electrochemical Reaction Mechanism

In order to evaluate the reaction mechanism in the Zn/CoS_2 battery, we performed XPS studies on the charged and discharged cathode. Figure 4.6a shows the S 2p spectra obtained from the discharged and charged cathodes, with peak analyses given in *Table 4.1*. From the analyses, the two main peaks at 162.8 eV ($2p_{3/2}$) and 164.0 eV ($2p_{1/2}$) are attributed to the presence of S_2^{2-}, which is consistent with previous studies.[37,38,39] Upon discharge, two peaks at 161.7 eV ($2p_{3/2}$) and 162.9 eV ($2p_{1/2}$) emerge, which indicates the presence of S^{2-} species.[25, 34] These peaks decrease in intensity significantly in the charged sample. This result supports the presence of a reversible sulfur redox: $S_2^{2-} \leftrightarrow 2\ S^{2-}$. The small peaks at 161.7 eV ($2p_{3/2}$) and 162.9 eV ($2p_{1/2}$) in the XPS of the charged sample indicates that a small portion of S^{2-} remains present after charging. The presence of a small amount of S^{2-} is supported by the presence of residual Zn in the EDX of the charged cathode (Figure 4.8f). The peak at 170.3 eV reveals the presence of sulfate species at the surface, possibly arising from the formation of a solid electrolyte interphase (SEI). We note in support of this suggestion that peaks of similar binding energy were observed

in the SEI formed in Li-ion batteries with Lithium bis(trifluoromethanesulfonyl)imide (LiTFSI) and Lithium bis(fluorosulfonyl)imide (LiFSI) in Ethylene Carbonate (EC) as electrolytes.[40]

Figure 4.6b shows the Co 2p spectra obtained from the discharged and charged cathodes. In both samples, the two peaks seen at 778.6 eV ($2p_{3/2}$) and 793.7 eV ($2p_{1/2}$) originate from the Co^{2+} in CoS_2. The two peaks appearing at 780.7 eV and 795.9 eV are satellite peaks. These core level features are consistent with previous studies on pristine CoS_2 materials.[38,39,41,42,43] No evident differences are evidenced in the two spectra, indicating that there is no change in the Co^{2+} valence state during electrochemical cycling. Further XPS study were carried out on samples at different voltage stage in initial and second cycles (Figure 4.7). S 2p spectra is consistent with Figure 4.6a, with the emergence of peaks at 161.8 eV in the discharge states, indicating the reduction of S_2^{2-} to S^{2-}. In the Co 2p spectra, the spectra of the pristine and first discharge samples contain an additional peak at 780.9 eV and 781.7 eV, which can be attributed to satellite peaks of oxidized Co species in the passivation layer on the CoS_2 surface.[37,44] These peaks are absent after first charge, suggesting that the oxidized Co species have been removed from the surface. No evident change is observed on the Co 2p peaks originating from Co^{2+} in CoS_2 among the various voltage states. This lack of oxidation state change in the Co is consistent with previous studies on pyrites in Li/Na-ion batteries, where reversible sulfur redox activity $S_2^{2-} \leftrightarrow 2\ S^{2-}$ mediates Li^+ insertion. [17,28,45]

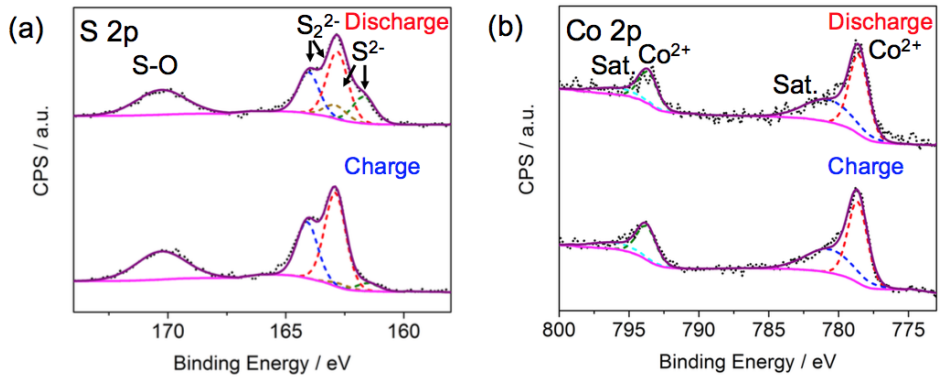

Figure 4.6. XPS spectra for (a) S 2p and (b) Co 2p on CoS_2 cathodes.

Table 4.1. XPS fitting components of S 2p and Co 2p spectra in Figure 4.6.

S 2p	Charge		Discharge		
Pos.	Area%	FWHM	Pos.	Area%	FWHM
162.9±0.1 eV	40.9±0.1	1.05	162.8±0.1 eV	32.2±0.1	1.05
164.1±0.1 eV	24.6±0.1	1.05	164.0±0.1 eV	19.8±0.1	1.05
170.3±0.1 eV	29.0±0.1	2.48	170.3±0.1 eV	27.9±0.1	2.49
161.5±0.1 eV	3.7±0.1	1.10	161.7±0.1 eV	13.4±0.1	1.10
162.7±0.1 eV	1.8±0.1	1.10	162.9±0.1 eV	6.7±0.1	1.10
Co 2p	Charge		Discharge		
Pos.	Area%	FWHM	Pos.	Area%	FWHM
778.6±0.1 eV	43.4±0.1	1.64	778.6±0.1 eV	43.6±0.1	1.60
780.7±0.1 eV	30.5±0.1	4.00	780.7±0.1 eV	30.5±0.1	4.00
793.8±0.1 eV	17.9±0.1	1.64	793.7±0.1 eV	17.3±0.1	1.60
796.0±0.1 eV	8.2±0.1	4.00	795.9±0.1 eV	8.6±0.1	4.00

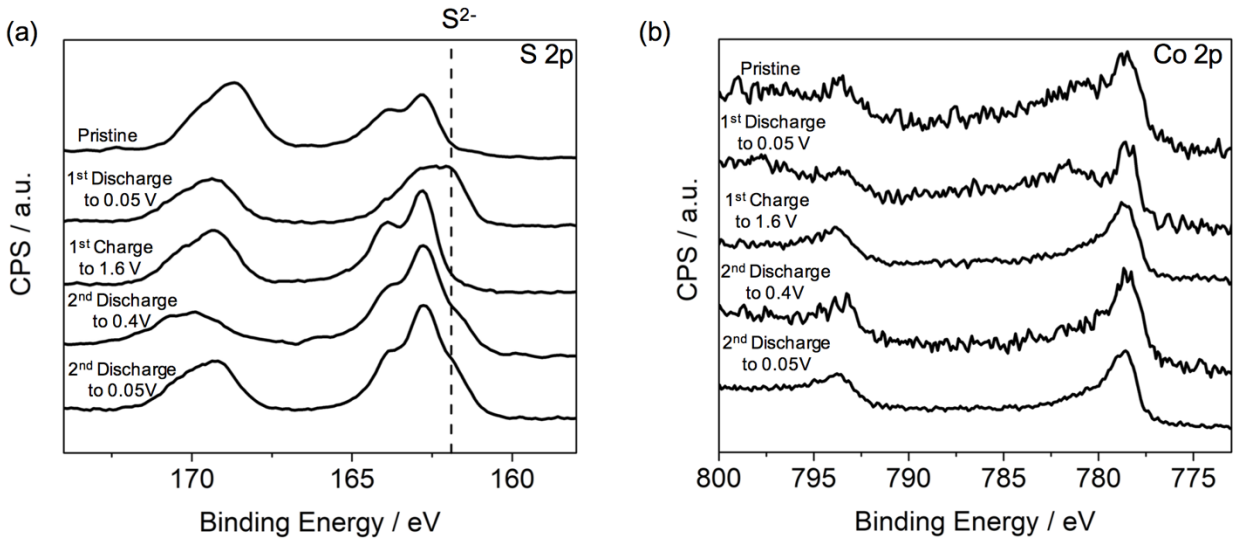

Figure 4.7. XPS spectra for (a) S 2p and (b) Co 2p on CoS_2 cathodes at various voltage states in 1st and 2nd cycles.

SEM and EDX studies are carried out on the pristine (Figure 4.8a and 4.8b), discharged (Figure 4.8c and 4.8d) and charged cathodes (Figure 4.8e and 4.8f). Quantitative analyses of the relative amounts of Zn, Co and S are included in the EDX spectra. No major morphological changes between the three conditions are evident in the SEM images (Figure 4.8a, 4.8c and 4.8e). Figure 4.8b shows that in the pristine cathode, the Co:S ratio is 0.51 : 1.00, in close accordance with the expected value. Upon discharge, an increase in Zn content is observed, wherein the Zn:Co:S ratios are 0.23 : 0.49 : 1.00 (Figure 4.8d). The corresponding ratio in the charged sample (Figure 4.8f) is 0.04 : 0.51 : 1.00. EDX mapping indicates that the Zn content is evenly distributed in the electrode material (Figure 4.9). The difference in Zn:S ratio corresponds to a discharge capacity of 165 mAh/g. This capacity is lower than the experimentally (coin cell)

derived capacity (212 mAh/g, as shown in Figure 4.4), which indicates that the redox mediated Zn^{2+} insertion is not the only process contributing to the high capacity.

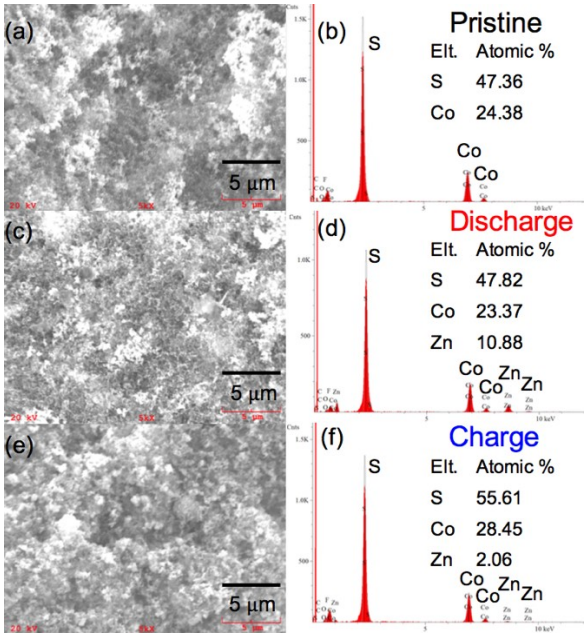

Figure 4.8. SEM and EDX for pristine (a, b), discharge (c, d) and charge (e, f) cathodes. The atomic percentage of Zn, Co and S are inserted.

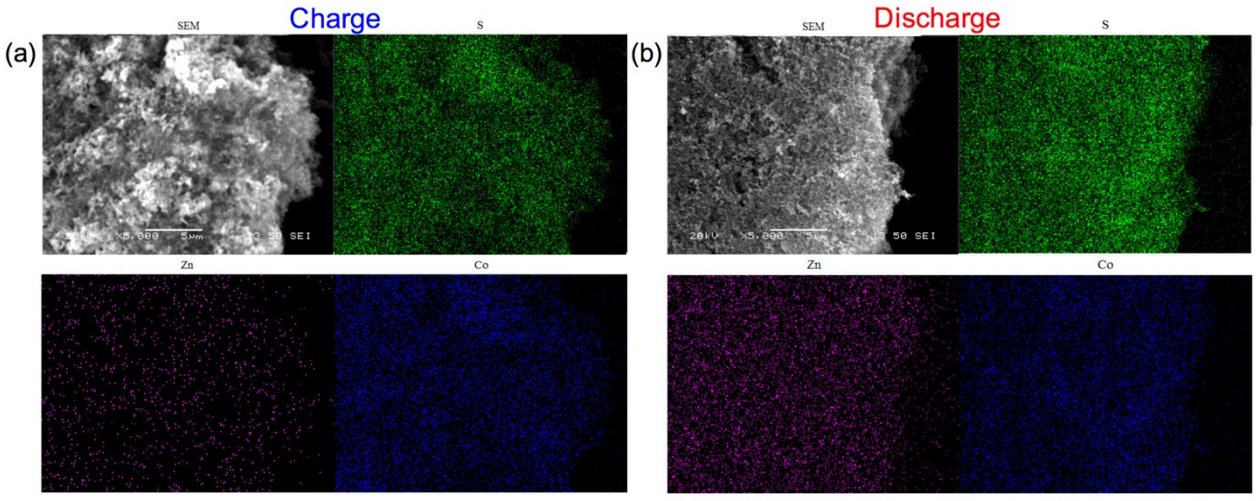

Figure 4.9. EDX mapping of (a) charge and (b) discharge cathodes.

To look into the relative contributions of Faradaic and capacitive processes to the total capacity, we used cyclic voltammetry following a method that has been previously reported for studies of pyrites in Li/Na-ion battery chemistries (Figure 4.10).[46,47,48,49] From this analysis, the ratio between capacities coming from capacitive and Faradaic processes was determined to be 0.23 : 1. The total capacity is therefore found to be 203 mAh/g, of which 165 mAh/g is Faradaic in nature and 38 mAh/g is capacitive. This capacity matches well with the value derived experimentally.

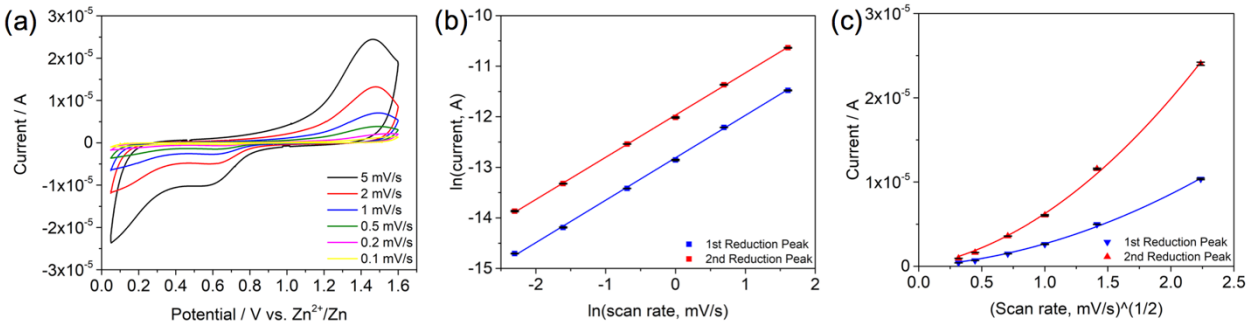

Figure 4.10. (a) CV of CoS_2 at various scan rates. (b) Fitted lines for ln(i) and ln(v), where i represents the peak current for the two reduction peaks, and v represents scan rate. The slope of the line is the b-value, which yield information on the degree of contribution of capacitance to the current. Since current produced from redox mediated intercalation follows $k_1 v^{\frac{1}{2}}$ while that from capacitance follows $k_2 v$, a b-value close to 0.5 would indicate a Faradaic process, while a b-value much greater than 0.5 would indicate a significant contribution from capacitance. The b-values for the first and second peaks are ~0.8. This means that the capacitance contribution cannot be omitted. (c) Fitted curves for current and (scan rate)^(1/2) of the two reduction peaks. With contribution from both redox mediated intercalation and capacitive effect, the total current is a combination of the two, where $i = k_1 v^{\frac{1}{2}} + k_2 v$. The two formulas derived from the fitting

Figure 4.10. for the first and second peaks are $i = (1.1 \pm 0.2) \times 10^{-6} v^{\frac{1}{2}} + (1.6 \pm 0.1) \times 10^{-6} v$ and $i = (2.6 \pm 0.4) \times 10^{-6} v^{\frac{1}{2}} + (3.7 \pm 0.2) \times 10^{-6} v$ respectively.

XRD studies were carried out to examine the structural evolution of the material during cycling. The *ex situ* XRD patterns of pristine, discharged, and charged cathodes are shown in Figure 4.11, with peaks related to CoS_2 labelled with their corresponding Miller indices. Upon discharge, these CoS_2-related peaks decrease in intensity, with new peaks emerging at 32.8° and 58.7°. After charging, the peaks for CoS_2 partially regain their intensity, while the new peaks found in the discharged state decreasing in intensity. No peak shifts are observed. The decrease in peak intensity seen upon discharge, and the partial regain of this peak intensity upon recharge, is consistent with the findings of previous reports on pyrites used in Li/Na-ion battery chemistries. Here, an irreversible change in the pyrite structure takes place during the first discharge process, producing a new phase Li_2MS_2/Na_2MS_2 (M = Co, Fe), which facilitates reversible Li^+ and Na^+ intercalation at a higher potential.[17,18,28] The new peaks emerging after discharge in Fig. 4.11 can be attributed to a new phase produced from Zn^{2+} intercalation into the active material. However, due to the limited number of peaks, possibly caused by poor crystallinity in the new phase[50], we cannot assign an explicit phase to the peaks with certainty. We do note that similar peaks in XRD spectra have been reported in Na/FeS_2 systems, which were assigned to a Na_xFeS_2 phase.[25,50] Li_xTiS_2 ($0 \leq x \leq 3$) has also been reported to exhibit similar diffraction peaks.[51] Taken together, the data suggest that new phase produced might be a Zn_xCoS_2 phase, in which reversible Zn^{2+} intercalation can take place. The XRD results, together with the data coming from valence state and compositional studies, supports a reversible S_2^{2-}/S^{2-} redox-mediated intercalation of Zn^{2+} into CoS_2, with a new phase formed irreversibly. The latter

allows the reversible Zn^{2+} intercalation seen at a higher potential in subsequent cycles, mediated by S_2^{2-}/S^{2-} redox as well. Taken together, these findings suggest that CoS_2 is an anionic redox active cathode material potentially suitable for use in non-aqueous Zn batteries. Furthermore, various studies have reported on the synthesis of desired architecture for CoS_2, which mitigates its dissolution in electrolytes, promising improved cycling at low C-rate.[52,53,54]

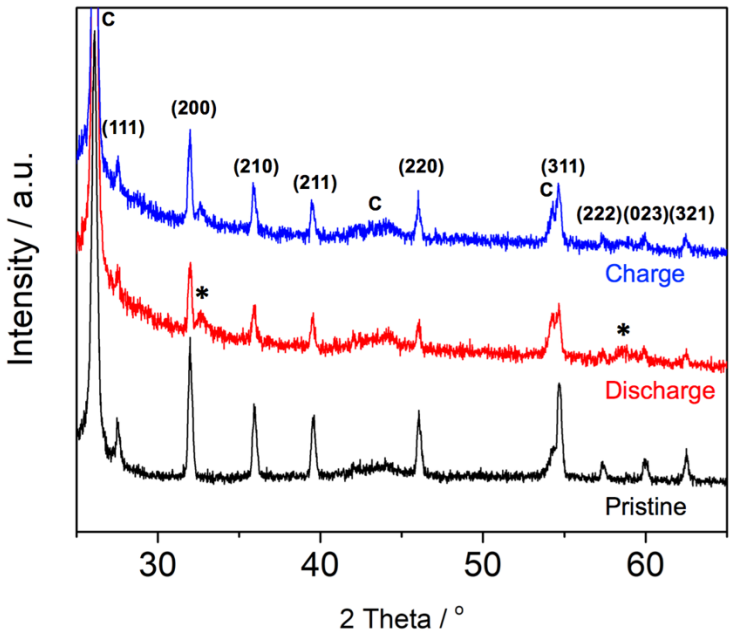

Figure 4.11. Ex-situ XRD patterns for pristine, discharge and charge cathodes. The new peaks emerged upon discharge are labelled in *.

We performed EIS studies to study the evolution of cell performance with cycling. Figure 4.12a shows the Nyquist plots of the cell at selected cycles. The capacitive behavior suggested by the tendency towards a vertical line in the very low frequency region in the Nyquist plots agrees with our scan rate study on the capacitance contribution, and is also consistent with previous studies on pyrites in Li and Na systems.[25,55] The analyses of the Nyquist plots were carried out by using Zview software with the equivalent circuit shown in Figure 4.12b. The

adoption of this equivalent circuit follows metrics established in previous studies on electrode materials with capacitive behavior.[56,57] The fitted EIS analyses of cycles 2 and cycle 50 are included in Figure 4.13. Cycle 2 exhibits a minimum charge transfer resistance R_{ct} of 230 Ω, which can be attributed to the electrochemical polishing of the passivation layers on the Zn metal[5,58] and CoS_2, as observed in the XPS spectra of the pristine and first discharge cathodes (Figure 4.7), during the first charge. A passivation layer resistance R_{pl} of 25 Ω is found, which might be due to the formation of SEI. After cycle 2, the semicircles in the high to medium frequency ranges in Nyquist plots enlarge, indicating an increase in R_{ct}. The measured value of R_{ct} is stable after 40 cycles. At cycle 50, the R_{ct} and R_{pl} are 493 Ω and 24 Ω respectively. The increase seen in R_{ct} may be due to the formation of a passivation layer containing cobalt and sulfide species on the Zn anode after repeated cycling, a suggestion consistent with core level data measured in XPS spectra of the cycled Zn anode (Figure 4.5).

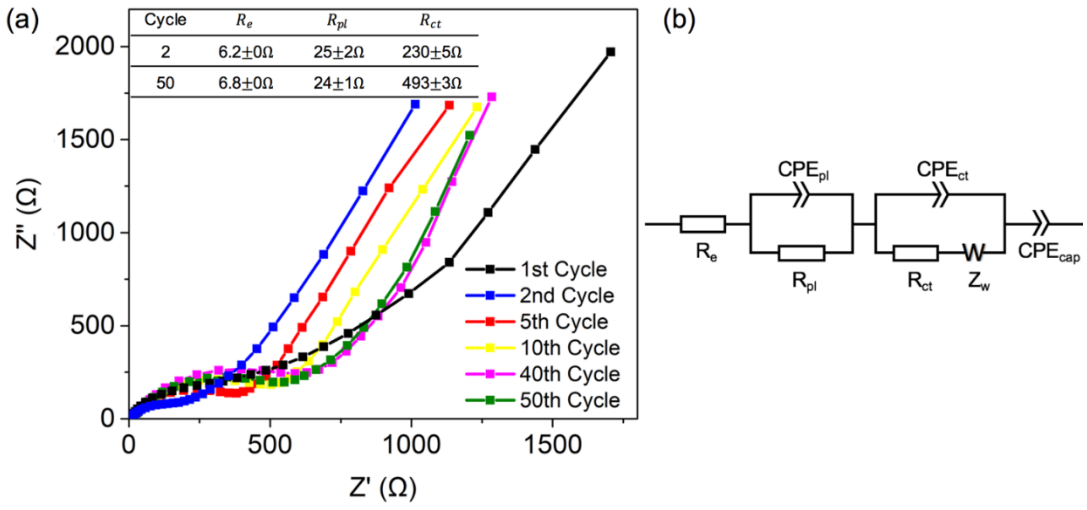

Figure 4.12. (a) Electrochemical impedance spectra of Zn/CoS_2 coin cell at selected cycles and (b) the corresponding equivalent circuit.

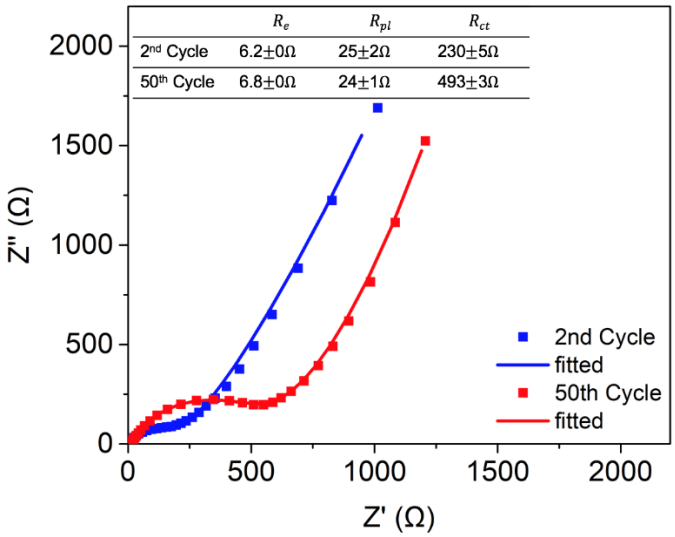

Figure 4.13. Fitted impedance spectra for the 2nd cycle and the 50th cycle based on equivalent circuit in Figure 4.12b.

4.4 Conclusions

In conclusion, we provide data demonstrating a reversible non-aqueous Zn-ion insertion into CoS_2 cathode system, yielding a Zn/CoS_2 non-aqueous battery exhibiting a maximum capacity of 283 mAh/g. Valence state, compositional and structural studies support anionic redox activity associated with S_2^{2-}, activities directly mediating reversible Zn-ion intercalation. This is the first instance of such mediation found to be active in a multivalent system. These findings suggest that anionic redox active metal sulfides are potential candidates for use in high capacity multivalent batteries.

4.5 References

1. Whittingham, M. S., Ultimate Limits to Intercalation Reactions for Lithium Batteries. *Chem. Rev.* **2014,** *114*, 11414-11443.

2. Choi, N.-S.; Chen, Z.; Freunberger, S. A.; Ji, X.; Sun, Y.-K.; Amine, K.; Yushin, G.; Nazar, L. F.; Cho, J.; Bruce, P. G., Challenges Facing Lithium Batteries and Electrical Double-Layer Capacitors. *Ange. Chem. Int. Ed.* **2012,** *51*, 9994-10024.

3. Muldoon, J.; Bucur, C. B.; Gregory, T., Quest for Nonaqueous Multivalent Secondary Batteries: Magnesium and Beyond. *Chem. Rev.* **2014,** *114*, 11683-11720.

4. Han, S.-D.; Rajput, N. N.; Qu, X.; Pan, B.; He, M.; Ferrandon, M. S.; Liao, C.; Persson, K. A.; Burrell, A. K., Origin of Electrochemical, Structural, and Transport Properties in Nonaqueous Zinc Electrolytes. *ACS Appl. Mater. Interfaces* **2016,** *8*, 3021-3031.

5. Senguttuvan, P.; Han, S.-D.; Kim, S.; Lipson, A. L.; Tepavcevic, S.; Fister, T. T.; Bloom, I. D.; Burrell, A. K.; Johnson, C. S., A High Power Rechargeable Nonaqueous Multivalent Zn/V_2O_5 Battery. *Adv. Energy Mater.* **2016,** *6*, 1600826.

6. Han, S.-D.; Kim, S.; Li, D.; Petkov, V.; Yoo, H. D.; Phillips, P. J.; Wang, H.; Kim, J. J.; More, K. L.; Key, B.; Klie, R. F.; Cabana, J.; Stamenkovic, V. R.; Fister, T. T.; Markovic, N. M.; Burrell, A. K.; Tepavcevic, S.; Vaughey, J. T., Mechanism of Zn Insertion into Nanostructured δ-MnO_2: A Nonaqueous Rechargeable Zn Metal Battery. *Chem. Mater.* **2017,** *29*, 4874-4884.

7. Pan, C.; Nuzzo, R. G.; Gewirth, A. A., $ZnAl_xCo_{2-x}O_4$ Spinels as Cathode Materials for Non-Aqueous Zn Batteries with an Open Circuit Voltage of ≤2 V. *Chem. Mater.* **2017,** *29*, 9351-9359.

8. Pan, C.; Zhang, R.; Nuzzo, R. G.; Gewirth, A. A., $ZnNi_xMn_xCo_{2-2x}O_4$ Spinel as a High-Voltage and High-Capacity Cathode Material for Nonaqueous Zn-Ion Batteries. *Adv. Energy Mater.* **2018**, 1800589.

9. Aurbach, D.; Lu, Z.; Schechter, A.; Gofer, Y.; Gizbar, H.; Turgeman, R.; Cohen, Y.; Moshkovich, M.; Levi, E., Prototype Systems for Rechargeable Magnesium Batteries. *Nature* **2000,** *407*, 724-727.

10. Levi, E.; Gofer, Y.; Vestfreed, Y.; Lancry, E.; Aurbach, D., $Cu_2Mo_6S_8$ Chevrel Phase, A Promising Cathode Material for New Rechargeable Mg Batteries: A Mechanically Induced Chemical Reaction. *Chem. Mater.* **2002,** *14*, 2767-2773.

11. Sun, X.; Bonnick, P.; Duffort, V.; Liu, M.; Rong, Z.; Persson, K. A.; Ceder, G.; Nazar, L. F., A High Capacity Thiospinel Cathode for Mg Batteries. *Energy Environ. Sci.* **2016,** *9*, 2273-2277.

12. Sun, X.; Bonnick, P.; Nazar, L. F., Layered TiS_2 Positive Electrode for Mg Batteries. *ACS Energy Lett.* **2016,** *1*, 297-301.

13. Li, B.; Xia, D., Anionic Redox in Rechargeable Lithium Batteries. *Adv. Mater.* **2017,** *29*, 1701054.

14. Pearce, P. E.; Perez, A. J.; Rousse, G.; Saubanère, M.; Batuk, D.; Foix, D.; McCalla, E.; Abakumov, A. M.; Van Tendeloo, G.; Doublet, M.-L.; Tarascon, J.-M., Evidence for Anionic Redox Activity in a Tridimensional-Ordered Li-Rich Positive Electrode β-Li_2IrO_3. *Nat. Mater.* **2017,** *16*, 580-586.

15. Luo, K.; Roberts, M. R.; Guerrini, N.; Tapia-Ruiz, N.; Hao, R.; Massel, F.; Pickup, D. M.; Ramos, S.; Liu, Y.-S.; Guo, J.; Chadwick, A. V.; Duda, L. C.; Bruce, P. G., Anion Redox Chemistry in the Cobalt Free 3d Transition Metal Oxide Intercalation Electrode $Li[Li_{0.2}Ni_{0.2}Mn_{0.6}]O_2$. *J. Am. Chem. Soc.* **2016,** *138*, 11211-11218.

16. Zhang, S. S.; Tran, D. T., Electrochemical Verification of the Redox Mechanism of FeS_2 in a Rechargeable Lithium Battery. *Electrochi. Acta* **2015,** *176*, 784-789.

17. Zhang, S. S., The Redox Mechanism of FeS_2 in Non-Aqueous Electrolytes for Lithium and Sodium Batteries. *J. Mater. Chem. A* **2015,** *3*, 7689-7694.

18. Yan, J. M.; Huang, H. Z.; Zhang, J.; Liu, Z. J.; Yang, Y., A Study of Novel Anode Material CoS_2 for Lithium Ion Battery. *J. Power Sources* **2005,** *146*, 264-269.

19. Xie, J.; Liu, S.; Cao, G.; Zhu, T.; Zhao, X., Self-Assembly of CoS_2/Graphene Nanoarchitecture by a Facile One-Pot Route and its Improved Electrochemical Li-Storage Properties. *Nano Energy* **2013,** *2*, 49-56.

20. Rout, C. S.; Kim, B.-H.; Xu, X.; Yang, J.; Jeong, H. Y.; Odkhuu, D.; Park, N.; Cho, J.; Shin, H. S., Synthesis and Characterization of Patronite Form of Vanadium Sulfide on Graphitic Layer. *J. Am. Chem. Soc.* **2013,** *135*, 8720-8725.

21. Britto, S.; Leskes, M.; Hua, X.; Hébert, C.-A.; Shin, H. S.; Clarke, S.; Borkiewicz, O.; Chapman, K. W.; Seshadri, R.; Cho, J.; Grey, C. P., Multiple Redox Modes in the Reversible Lithiation of High-Capacity, Peierls-Distorted Vanadium Sulfide. *J. Am. Chem. Soc.* **2015,** *137*, 8499-8508.

22. Linden, D.; Reddy, T. B., *Handbook of Batteries*. 3rd ed.; McGraw-Hill: 2002.

23. Butala, M. M.; Doan-Nguyen, V. V. T.; Lehner, A. J.; Göbel, C.; Lumley, M. A.; Arnon, S.; Wiaderek, K. M.; Borkiewicz, O. J.; Chapman, K. W.; Chupas, P. J.; Balasubramanian, M.; Seshadri, R., Operando Studies Reveal Structural Evolution with Electrochemical Cycling in Li–CoS_2. *J. Phys. Chem. C* **2018,** *122*, 24559-24569.

24. Fong, R.; Dahn, J. R.; Jones, C. H. W., Electrochemistry of Pyrite-Based Cathodes for Ambient Temperature Lithium Batteries. *J. Electrochem. Soc.* **1989,** *136*, 3206-3210.

25. Hu, Z.; Zhu, Z.; Cheng, F.; Zhang, K.; Wang, J.; Chen, C.; Chen, J., Pyrite FeS_2 for High-Rate and Long-Life Rechargeable Sodium Batteries. *Energy Environ. Sci.* **2015,** *8*, 1309-1316.

26. Liu, X.; Zhang, K.; Lei, K.; Li, F.; Tao, Z.; Chen, J., Facile Synthesis and Electrochemical Sodium Storage of CoS_2 Micro/Nano-Structures. *Nano Res.* **2016,** *9*, 198-206.

27. Butala, M. M.; Mayo, M.; Doan-Nguyen, V. V. T.; Lumley, M. A.; Göbel, C.; Wiaderek, K. M.; Borkiewicz, O. J.; Chapman, K. W.; Chupas, P. J.; Balasubramanian, M.; Laurita, G.; Britto, S.; Morris, A. J.; Grey, C. P.; Seshadri, R., Local Structure Evolution and Modes of Charge Storage in Secondary Li–FeS_2 Cells. *Chem. Mater.* **2017,** *29*, 3070-3082.

28. Kitajou, A.; Yamaguchi, J.; Hara, S.; Okada, S., Discharge/Charge Reaction Mechanism of a Pyrite-Type FeS_2 Cathode for Sodium Secondary Batteries. *J. Power Sources* **2014,** *247*, 391-395.

29. Yu, H.; Rui, X.; Tan, H.; Chen, J.; Huang, X.; Xu, C.; Liu, W.; Yu, D. Y. W.; Hng, H. H.; Hoster, H. E.; Yan, Q., Cu Doped V_2O_5 Flowers as Cathode Material for High-Performance Lithium Ion Batteries. *Nanoscale* **2013,** *5*, 4937-4943.

30. Przesniak-Welenc, M.; Karczewski, J.; Smalc-Koziorowska, J.; Lapinski, M.; Sadowski, W.; Koscielska, B., The Influence of Nanostructure Size on V_2O_5 Electrochemical Properties as Cathode Materials for Lithium Ion Batteries. *RSC Adv.* **2016,** *6*, 55689-55697.

31. Zhou, Y.; Yan, D.; Xu, H.; Feng, J.; Jiang, X.; Yue, J.; Yang, J.; Qian, Y., Hollow Nanospheres of Mesoporous Co_9S_8 as a High-Capacity and Long-Life Anode for Advanced Lithium Ion Batteries. *Nano Energy* **2015,** *12*, 528-537.

32. Dong, L.; Ma, X.; Li, Y.; Zhao, L.; Liu, W.; Cheng, J.; Xu, C.; Li, B.; Yang, Q.-H.; Kang, F., Extremely Safe, High-Rate and Ultralong-Life Zinc-Ion Hybrid Supercapacitors. *Energy Storage Materials* **2018,** *13*, 96-102.

33. Qi, S.; Mi, L.; Song, K.; Yang, K.; Ma, J.; Feng, X.; Zhang, J.; Chen, W., Understanding Shuttling Effect in Sodium Ion Batteries for the Solution of Capacity Fading: FeS_2 as an Example. *J. Phys. Chem. C* **2019,** *123*, 2775-2782.

34. Deroubaix, G.; Marcus, P., X-Ray Photoelectron Spectroscopy Analysis of Copper and Zinc Oxides and Sulphides. *Surf. Interface Anal.* **1992,** *18*, 39-46.

35. Li, J.; Zhu, Q.-L.; Xu, Q., Highly Active AuCo Alloy Nanoparticles Encapsulated in the Pores of Metal-Organic Frameworks for Hydrolytic Dehydrogenation of Ammonia Borane. *Chem. Commun.* **2014,** *50*, 5899-5901.

36. Zhai, M.; Wang, F.; Du, H., Transition-Metal Phosphide–Carbon Nanosheet Composites Derived from Two-Dimensional Metal-Organic Frameworks for Highly Efficient Electrocatalytic Water-Splitting. *ACS Appl. Mater. & Interfaces* **2017,** *9*, 40171-40179.

37. Faber, M. S.; Dziedzic, R.; Lukowski, M. A.; Kaiser, N. S.; Ding, Q.; Jin, S., High-Performance Electrocatalysis Using Metallic Cobalt Pyrite (CoS_2) Micro- and Nanostructures. *J. Am. Chem. Soc.* **2014,** *136*, 10053-10061.

38. Zou, K.-Y.; Liu, Y.-C.; Jiang, Y.-F.; Yu, C.-Y.; Yue, M.-L.; Li, Z.-X., Benzoate Acid-Dependent Lattice Dimension of Co-MOFs and MOF-Derived CoS_2@CNTs with Tunable Pore Diameters for Supercapacitors. *Inorg. Chem.* **2017,** *56*, 6184-6196.

39. Fang, L.; Zhang, Y.; Guan, Y.; Zhang, H.; Wang, S.; Wang, Y., Specific Synthesis of CoS_2 Nanoparticles Embedded in Porous Al_2O_3 Nanosheets for Efficient Hydrogen Evolution and Enhanced Lithium Storage. *J. Mater. Chem. A* **2017,** *5*, 2861-2869.

40. Nie, M.; Lucht, B. L., Role of Lithium Salt on Solid Electrolyte Interface (SEI) Formation and Structure in Lithium Ion Batteries. *J. Electrochem. Soc.* **2014,** *161*, A1001-A1006.

41. Zhou, X.; Yang, X.; Li, H.; Hedhili, M. N.; Huang, K.-W.; Li, L.-J.; Zhang, W., Symmetric Synergy of Hybrid CoS_2-WS_2 Electrocatalysts for the Hydrogen Evolution Reaction. *J. Mater. Chem. A* **2017,** *5*, 15552-15558.

42. Gu, H.; Huang, Y.; Zuo, L.; Fan, W.; Liu, T., Electrospun Carbon Nanofiber@CoS_2 Core/Sheath Hybrid as an Efficient all-pH Hydrogen Evolution Electrocatalyst. *Inorg Chem. Front.* **2016,** *3*, 1280-1288.

43. Ji, Y.; Liu, X.; Liu, W.; Wang, Y.; Zhang, H.; Yang, M.; Wang, X.; Zhao, X.; Feng, S., A Facile Template-Free Approach for the Solid-Phase Synthesis of CoS_2 Nanocrystals and Their Enhanced Storage Energy in Supercapacitors. *RSC Adv.* **2014,** *4*, 50220-50225.

44. Chang, J.; Ouyang, Y.; Ge, J.; Wang, J.; Liu, C.; Xing, W., Cobalt Phosphosulfide in the Tetragonal Phase: A Highly Active and Durable Catalyst for the Hydrogen Evolution Reaction. *J. Mater. Chem. A* **2018,** *6*, 12353-12360.

45. Totir, D. A.; Bae, I. T.; Hu, Y.; Antonio, M. R.; Stan, M. A.; Scherson, D. A., In Situ Fe K-Edge X-ray Absorption Fine Structure of a Pyrite Electrode in a Li/Polyethylene Oxide($LiClO_4$)/FeS_2 Battery Environment. *J. Phys. Chem. B* **1997,** *101*, 9751-9756.

46. Yu, P.; Li, C.; Guo, X., Sodium Storage and Pseudocapacitive Charge in Textured $Li_4Ti_5O_{12}$ Thin Films. *J. Phys. Chem. C* **2014,** *118*, 10616-10624.

47. Kumar, V.; Lee, P. S., Redox Active Polyaniline-h-MoO_3 Hollow Nanorods for Improved Pseudocapacitive Performance. *J. Phys. Chem. C* **2015,** *119*, 9041-9049.

48. Deng, F.; Li, X.; Ding, F.; Niu, B.; Li, J., Pseudocapacitive Energy Storage in Schiff Base Polymer with Salphen-Type Ligands. *J. Phys. Chem. C* **2018,** *122*, 5325-5333.

49. Harilal, M.; Krishnan, S. G.; Yar, A.; Misnon, I. I.; Reddy, M. V.; Yusoff, M. M.; Ojur Dennis, J.; Jose, R., Pseudocapacitive Charge Storage in Single-Step-Synthesized CoO–MnO_2–

$MnCo_2O_4$ Hybrid Nanowires in Aqueous Alkaline Electrolytes. *J. Phys. Chem. C* **2017,** *121*, 21171-21183.

50. Shadike, Z.; Zhou, Y.-N.; Ding, F.; Sang, L.; Nam, K.-W.; Yang, X.-Q.; Fu, Z.-W., The New Electrochemical Reaction Mechanism of Na/FeS_2 Cell at Ambient Temperature. *J. Power Sources* **2014,** *260*, 72-76.

51. Suslov, E. A.; Bushkova, O. V.; Sherstobitova, E. A.; Reznitskikh, O. G.; Titov, A. N., Lithium Intercalation into TiS_2 Cathode Material: Phase Equilibria in a Li–TiS_2 System. *Ionics* **2016,** *22*, 503-514.

52. Wang, Q.; Jiao, L.; Han, Y.; Du, H.; Peng, W.; Huan, Q.; Song, D.; Si, Y.; Wang, Y.; Yuan, H., CoS_2 Hollow Spheres: Fabrication and Their Application in Lithium-Ion Batteries. *J. Phys. Chem. C* **2011,** *115*, 8300-8304.

53. Kinner, T.; Bhandari, K. P.; Bastola, E.; Monahan, B. M.; Haugen, N. O.; Roland, P. J.; Bigioni, T. P.; Ellingson, R. J., Majority Carrier Type Control of Cobalt Iron Sulfide ($Co_xFe_{1-x}S_2$) Pyrite Nanocrystals. *J. Phys. Chem. C* **2016,** *120*, 5706-5713.

54. Tong, Y.; Yu, X.; Shi, G., Cobalt Disulfide/Graphite Foam Composite Films as Self-Standing Electrocatalytic Electrodes for Overall Water Splitting. *Phys. Chem. Chem. Phys.* **2017,** *19*, 4821-4826.

55. Xu, X.; Liu, J.; Liu, Z.; Shen, J.; Hu, R.; Liu, J.; Ouyang, L.; Zhang, L.; Zhu, M., Robust Pitaya-Structured Pyrite as High Energy Density Cathode for High-Rate Lithium Batteries. *ACS Nano* **2017,** *11*, 9033-9040.

56. Ning, X.; Wang, X.; Yu, X.; Zhao, J.; Wang, M.; Li, H.; Yang, Y., Outstanding Supercapacitive Properties of Mn-Doped TiO_2 Micro/Nanostructure Porous Film Prepared by Anodization Method. *Sci. Rep.* **2016,** *6*, 22634.

57. Park, H. W.; Na, B.-K.; Cho, B. W.; Park, S.-M.; Roh, K. C., Influence of Vanadium Doping on the Electrochemical Performance of Nickel Oxide in Supercapacitors. *Phys. Chem. Chem. Phys.* **2013,** *15*, 17626-17635.

58. Kundu, D.; Hosseini Vajargah, S.; Wan, L.; Adams, B.; Prendergast, D.; Nazar, L. F., Aqueous vs. Nonaqueous Zn-Ion Batteries: Consequences of the Desolvation Penalty at the Interface. *Energy Environ. Sci.* **2018,** *11*, 881-892.

Appendix A: Notes for Attenuated Total Reflectance Surface Enhanced Infrared Absorption Spectroscopy

A.1 Spectroelectrochemical Cell Design

The spectroelectrochemical cell for attenuated total reflectance surface enhanced infrared absorption spectroscopy (ATR-SEIRAS) was built in physics-MRL machine shop under project title 'SEIRAS CELL'. The spectrochemical cell was designed based on previous studies.[1] The detailed components of the cell are shown in Figure A.1a. The working electrode is the thin metal film evaporated onto a prism. An o-ring is pressed onto the metal film surface to seal the cell and prevent leakage of the electrolyte. A Au wire is placed outside the o-ring and also pressed onto the metal film surface to make the electrical contact for the metal film working electrode. The counter electrode and reference electrode are placed into the electrolyte through Flangeless fittings from the wall of the cell. The Flangeless fitting contains a Flangeless nut, a tubing, and a Flangeless ferrule. The metal wires/electrodes are fed through the tubing, and the diameter of the wires should be the same as the inner diameter of the tubing. This setup is crucial for the seal of the cell to prevent electrolyte leakage. The image of the cell placed on an attenuated total reflectance (ATR) accessory is shown in Figure A.1b.

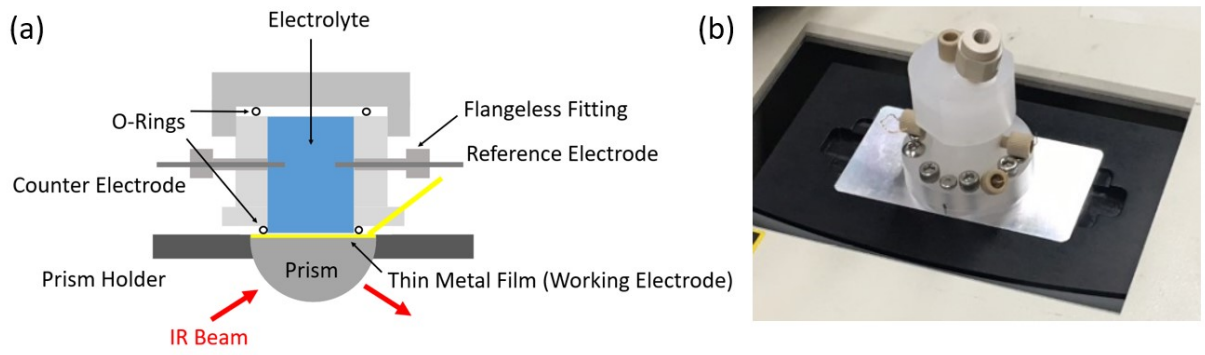

Figure A.1 (cont.)

(a) Components of the spectroelectrochemical cell for ATR-SEIRAS. (b) Image of the spectroelectrochemical cell for ATR-SEIRAS on an ATR accessory.

A.2 Preparation for SEIRAS Measurements

The thin metal film is deposited onto the prism through electron beam physical vapor deposition. In this study, the deposition process is carried out using E-beam 4 at MRL. 20 nm of Au is deposited onto a Si wafer (the prism) at a rate of 0.01 nm/s. The slow deposition rate is crucial to achieve a rough metal surface, which is necessary for surface enhancement.[2] When the metal film is too thick, signal at the metal film/electrolyte interface would decrease, since the IR beam is reflected from the prism side/back side of the metal film. Cyclic voltammetry in 0.1 M H_2SO_4 is necessary to activate the surface enhancement effect of the metal film. For this process, cyclic voltammetry is first carried out, and potential hold at positive and negative potentials follows to check whether different peak intensities for water and sulfate can be observed at different potentials. If no spectra difference can be observed, the metal film has not been activated, and cyclic voltammetry needs to be repeated until metal film surface IR activation is achieved. The activation of the metal film can be confirmed once different peak intensities (positive/negative absorbance) of water and sulfate can be observed at positive/negative potentials (Figure A.2).

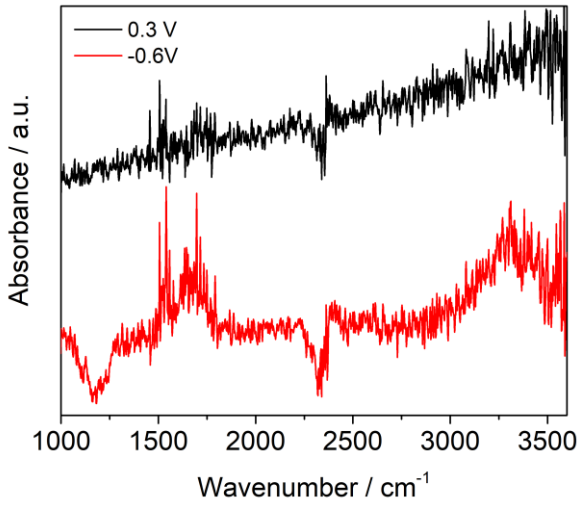

Figure A.2. SEIRAS spectra of 0.1 M H_2SO_4 at 0.3 V and -0.6 V for metal thin film surface IR activation process.

The setup for SEIRAS in this study is built on a Nicolet Magna-IR 550 spectrometer. Continuous purging of N_2 gas is required to remove CO_2 and water vapor inside the spectrometer, so that their noise level in the IR spectra can be removed. For current setup, the N_2 purging time needs to be greater than 3 hours to obtain low H_2O noise level. Improvement on the seal of the spectrometer setup can lower the purging time.

A.3 References

1. Ataka, K.-i.; Yotsuyanagi, T.; Osawa, M., Potential-Dependent Reorientation of Water Molecules at an Electrode/Electrolyte Interface Studied by Surface-Enhanced Infrared Absorption Spectroscopy. *J. Phys. Chem.* **1996,** *100*, 10664-10672.

2. Wang, T.; Dong, Z.; Koay, E. H. H.; Yang, J. K. W., Surface-Enhanced Infrared Absorption Spectroscopy Using Charge Transfer Plasmons. *ACS Photonics* **2019,** *6*, 1272-1278.

Appendix B: Dimensions of Pike Technologies VeeMAX III Attenuated Total Reflectance Accessory